

6692

NATIONAL LIBRARY
OTTAWA



BIBLIOTHÈQUE NATIONALE
OTTAWA

NAME OF AUTHOR.....NEAL.....HARVEY.....BURNETT.....
 TITLE OF THESIS.....AN.....INVESTIGATION.....INTO.....THE.....
 ..PROPERTIES.....OF.....WATER.....BLOWOFF.....
 ..METAL.....PLASMAS.....
 UNIVERSITY.....OF.....ALBERTA.....
 DEGREE FOR WHICH THESIS WAS PRESENTED.....Ph.D.....
 YEAR THIS DEGREE GRANTED.....1970.....

Permission is hereby granted to THE NATIONAL LIBRARY
 OF CANADA to microfilm this thesis and to lend or sell copies
 of the film.

The author reserves other publication rights, and
 neither the thesis nor extensive extracts from it may be
 printed or otherwise reproduced without the author's
 written permission.

(Signed).....*N. Neal Burnett*.....

PERMANENT ADDRESS:

...CENTRE...DE...L'ENERGIE
 ...C...P...1020.....
 ...VARENNE...P.Q....

DATED.....Sept 28.....1970

THE UNIVERSITY OF ALBERTA

AN INVESTIGATION INTO THE PROPERTIES OF LASER-BLOWOFF
METAL PLASMAS

by



NEAL HARVEY BURNETT

A THESIS

SUBMITTED TO THE FACULTY OF GRADUATE STUDIES
IN PARTIAL FULFILMENT OF THE REQUIREMENTS FOR THE DEGREE
OF DOCTOR OF PHILOSOPHY

DEPARTMENT OF ELECTRICAL ENGINEERING

EDMONTON ALBERTA

FALL 1970

ABSTRACT

The properties of the plasma formed by irradiating a massive aluminum target with a Q-spoiled ruby laser pulse have been examined experimentally and a simple model has been developed to account for several features of the laser-blowoff process, such as; depth of target fissure, flare temperature and density, and the expansion velocity of the plasma front.

The interaction of the laser-blowoff plasma with transverse magnetic fields in the 100 kgauss range has been studied in the simple geometry of a line current. The continued rapid motion of the plasma across fields of this magnitude has been attributed to a rapid electrical polarization of the plasma and an $\underline{E} \times \underline{B}$ drift.

ACKNOWLEDGEMENTS

This work was carried out between September 1967 and August 1970 at the Department of Electrical Engineering of the University of Alberta under the supervision of Professor P. R. Smy.

In addition to the above, the author would like to thank Dr. G. J. Pert for his interest and encouragement and R. M. S. Hardy for many useful discussions.

The apparatus, including the ruby laser head, was constructed under the supervision of Mr. E. Buck who also offered many suggestions concerning the design of the various components. The author would like to thank him and other members of the shop staff for their excellent and prompt service.

The author is grateful for the receipt of a National Research Council of Canada studentship during the course of these studies.

TABLE OF CONTENTS

INTRODUCTION	1
A Brief Review of the Literature	2
The Nature of the Present Work	5
Chapter 1. THE APPARATUS	8
1.1 The Laser	8
1.2 Experimental Setup for Blowoff Studies	13
Chapter 2. EXPERIMENTAL OBSERVATIONS OF THE BLOWOFF PROCESS	16
2.1 The Target	16
2.2 Size of Target Fissure	17
2.3 High Speed Photographic Studies	20
2.4 Emission-Absorption Diagnostics	24
2.5 Electrostatic Probe Measurements	41
Chapter 3. A SIMPLE PLANAR MODEL OF THE HEATING AND HYDRODYNAMIC EXPANSION OF A LASER-BLOWOFF PLASMA	50
3.1 The Model	51
3.2 The Numerical Solution	56
3.3 A Discussion of the Results and Comparison with Experiment	65
3.4 A Discussion of the Model	66
Chapter 4. THE FORMATION AND EXPANSION OF BLOWOFF PLASMAS IN A LARGE TRANSVERSE MAGNETIC FIELD	71

4.1	The Experiment	72
4.2	High Speed Photography	75
4.3	Emission-Absorption Measurements	79
4.4	Probe Studies	82
4.5	A Discussion of the Cross-Field Plasma Flow	87
4.6	The Source of the Plasma Velocity Reduction	94
4.7	Possible Cause of the Onset of Polarization	105
Chapter 5. CONCLUSIONS AND SUGGESTIONS FOR FUTURE RESEARCH		107
BIBLIOGRAPHY		110
	Review Papers	113
Appendix A	EFFECT OF DENSITY GRADIENT ON TEMPERATURE DETERMINATION	114
Appendix B	THE MODEL OF OPOWER AND PRESS	115
Appendix C	TURBULENT DISSIPATION	117

LIST OF ILLUSTRATIONS

Figure 1.1	The Laser Optical Head	9
1.2	Laser Cavity	10
1.3	The Flashtube Discharge Circuit	11
1.4	Laser Pulse Shape	12
1.5	Basic Setup for Blowoff Studies	13
1.6	The Target Chamber	15
2.1	Target Fissure on Aluminum	19
2.2	Experimental Arrangement for Image Converter Photographs	21
2.3	Optical Observations of the Flare	23
2.4	Experimental Setup for Emission-Absorption Diagnostics	26
2.5	Photomultiplier Calibration with 500Ω Load	27
2.6	Schematic of Plasma Flare and Test Cross-Section	28
2.7	The Spatial Filter	30
2.8	Emission-Absorption Profiles	32
2.9	Flare Temperature and Density 0.5mm from the Target Surface	35
2.10	Flare Temperature and Density 1.0mm from the Target Surface	36
2.11	Adiabatic Temperature Decay Profiles	38
2.12	Wall Probe Details	42
2.13	Wall Probe Signal	43
2.14	Biased Double Electrostatic Probe	44
2.15	Ion Current Waveforms to Double Probe	45
2.16	Current-Voltage Characteristics of the Double Probe	47

2.17	Position of the Leading Edge of the Ionization Front as a Function of Time	49
3.1	One Dimensional Plasma Slab	51
3.2	Assumed Laser Pulse Shape	54
3.3	Plasma Thickness as a Function of Time for $z = 3$; $\alpha = 1, 2, \text{ and } 10$	57
3.4	Expansion Velocity of the Leading Edge of the Plasma for $z = 3$; $\alpha = 1, 2, \text{ and } 10$	58
3.5	Plasma Temperature and Specific Energy for $z = 3$; $\alpha = 1, 2, \text{ and } 10$	59
3.6	Depth of Target Fissure for $z = 3$; $\alpha = 1, 2, \text{ and } 10$	60
3.7	Effect of Ion Charge Multiplicity on Plasma Thickness	61
3.8	Effect of Ion Charge Multiplicity on Expansion Velocity	62
3.9	Effect of Ion Charge Multiplicity on Plasma Temperature	63
3.10	Effect of Ion Charge Multiplicity on the Depth of Target Fissure	64
4.1	The Discharge Circuit	72
4.2	Underdamped RLC Current Waveform for 10kv Charging Voltage	74
4.3	Capacitor Bank Trigger Arrangement	75
4.4	50nsec Frames of Flare Development in a Magnetic Field	77
4.5	200nsec Streak Photographs of Flare Development in a Magnetic Field	78
4.6	Emission-Absorption Profiles with $B_0 = 70$ kgauss	80
4.7	Flare Temperature and Density 1.0mm from Target Surface with $B_0 = 70$ kgauss	81
4.8	Probe Insertion Geometry	82
4.9	Electric Field Probe Setup	83
4.10	Movable Probe Signals at $R = 1.5\text{cm}$	85

4.11	Expansion Velocity of the Sharp Ionization Front of an Aluminum Plasma in a Magnetic Field	86
4.12	Magnitude of the Transverse Electric Field at the Ionization Front	90
4.13	Maximum Plasma Diamagnetism 1.5cm from Surface of an Aluminum Target	91
4.14	Maximum Ion Current to the Double Probe 1.5cm from Surface of an Aluminum Target	93
4.15	Charge Separation in a Free Plasma Expansion	94
4.16	Response of Faraday Cup Wall Probe	97
4.17	Velocity of the Ionization Front of Plasmas Formed from Mg and Cu in a Magnetic Field	100
4.18	Width of Diamagnetic Signal at $B_0 = 70$ kgauss	103
4.19	Conductivity in Ionization Front 1.5cm from the Target Surface	104
4.20	Nature of the Particle Drifts Introduced by Magnetic Field Gradient and Curvature	106

LIST OF TABLES

Table 2.1	Marz Grade Aluminum Mass Spectrometer Analysis.	17
2.2	Dimensions of the Double Electrostatic Probes.	46
4.1	Ionization Energies of Al, Cu, and Mg.	98

INTRODUCTION

Since the advent of high power pulsed laser systems there has been considerable interest in their use to create high temperature plasmas from a variety of target materials. The essential property of lasers in this connection is that by this means it is possible to dump a relatively large amount of energy into a very small volume, which may lead to ionization and heating of gaseous, liquid, or solid target material. No special features have yet been observed in laser-produced plasmas due to either the coherence or monochromaticity of the laser light.

Solid target materials have several advantages for use in the creation of plasmas by laser heating and have historically received the most attention. By far the most important mechanism for absorption of optical radiation by hot, dense plasmas ($kT_e > 1\text{ev}$, $n_e > 10^{19}\text{cm}^{-3}$) is inverse bremsstrahlung¹, the absorption of photons by free electrons in the fields of ions. In order to obtain appreciable absorption by this mechanism at the temperatures of interest ($kT_e > 100\text{ev}$) within the focal volume of a laser, it is necessary to have electron densities in the range, $10^{20} < n_e < 10^{21}\text{cm}^{-3}$ (2). Such high densities are easily obtainable by the vapourization of solid target material. In addition it is relatively easy to isolate a solid target in a vacuum environment.

Experimentally the laser-solid interaction has been investigated in two distinct classes of experiments. In the first class^{3,4}, a small isolated speck of target material with dimensions of the order of 10^{-2}cm and containing about 10^{16} atoms has been suspended in the focal volume

of a laser focussing lens in a vacuum environment to create an isolated plasma of varying degree of spherical symmetry. In the second class^{5,6}, a massive solid target has been isolated in a vacuum environment and a Q-spoiled laser pulse focussed onto its surface, leading to intense local heating and ionization with the emission of a hot plasma flare away from the target surface. It is with this second class of plasma for which the term laser-blowoff plasma has been adopted that this thesis is concerned.

Apart from their use in the study of basic plasma phenomena such as ionization and recombination processes in dense plasmas and plasma instabilities, laser-blowoff plasmas have been proposed for a number of possible applications. These include their use as sources of soft x-rays⁷, sources of energetic ions and neutrals⁶, and pulsed neutron sources⁸. Much of the interest in laser-produced plasmas in general has centred on the possibility of obtaining a hot, clean plasma suitable for filling thermonuclear machines⁴.

A Brief Review of the Literature

1. Theoretical. The use of a laser to heat a solid particle to temperatures of thermonuclear interest was first proposed by Basov and Krokhin (1963)⁹. They proposed heating a small solid hydrogen pellet to temperatures of about 1000eV by showing that the absorption length for such a plasma at a density of approximately $3 \times 10^{21} \text{ cm}^{-3}$ and the ruby laser wavelength was of the same order of magnitude as the size of the focal spot into which the laser could be concentrated.

Shortly afterwards, Dawson (1964)¹⁰ presented a paper which elaborated on this proposal. Dawson considered the heating of lithium and hydrogen drops of initial dimensions of the order of 10^{-2} - 10^{-3} cm. He showed that for the dense plasma thus produced, the electrons could effectively transfer their energy to the ions and arrived at the figure of 4.4×10^{-10} sec for the electron-ion thermalization time. Dawson also considered the various energy loss mechanisms which might limit the obtainable temperatures and showed that by far the most important for these isolated plasmas was the rapid expansion of the drop which converts most of the incident laser energy into ordered motion. In addition, he foresaw that the expansion would rapidly reduce the density to a point where no further absorption could occur at optical frequencies, and so concluded that to be effective for such a process the laser energy would have to be delivered in a very short time (less than one nanosecond). The decisive and limiting role of the hydrodynamic expansion in his model led Dawson to suggest trying to trap such a plasma in a magnetic field.

The heating of a plasma formed by the laser irradiation of a solid surface situated in a vacuum was considered by Krokhin (1965)¹¹ who concluded by elementary means that the process must be self-regulating in the sense that the optical thickness of the plasma produced must be independent of time and of the order of unity. Krokhin's observations were incorporated into the models of Caruso et al^{12,13} to explain certain features of the laser-blowoff process through dimensional considerations. Shkuropat and Schneerson¹⁴ noted that for such a one dimensional plasma, the energy losses through expansion were not as severe as the case considered by Dawson.

In line with the proposals of Dawson, several papers were published^{15,16} on the expansion of a high β (β = ratio of kinetic pressure to magnetic pressure) plasma blob in a uniform magnetic field. It was concluded that such a plasma of high thermal conductivity would oscillate in diameter about the $\beta \approx 1$ value as its energy alternated between thermal and ordered expansion with the field lines alternately 'stretched' and 'relaxed.'

2. Experimental. Shortly after the theoretical proposals of Basov and Krokhin⁹ and Dawson¹⁰, several experiments were carried out which demonstrated the emission of ions and electrons in the kev energy range from solid surfaces irradiated by Q-spoiled laser radiation^{6, 17, 18, 19}. A comprehensive experimental study of the gas-dynamic motion of a laser-blow-off carbon plasma was reported by Basov et al²⁰. Spectroscopic determinations of the flare temperature were reported by Ambartsumyan et al²¹ and David and Wiechel²².

During the same period, much progress was reported on the experimental study of plasmas formed by laser irradiation of isolated solid particles. Haught and Polk³ succeeded in electrostatically suspending a small (10-20 μ) particle of LiH to produce a plasma with a high degree of spherical symmetry. They found that the observed form of the emitted ion signal could be explained by a refined version of Dawson's hydrodynamic model. Average plasma energies of 10-100ev were estimated from the time of flight measurements.

Ascoli-Bartoli et al⁴ extruded a short length of solid deuterium and investigated the effects of focussing a 200Mw laser onto it. They estimated the resulting plasma to have a temperature of about 10ev with a density of about 10^{18} cm^{-3} .

Sucov et al²³ studied the confining effect of a magnetic mirror field on the plasma produced by irradiating a 400 μ diameter aluminum target. The partial failure of this confinement attempt was attributed to an electrical polarization of the resulting plasma.

Recently, Tuckfield and Schwirze²⁴ have observed effects similar to those predicted by Bhadra¹⁵ and Poukey¹⁶ for the expansion of a laser-produced plasma into a mirror field. The same authors have presented evidence to show that the presence of collisionless instabilities may require extensions and modifications of the theory²⁵.

Other magnetic field interaction studies are currently in progress^{26, 27} on high temperature single particle plasmas, reflecting the current understanding that some sort of confinement will be necessary to create useful thermonuclear plasmas by laser heating.

The Nature of the Present Work

Despite the contribution to our understanding of the laser-solid interaction furnished by the experiments mentioned above, and others, several important phenomena associated with these plasmas remain little understood. For example, there exists much discrepancy between direct flare temperature measurements through spectroscopic and radiation techniques^{21, 22} and the observed energies of the emitted ions and x-rays^{6, 28}. In addition, the investigation of the interaction of such hot, dense plasmas with large magnetic fields remains a subject of prime importance since it is not yet clear whether they can be trapped or if macro-instabilities or plasma turbulence will prevent this.

The work reported in this thesis deals with the interaction of moderately high intensity ruby laser light (10^{11} watt/cm²) with massive metallic targets (for the most part aluminum). In particular, the formation and expansion of the blowoff plasma in large transverse magnetic fields (up to 120 kgauss) has been studied in the hope of observing effects similar to those predicted by the theories discussed above.

Following a brief description of the apparatus in Chapter 1, some experimental observations on the interaction of a 100Mw ruby laser pulse with an aluminum target will be presented in Chapter 2. A new technique for the measurement of the temperature and density of the luminous flare will be described and evidence presented to show that despite the release of ions with energies of several kev, the actual temperature in this region is only about 10ev at the end of the laser pulse.

In Chapter 3, a simple planar model of the heating and hydrodynamic expansion of laser-blowoff plasmas is presented. This model is shown to adequately explain several of the features of the process such as, flare temperature, the expansion velocity of the leading edge of the plasma, and the depth of the resulting target fissure.

Some investigations into the interaction of the blowoff plasma with transverse magnetic fields in the 100 kgauss range are described in Chapter 4, the magnetic field being generated by a line current through the target. The rapid expansion of the plasma across magnetic fields of this magnitude is attributed to an electrical polarization of the plasma and an $\underline{E} \times \underline{B}$ drift. An observed velocity reduction of the emitted ions and electrons at fields greater than 10 kgauss is attributed to an inhibiting effect of the magnetic field on the normal collective energy transfer between electrons and ions in the freely expanding blowoff plasma²⁹.

Some conclusions and suggestions for future research are presented in Chapter 5.

CHAPTER 1 THE APPARATUS

In most of the recent experimental research on laser-blowoff plasmas, lasers in the 100-200Mw range with several joules pulse energy have been focussed onto a slab or foil of target material through a simple lens of a few centimeters focal length. The most common target materials have been carbon in the form of pyrolytic graphite^{5,20,22}, and light metals such as aluminum^{30,31}.

In this chapter, the design and construction of a nominal 100Mw giant pulse ruby laser will be briefly described and details of the experimental setup used in the present laser-blowoff studies presented.

1.1 The Laser

The laser used in these studies was designed and constructed at the University of Alberta. It utilized a 3" x 3/8" select quality ruby crystal situated between external reflectors in a close coupled double elliptic cavity. The optical pumping was accomplished by two FX-47 flashtubes and the device was Q-switched by means of a Pockels cell.

The optical configuration of the laser head is shown in Figure 1.1.

The laser cavity was fabricated from two sections of solid aluminum with inside surfaces highly polished. The top section could be removed for access to the ruby crystal and flashtubes. The flashtubes were enclosed in pyrex glass sleeves which served to shield the ruby crystal from u.v. light and allowed a flow of nitrogen vapour to be passed along them for cooling purposes. The ruby crystal itself was supported by four

1/8" diameter pyrex rods which could be adjusted from outside the cavity for alignment. Details of the cavity geometry and support structure are shown in Figure 1.2.

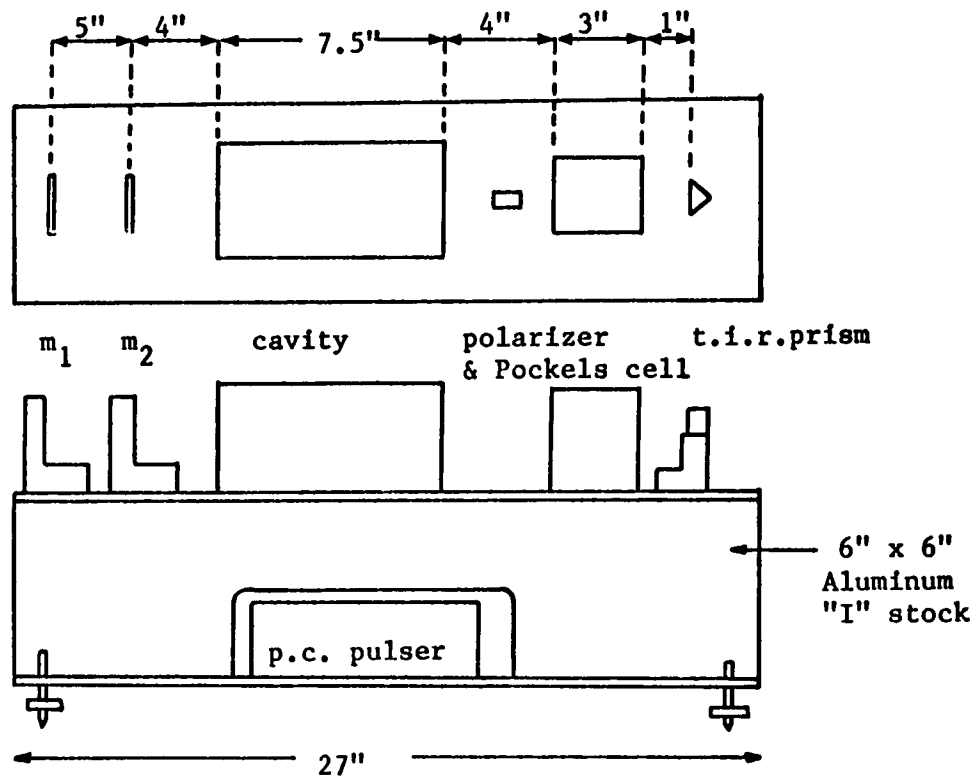
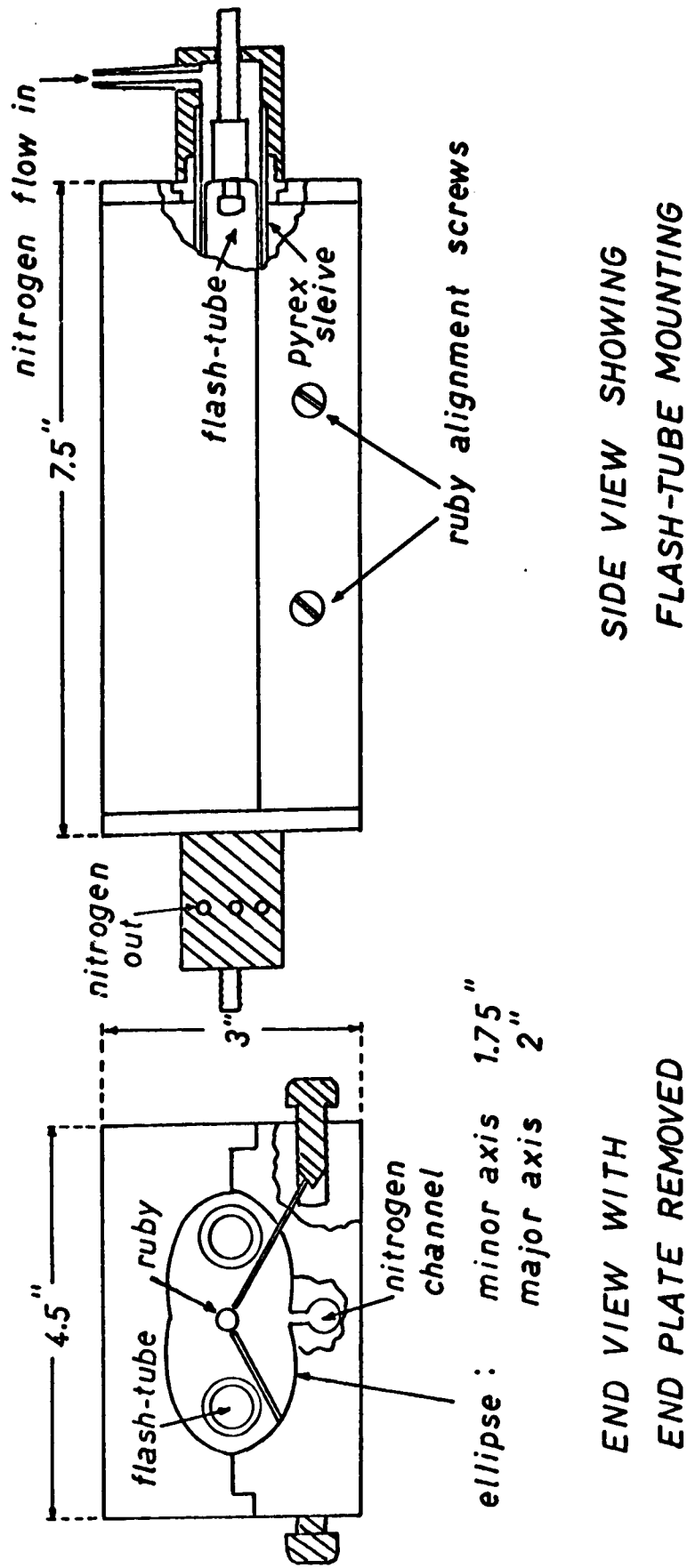


Figure 1.1 Laser Optical Head.

The cavity was also cooled by nitrogen vapour which was forced onto the crystal through a series of small holes in the upper and lower halves of the cavity. The nitrogen flow was obtained from a sealed Dewar flask into which was placed a reostat controlled heating element.

The external optics consisted of two dense glass reflectors (m_1 and m_2 in Fig. 1.1), the Pockels cell and polarizer, and a total internal reflection prism. The two front reflectors were mounted about 5" apart



END VIEW WITH
END PLATE REMOVED

SIDE VIEW SHOWING
FLASH-TUBE MOUNTING

FIG. 1.2 LASER CAVITY

in such a way as to prevent mode locking in the laser output. The total reflectivity of the pair was about 40%. The Pockels cell, manufactured by Isomet Corp., consisted of a deuterated KD*P crystal operated in the $1/4$ wave retardation mode, and was used with a Glan air-spaced polarizer. The free aperture of the polarizer and Pockels cell was about $1/2$ ".

The energy for the flashtube discharge was furnished by a $1600\mu\text{F}$, 2kv capacitor bank and pulse forming network. The discharge was initiated with a series injection trigger transformer. This device with its associated circuitry furnished μsec pulses of up to 75kv at the secondary windings. The discharge circuit and approximate current wave form is shown in Figure 1.3.

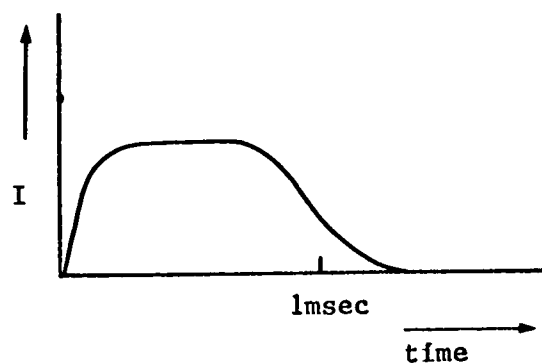
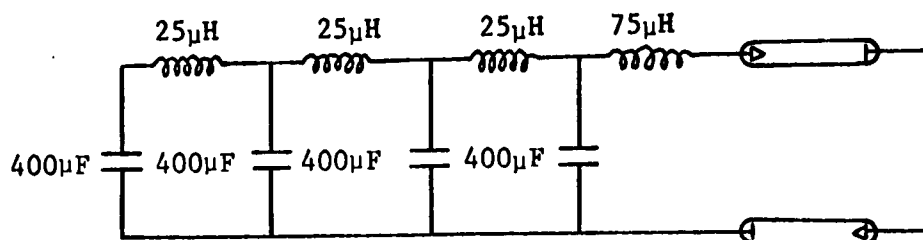


Fig. 1.3 The Flashtube Discharge Circuit.

The Pockels cell electronics was obtained from Optics Technology Inc. and consisted of a low jitter delay unit (up to 1msec delay), a high voltage power supply, and a thyratron pulse generator of about 5nsec risetime. A timing reference pulse was obtained at the initiation of the flashtube discharge from a photo-resistor mounted near the optical cavity. This was used to trigger the delay unit which after about 1msec furnished a 300v pulse to the Pockels cell pulse generator and a 30v reference pulse. The pulse generator was mounted in the optical head as shown in Figure 1.1. The delay time between the 30v reference pulse and the laser pulse was about 50nsec.

The laser was found to have a threshold for spontaneous laser action at about 2000joules input energy. In the Q-spoiled mode, it was found that an input of approximately 3000joules was sufficient to yield a 2 joule pulse of ~ 15 nsec full width at half power. The laser power was reproducible within about 10% providing five minutes or so were allowed for cooling between shots. The experimentally measured divergence of the Q-spoiled output was 2.0×10^{-3} rad.

The approximate laser pulse shape as recorded by means of a planar photodiode and a Textronix 519 oscilloscope is shown in Figure 1.4.

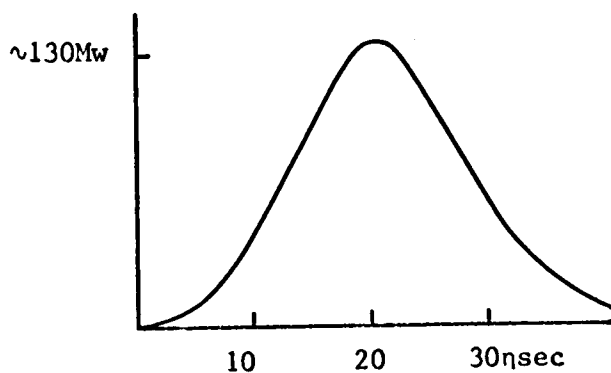


Fig. 1.4 Laser Pulse Shape.

1.2 Experimental Setup for Blowoff Studies

A schematic of the basic arrangement adopted for the experimental laser-blowoff studies is shown in Figure 1.5. A 2mwatt helium-neon laser was used to align the optical system and the target which was a 1/4" diameter metal rod. An I.T.T. type FW-114A planar photodiode was used to monitor the giant pulse shape and power. This was mounted in a co-axial waveguide structure and calibrated against a calorimeter placed at the target position. Care was taken to ensure that the optical pathlength from the ruby laser to the photodiode was equal to the pathlength to the target.

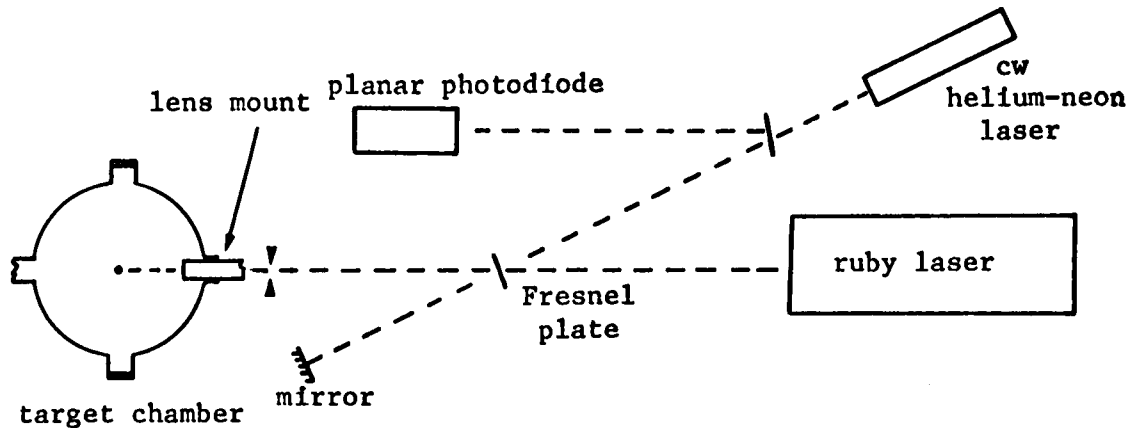
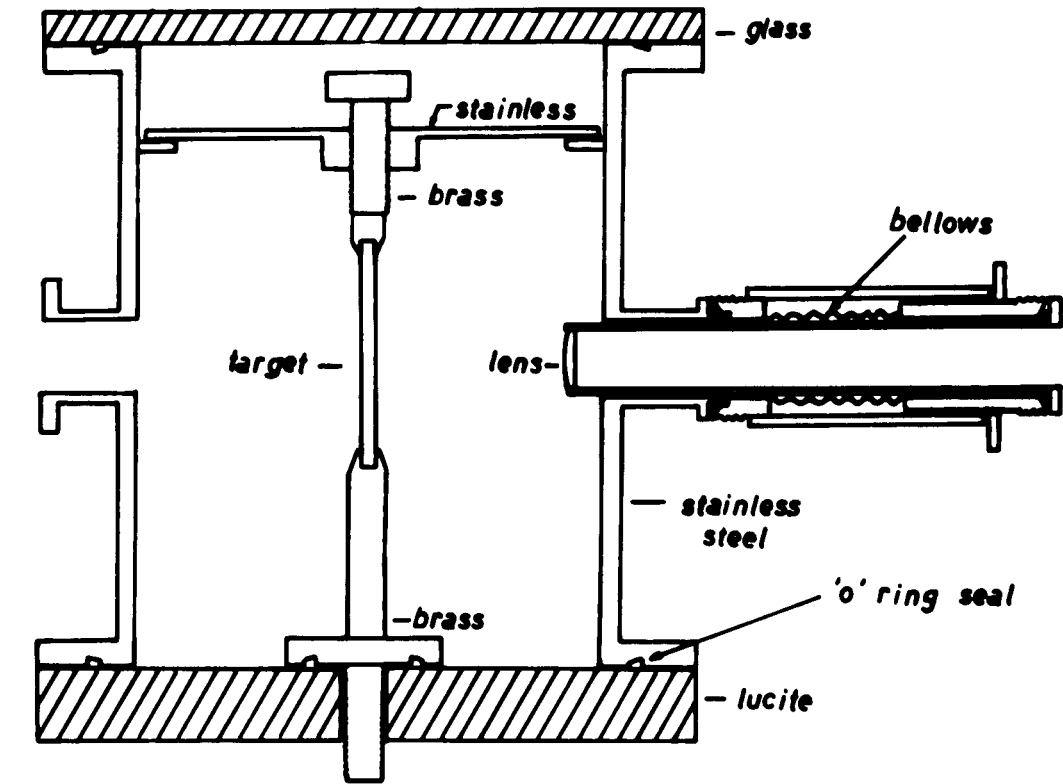


Fig. 1.5 Basic Setup for Blowoff Studies.

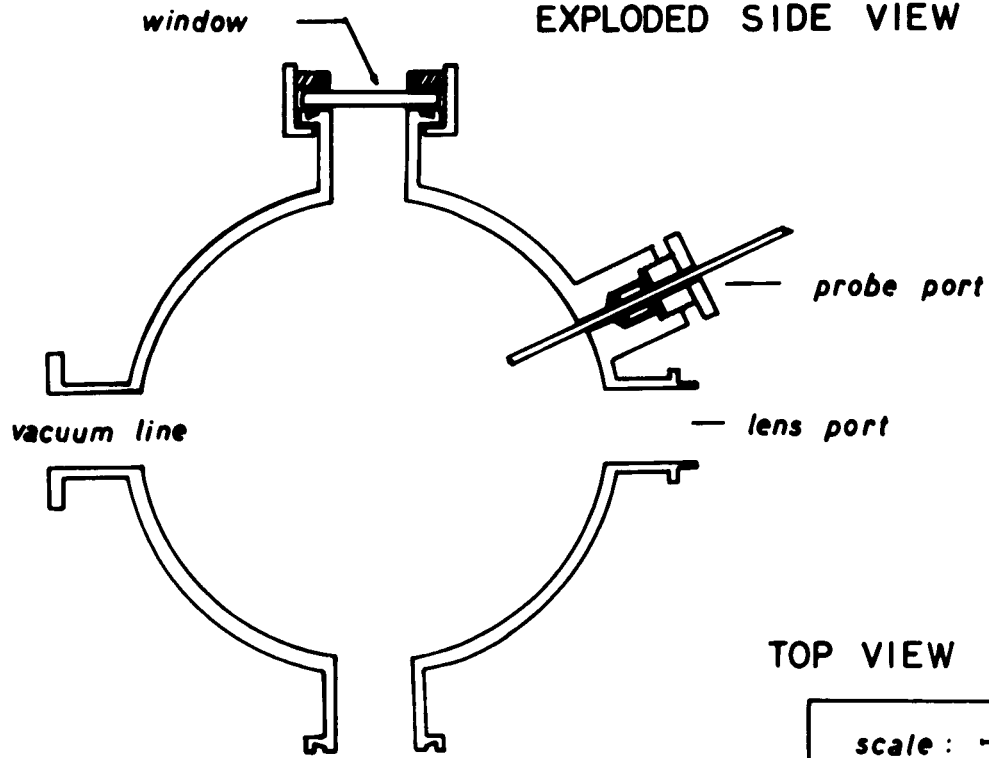
The target in the form of a 1/4" diameter by 3" long metal rod was enclosed in a vacuum chamber capable of being evacuated to 10^{-6} torr with an externally adjustable 45mm F.L. plano-convex laser focussing lens. For the purposes of the experiment discussed in Chapter 3, provision was made for a large current to be discharged through the target from an external capacitor bank.

The stainless steel vacuum chamber was connected to a Varian, model 941-5610 "Vacsorb" forepump and an 8 litre per second "Vacion" pump. This was sufficient to obtain a base pressure of about 10^{-6} torr with a recycling time of about two hours. For the experiments, the target chamber was evacuated to 1×10^{-5} torr before each shot.

The target chamber and lens focussing system is shown in some detail in Figure 1.6. The two one inch diameter windows at right angles to the incident laser path allowed photographic observations of the blowoff process and were also used for the emission-absorption measurements described in Chapter 2. Other diagnostic techniques were provided for by a probe port located at an angle of 20° to the incident laser path. This port accepted glass-sheathed 5mm probes which could be moved radially in towards the target surface while maintaining a vacuum seal.



EXPLODED SIDE VIEW



TOP VIEW

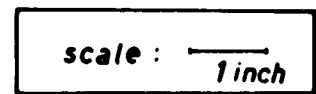


FIG. 1.6 THE TARGET CHAMBER

CHAPTER 2 EXPERIMENTAL OBSERVATIONS OF THE BLOWOFF PROCESS

Some experimental investigations into the properties of freely expanding laser-blowoff aluminum plasmas will be described in this chapter. These include microphotographic studies of the resulting target fissure, image converter framing and streak camera photographs of the luminous flare formed at the target surface, and electrostatic and Faraday cup charge collection probe studies of the emitted ionization.

A simple technique for flare temperature and density measurement will be described and evidence presented to show that despite the release of ions in the 1000ev energy range, the temperature of the luminous flare near the target surface is only about 10ev at the end of the laser pulse.

2.1 The Target

The experimental observations reported in this chapter concern the interaction of a laser pulse of the characteristics discussed in Chapter 1 with an aluminum target. Aluminum was chosen because of the considerable background of data on plasmas formed from this metal^{30,31,32} and the availability of high purity samples. These were obtained as Marz grade polycrystalline rod from Materials Research Corp.. An approximate impurity analysis of this material as supplied by the manufacturer is shown in Table 2.1.

ELEMENT	CONTENT (ppm)
C	5
H	<1
O	5
N	<1
Ca	0.15
Cl	0.4
Cr	0.2
Cu	0.5
Fe	0.5
K	0.4
S	0.4
Si	<1
Zn	1
Rare earths	<0.5
All others	<0.1

Table 2.1 Marz Grade Aluminum Mass Spectrometer Analysis.

2.2 Size of Target Fissure

The degree to which laser radiation can be concentrated by a simple lens is a complicated function of the laser beam divergence, the focal length of the lens, and the optical quality of the lens. A perfect lens of focal length F would result in a focal spot diameter,

$$D = 2 F \Delta\phi \quad \dots 2.1$$

where $\Delta\phi$ is the laser beam divergence. For $\Delta\phi = 2.0 \times 10^{-3}$ rad, $F = 45$ mm, this results in a focal spot diameter, $D = 0.180$ mm. Thus an input of 130Mw would result in an average power at the focal point of the lens of 5.5×10^{11} watt/cm².

In order to ascertain the actual focal diameter with a lens of the type used in these investigations, and to determine the number of target

atoms involved in the blowoff process, the target crater caused by the action of the 130Mw laser pulse was studied with a photomicroscope. A typical microphotograph of the laser impact area on an aluminum target is shown in Figure 2.1.

Of five shots examined in this way, the damage area had a fairly constant diameter of $300 \pm 20 \mu$ and a depth of $15 \pm 5 \mu$. The latter was estimated by alternately focussing the microscope on the bottom and top of the crater. Taking the density of solid aluminum to be 2.4×10^{22} atoms/cm³, about $3 \pm 1 \times 10^{16}$ aluminum atoms were involved in the blowoff process. Since the laser input was about 2 joules, neglecting any energy losses, about $2 + (3 \times 10^{16} \times 1.602 \times 10^{-19}) = 500 \text{ ev}$ was available for each aluminum atom involved in the process. (For example, if each atom were ionized to the Al⁴⁺ level and the ionization energy were subtracted, about 70ev would be available for each plasma particle.)

Assuming a uniform distribution of the laser intensity over the 300μ damage area, the peak power delivered to the target surface by the 130Mw laser pulse was about 1.8×10^{11} watt/cm².




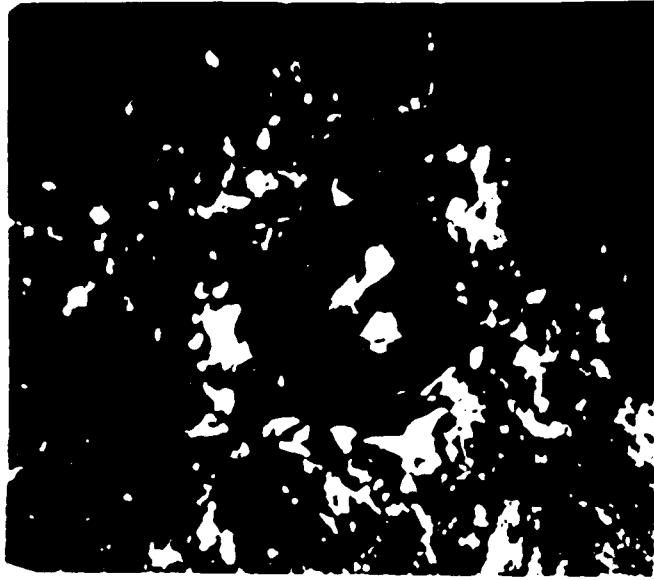
SCALE :  300 μ

FIG. 2.1 TARGET FISSURE ON ALUMINUM



SCALE : $\overline{\hspace{1.5cm}}$
300 μ

FIG. 2.1 TARGET FISSURE ON ALUMINUM

2.3 High Speed Photographic Observations

The expanding plasma flare formed during the blowoff process was studied using a T.R.W. image converter camera with high speed framing and streak plug in units. The framing unit was a type 26B, providing up to five frames with a minimum exposure duration of 50 η sec and minimum inter-frame delay of 250 η sec. This unit requires a +300v, 10 η sec risetime trigger pulse and provides an 8v output monitor of the shutter pulse train. The streak plug in was a model 7B with writing times of 50, 100, and 200 η sec in a five centimeter streak. It requires a 500v, 10 η sec risetime trigger pulse. A block diagram of the experimental arrangement used to trigger the camera is shown in Figure 2.2.

A 20v pulse from a photo-resistor near the flashtubes marked the onset of the pumping discharge and triggered a 1msec delay unit which provided three 50 Ω output pulses. The first, a 300v, 10 η sec risetime pulse was used to trigger the Pockels cell pulser which opened the laser shutter after a fixed delay of about 100 η sec. The second, a 30v pulse was used to trigger a Tektronix type 585 oscilloscope. The third, another 300v, 10 η sec risetime pulse was amplified to 500v by a simple high pressure thyratron circuit and passed through a delay line (Tektronix type 113 plus additional lengths of 50 Ω cable) so as to trigger the camera a few nanoseconds before the arrival of the laser pulse at the target surface. This synchronization was confirmed by adding the camera shutter monitor pulse and the photodiode laser monitor signal and displaying the result on the oscilloscope through a type 81 differential plug in. Care was taken to ensure equal cable lengths to the camera and the photodiode.

For the streak photographs, a 1mm wide slit was masked onto the face

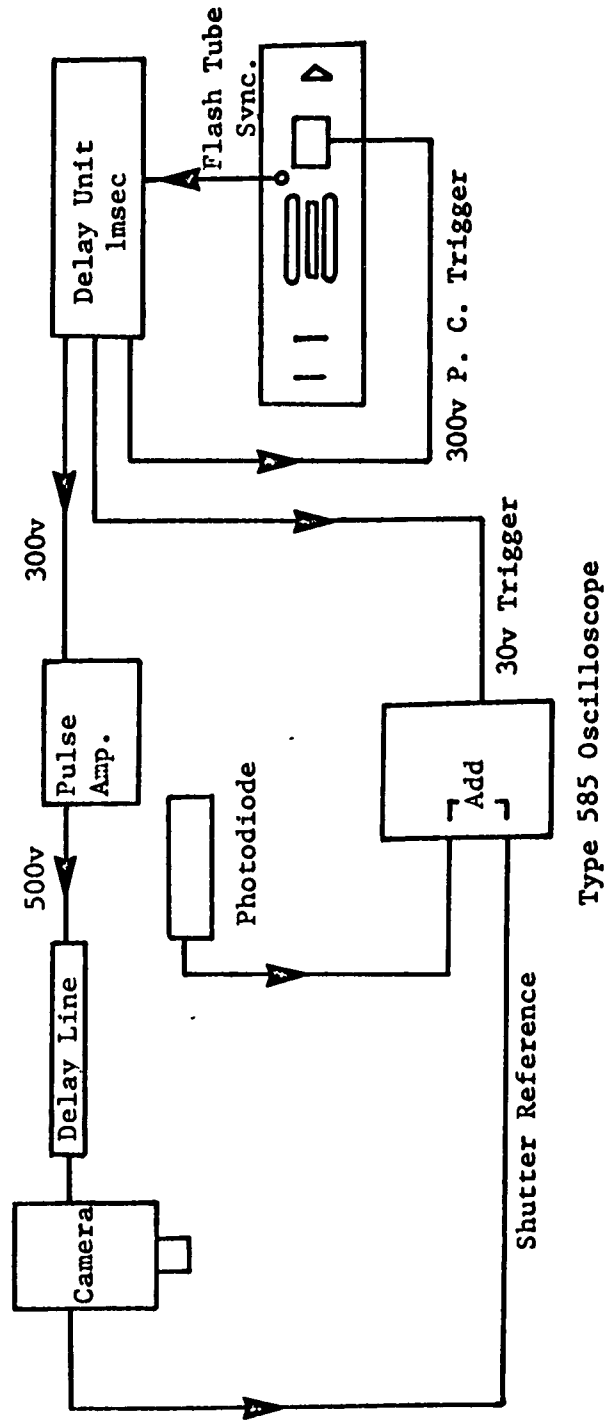
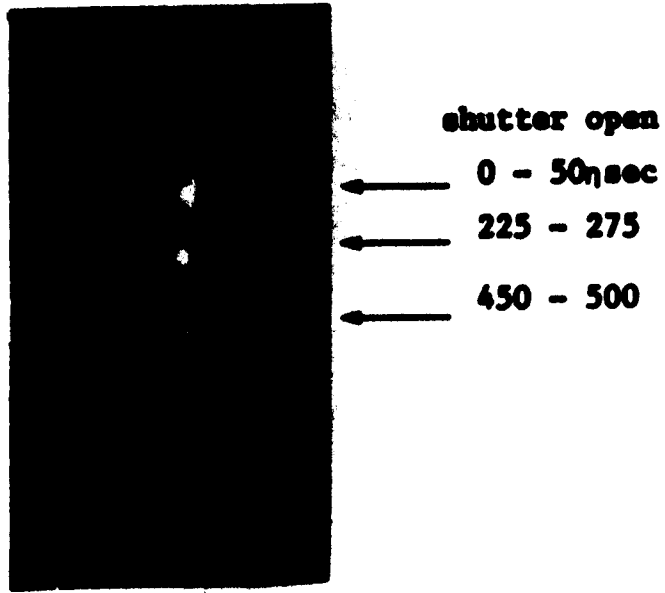


Fig. 2.2 Experimental Arrangement for Image Converter Photographs

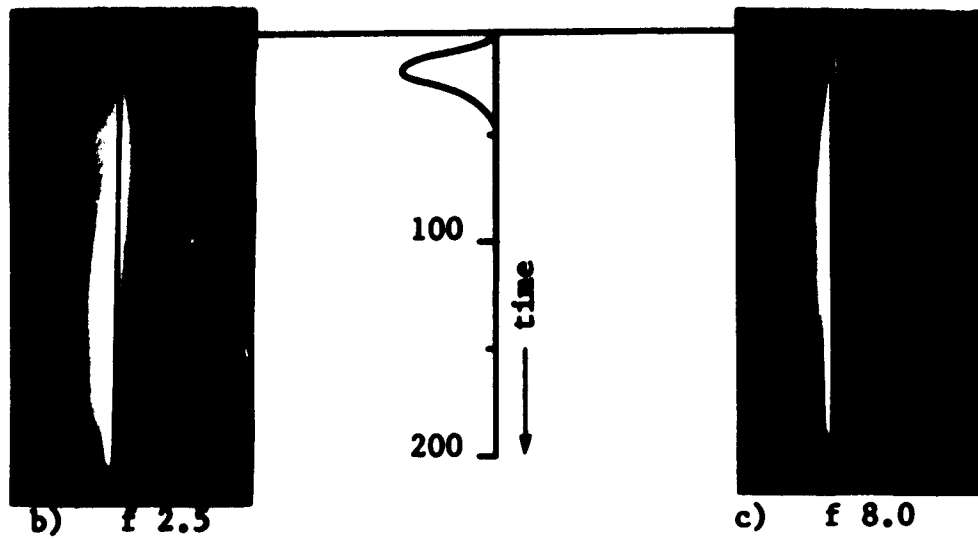
of the image converter tube to improve the resolution of the photographs.

The resulting streak and framing photographs are shown in Figure 2.3. It can be seen that a more or less spherically symmetric bright nucleus forms tangentially to the impact area during the laser pulse (Fig. 2.3a) and that some luminosity persists in this region for more than 500nsec after the end of the laser pulse. Because of the relatively long exposure duration (50nsec), the framing photographs fail to yield much information on the dynamics of the plasma flare, however, the 200nsec streaks indicate the flare consists of a highly luminous, sharply defined central core (Fig. 2.3c) which expands from an initial diameter of about 1mm at a rate of $2-3 \times 10^6$ cm/sec for about 50nsec before becoming stationary, and a more diffuse, less luminous region (Fig. 2.3b) which expands at about $4-5 \times 10^6$ cm/sec for more than 100nsec after the end of the laser pulse.

The persistence of luminosity near the impact area for more than 500nsec after the end of the laser pulse suggests that in these late stages at least, the luminous region is inhabited by a relatively cold, recombination dominated plasma. That is, the emission of material from the target vicinity must proceed at about its thermal velocity so that in the absence of any additional energy sources the plasma will cool through adiabatic expansion within a few tens of nanoseconds after the end of the laser pulse.

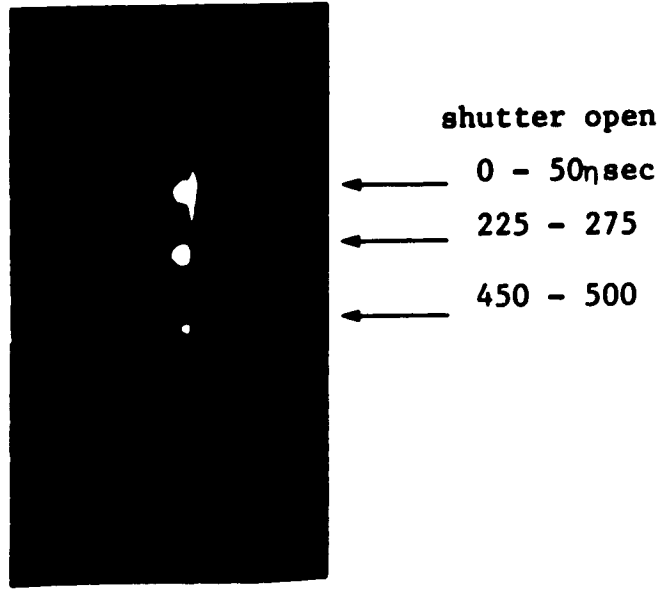


a) Framing Camera Photograph - f 25

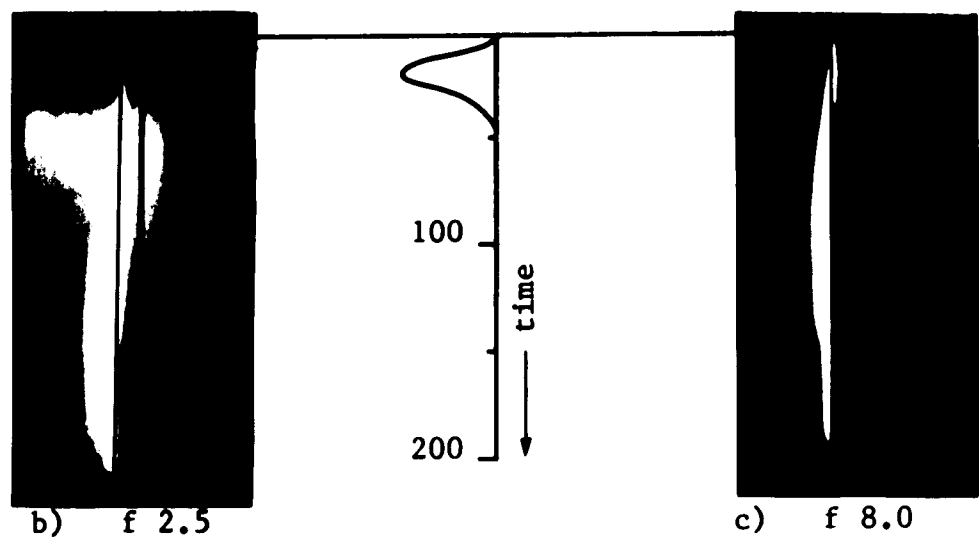


200nsec Streak Photographs

Fig. 2.3 Optical Observations of the Flare.



a) Framing Camera Photograph - f 25



200 nsec Streak Photographs

Fig. 2.3 Optical Observations of the Flare.

2.4 Emission-Absorption Diagnostics

In order to gain some insight into the relatively long lifetime of the luminous flare, a simple technique was developed for direct measurement of temperature and density in this region at the end of the laser pulse. This was a modification of the technique employed by Lampis and Brown³³* in afterglow studies on a laser spark in helium.

The method was to isolate a small cross-section of the flare by means of a spatial filter and determine the plasma source function in a narrow wavelength interval by comparing the plasma absorption and emission through the test cross-section. The emission in a 20\AA region about the He-Ne laser wavelength (6328\AA) was isolated by means of a narrow line-pass filter and the absorption at this wavelength measured directly from the attenuation of a cw He-Ne laser. The experimental configuration is shown in Figure 2.4.

A 57cm focal length lens, L_1 , mounted on a precision transverse slide was used to focus the beam from a 2mw cw He-Ne laser to a diameter of about 0.75mm, and to position it in front of the aluminum target rod. The laser was also used to align the spatial filter comprising elements A_2 , L_2 , and A_3 ⁽³⁴⁾ which selected the same 0.75mm diameter cross-section.

* The method described here differs from that used by Lampis and Brown in that a spatial filter was employed in the present measurements rather than averaging the plasma emission over its whole volume.

The absorption and emission through the test cross-section were monitored by means of an R.C.A. type 8645 photomultiplier tube enclosed in a light-tight box containing the chromatic filters F_1 , F_2 , and F_3 . F_1 was a 6500\AA low pass filter, F_2 , a 6000\AA high pass filter, and F_3 , a 20\AA band-pass filter centred at 6328\AA . The photomultiplier with 500Ω load had a rise-time of 5nsec and was connected to a Textronix 585 oscilloscope directly through a cable short enough to prevent troublesome ringing (about one foot). The detection system was calibrated for the emission measurements by passing the He-Ne laser through various neutral density filters, monitoring the power at the target position by calorimeter, and recording the photomultiplier response.

The calibration curves obtained in this way are shown in Figure 2.5 at two photomultiplier voltages, 1400v (used for emission measurements), and 1000v (used for absorption measurements).

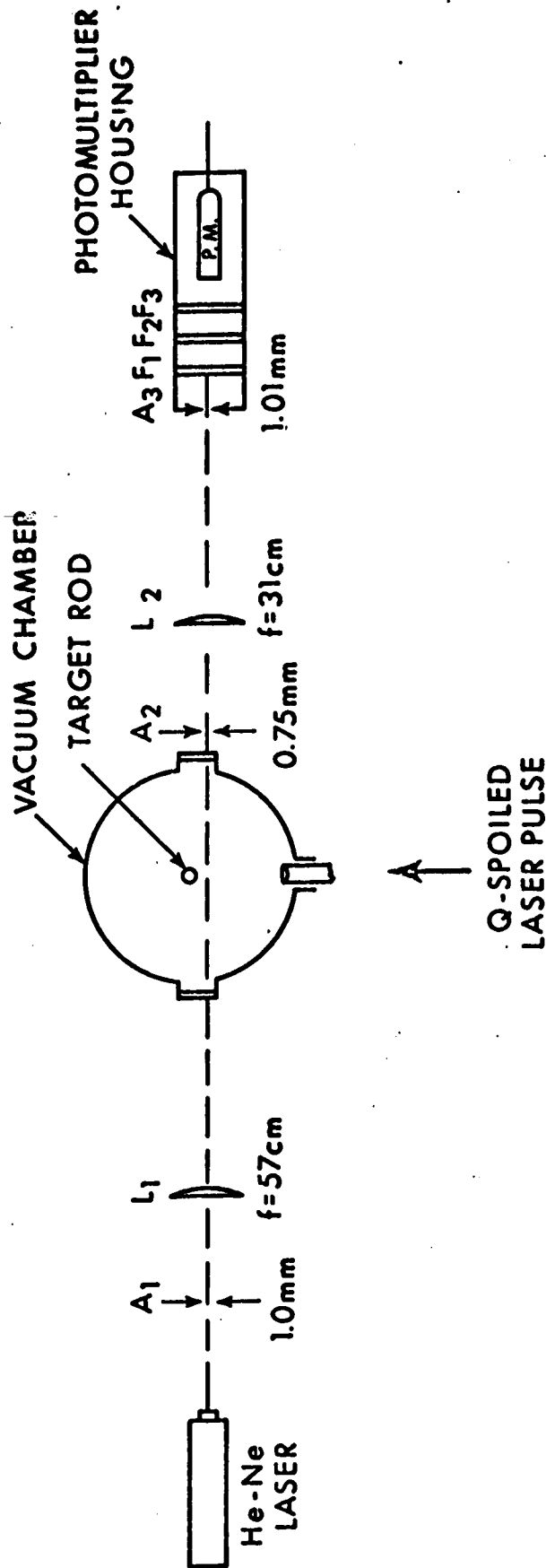


Fig. 2.4 Experimental Setup for Emission-Absorption Diagnostics.

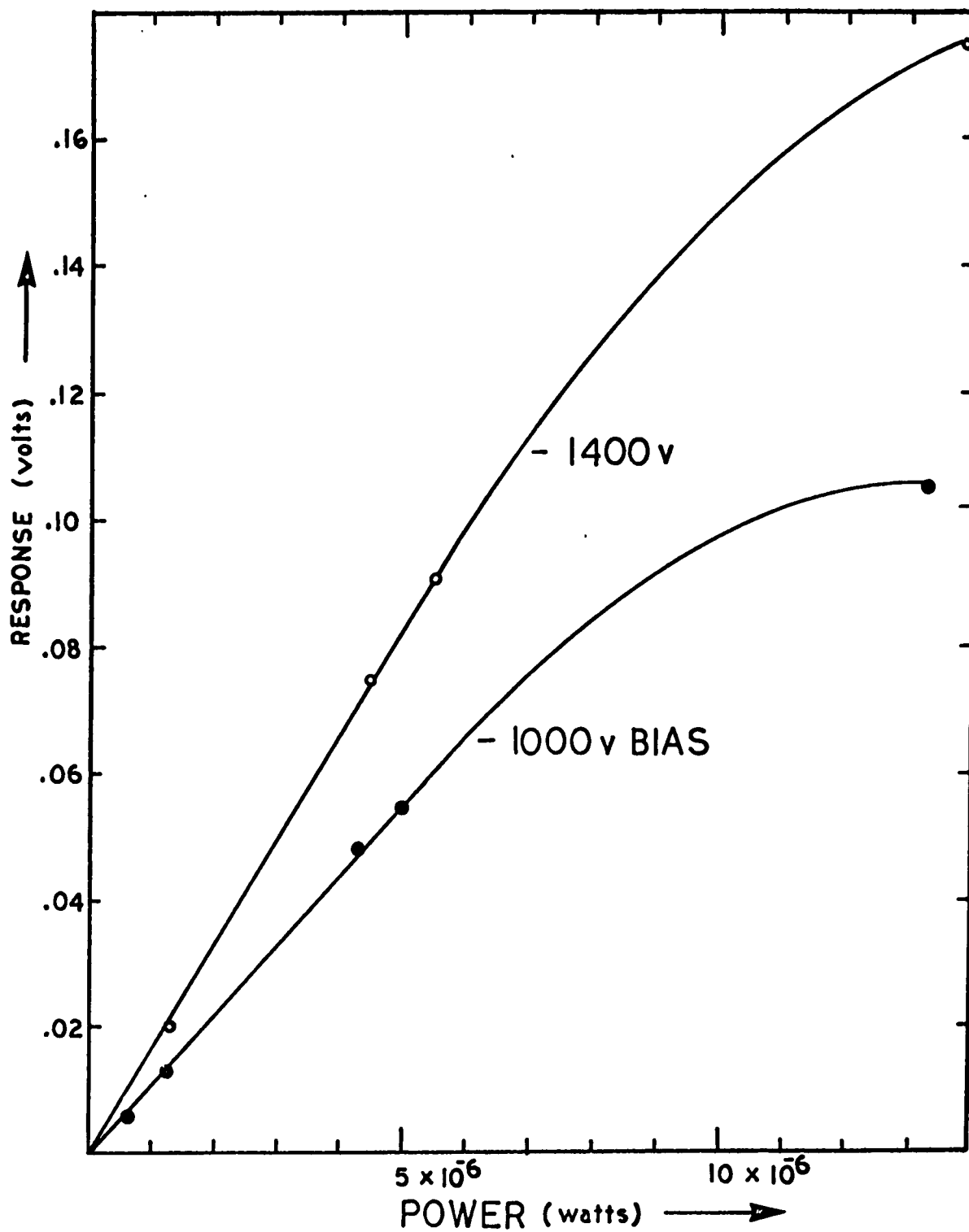


Fig. 2.5 Photomultiplier Calibration with 500Ω Load.

If one considers a plane plasma slab of uniform properties, the ratio of emissivity and absorptivity will give the plasma temperature in terms of its source function which can be equated to the Planck function for the case of a thermal equilibrium plasma.

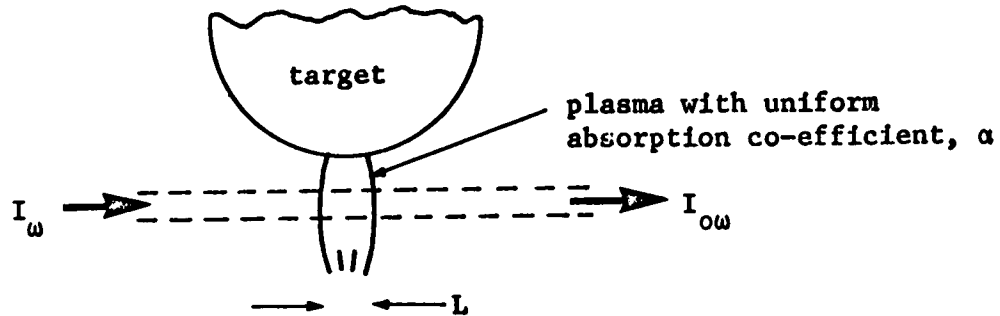


Fig. 2.6 Schematic of Plasma Flare and Test Cross-Section.

With reference to Figure 2.6, if we define E_ω as the power emitted per (unit area) \times (solid angle) \times (angular frequency interval), I_ω as the incident cw laser intensity, and $I_{\omega'}$ as the transmitted laser intensity, then,

$$I_{\omega'} = I_\omega e^{-\alpha L} \quad \dots 2.2$$

and,

$$E_\omega = S_\omega (1 - e^{-\alpha L}) \quad \dots 2.3$$

where if local thermodynamic equilibrium is obtained, the source function, S_ω is the Planck function,

$$S_\omega = \frac{\hbar \omega^3}{4 \pi^3 c^2} \left\{ \exp \frac{\hbar \omega}{kT} - 1 \right\}^{-1} \quad \dots 2.4$$

So that,

$$\frac{E_{\omega}}{1 - \frac{I_{\omega\omega}}{I_{\omega}}} = S_{\omega} \quad , \quad \dots 2.5$$

and to obtain a temperature estimate from E_{ω} , $I_{\omega\omega}$, and I_{ω} , no knowledge of the plasma thickness is required.

Since the He-Ne laser frequency is far removed from any strong aluminum lines, the absorption at this wavelength is due to inverse bremsstrahlung¹⁰. The absorption coefficient for this process, corrected for induced emission, is given by Spitzer¹ as,

$$\alpha = 3.69 \times 10^8 \frac{z^3 n_i^2}{T^{3/2} \nu^3} (1 - \exp \frac{-h\nu}{kT}) \text{ cm}^{-1} \quad , \quad \dots 2.6$$

where z is the ionic charge multiplicity. Thus $I_{\omega\omega}$ and I_{ω} will be related by,

$$I_{\omega\omega} = I_{\omega} e^{-\alpha L} \quad , \quad \dots 2.7$$

where L is the plasma thickness. Therefore, a knowledge of the dimension L allows a calculation of n_i , assuming the ionic charge multiplicity is known.

The properties of the spatial filter used in these measurements have been analyzed by Rogoff³⁴. The basic elements of this device are shown in Figure 2.7.

The lens L_2 serves to image aperture A_3 at A_3' such that the width of A_3' equals the width of A_2 . Thus all light which passes through both A_3' and A_2 is transmitted and all else is discriminated.

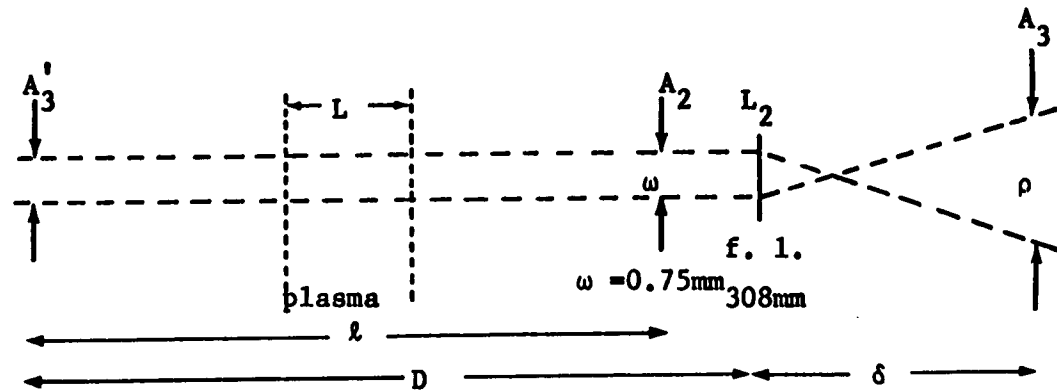


Fig. 2.7 The Spatial Filter.

It is thus required that,

$$\delta = \frac{Df}{D - f} ,$$

$$\rho = \frac{\omega f}{D - f} .$$

These criteria were met by setting,

$$\begin{aligned} \ell &= 29\text{cm}, \\ D &= 54\text{cm}, \\ \delta &= 72.7\text{cm}, \\ \rho &= 1.01\text{mm}, \\ \text{and } \omega &= 0.75\text{mm}. \end{aligned}$$

The (solid angle) \times (area) integral for this arrangement has been shown by Rogoff to be approximately given as,

$$\begin{aligned} \int \Omega \, dA &\approx \frac{\pi^2 \omega^4}{\ell^2} , \\ &= 2.31 \times 10^{-8} \text{ cm}^2 \end{aligned}$$

The frequency interval of the plasma emission reaching the detector was limited by the narrow line-pass filter installed in the photomultip-

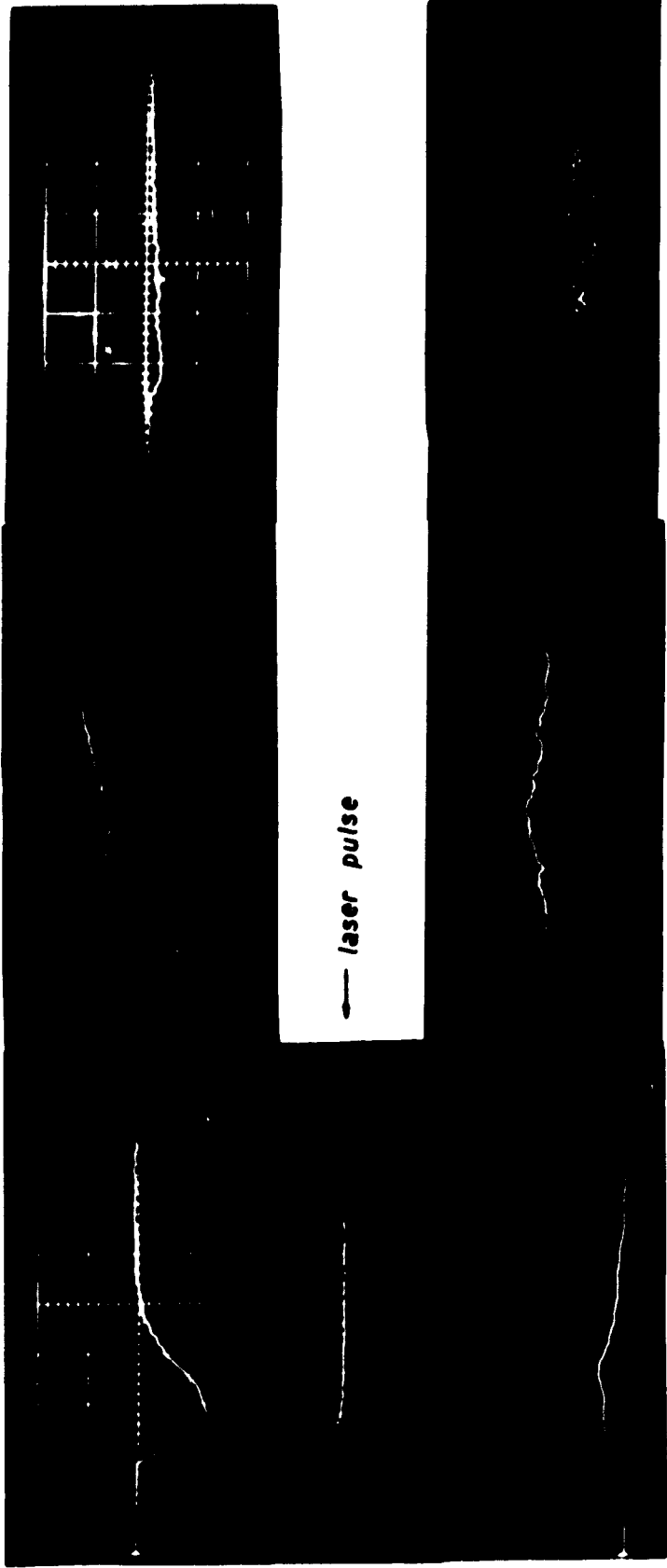
lier housing. This was obtained with calibrated transmission curve from Perkin-Elmer Corp.. It possessed a 60% transmission spike at 6328\AA with a 20\AA full width at half power. Thus the spectral range of the detected plasma emission was estimated as $20\text{\AA} \pm 10\%$.

Emission and absorption profiles were recorded on a Textronix 585 oscilloscope which was triggered from the photodiode laser monitor. Care was taken to insert calibrated neutral density filters at the front of the photomultiplier housing if required to keep the photomultiplier response in its linear range (see Fig. 2.5). The photomultiplier bias was set at 1400v for the emission measurements and 1000v for the absorption measurements. To allow for the diverging effect of the plasma curvature on the cw He-Ne laser beam, it was necessary to increase apertures A_2 and A_3 to 1.5 and 2.5mm respectively when measuring the plasma absorption.

Emission and absorption profiles of the Al plasma flare are shown in Figure 2.8 with the spatial filter centred at 0.5, 1.0, and 1.5mm from the target surface. Both signals were quite reproducible for up to five shots before it was necessary to rotate the target to expose a fresh surface.

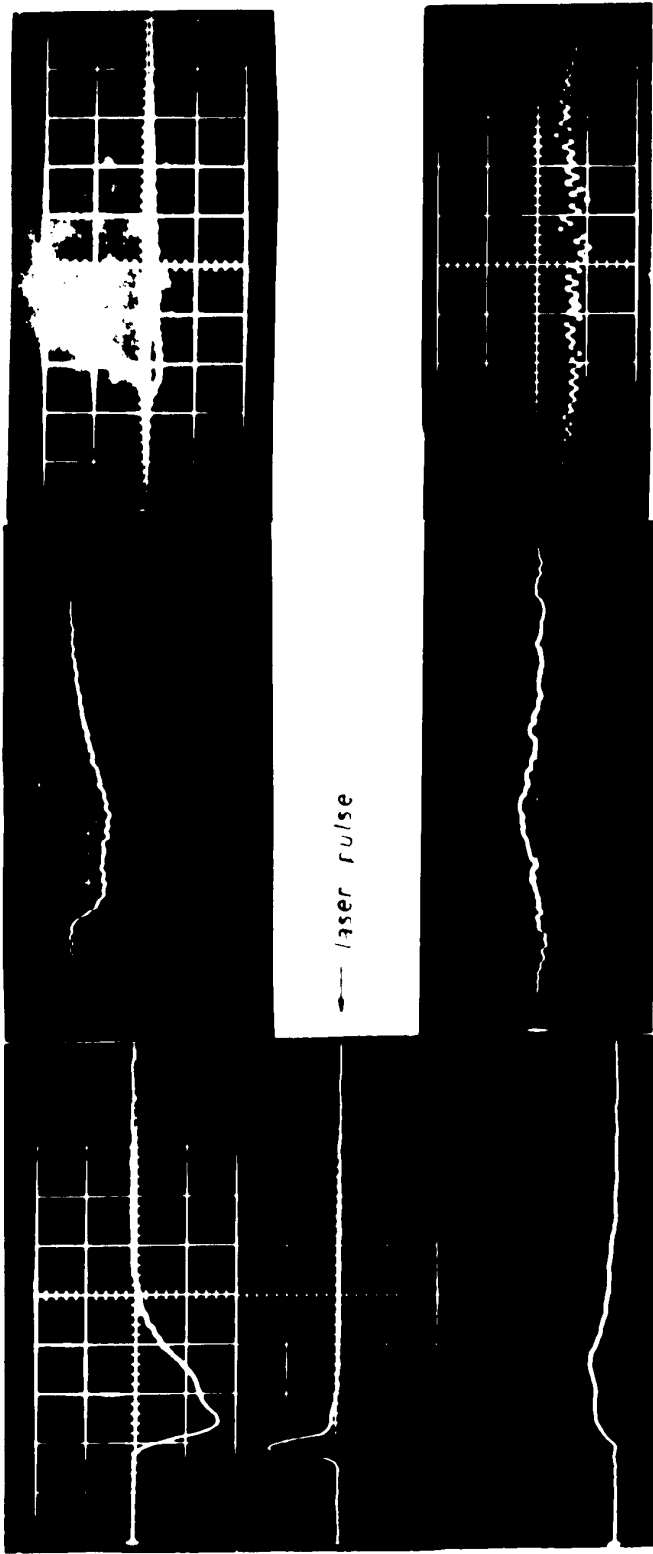
The traces of Figure 2.8 allow a temperature calculation to be made as follows: if we denote the power registered by the photomultiplier during the plasma emission measurements by I_{ω}^e , then,

$$\frac{I_{\omega}^e}{1 - \frac{I_{0\omega}}{I_{\omega}}} = \frac{2hc}{\lambda^3} \left[\exp\left(\frac{hv}{kT}\right) - 1 \right]^{-1} \left[\int_{\Omega} dA \right] \left[\delta v \right] \quad \dots 2.7$$



R = 0.5 mm	R = 1.0 mm	R = 1.5 mm
EMISSION - UPPER	P.M. = 1400v	P.M. = 1400v
TRACE :	50 ηsec/div	50 ηsec/div
	0.1 v/div (neutral density = 0.5)	.05v/div
ABSORPTION - LOWER	P.M. = 1000v	P.M. = 1000v
TRACE :	.05 v/div (dc level = .08v)	.005 v div (.08v)

FIG. 2.8 EMISSION ABSORPTION PROFILES



R = 1.0 mm R = 1.5 mm
 E.M. = 1400V E.M. = 1400V
 50 nsec/div 50 nsec/div
 100 nsec/div 100 nsec/div
 100 nsec/div 100 nsec/div
 100 nsec/div 100 nsec/div
 100 nsec/div 100 nsec/div

EMISSION ABSORPTION PROFILES

where from the discussion above,

$$\int \Omega \, dA = 2.31 \times 10^{-8} \, \text{cm}^2$$

$$\delta \nu = 20 \text{Å} = 1.50 \times 10^{12} \, \text{sec}^{-1}$$

$$\frac{2hc}{\lambda^3} = 1.58 \times 10^{-3} \, \text{sec} \cdot \text{cm}^{-2}$$

Therefore,

$$kT = \theta = \frac{1.97}{\ln \left(1 + 45.6 \left(1 - \frac{I_{\omega}}{I_{\omega}^e} \right) \right)} \quad (\text{ev}) \quad \dots 2.8$$

An order of magnitude density estimate was made by assuming that the plasma absorption was due to inverse bremsstrahlung with an average charge multiplicity of the aluminum ions of two³⁵. If the absorbing thickness of the plasma is L, from the discussion above, the plasma absorption coefficient,

$$\alpha = \frac{-\ln \left(I_{\omega} / I_{\omega}^e \right)}{L} = 3.69 \times 10^8 \frac{z^3 n_i^2}{T^{3/2} \nu^3} \left(1 - \exp \frac{-h\nu}{kT} \right) \quad \dots 2.9$$

and,

$$n_i = \left[\frac{- \left(\ln I_{\omega} / I_{\omega}^e \right) \times \theta^{1/2} / L}{1 - \exp \frac{h\nu}{\theta}} \right]^{1/2} \times \frac{3.24 \times 10^{19}}{z^{3/2}} \quad (\text{cm}^{-3}) \quad \dots 2.10$$

The absorption length, L, was estimated to be about 1mm. This was a reasonable figure both from photographic observations of the luminous flare (see section 2.3), and from the observation that the cw laser could be moved about 0.5mm off the axis of the incident giant laser pulse before the absorption signal altered significantly. It can be seen from equation 2.10 that n_i depends only on $L^{1/2}$, thus for an order of magnitude calculation, the actual value adopted for L is not too critical.

The traces of Figure 2.8 were resolved in this manner into estimates of radiation temperature and ion density at various instants after the Q-spoiled laser pulse by solving equations 2.8 and 2.10. The computations were performed on an A.P.L.360 system. These results are shown in Figures 2.9 and 2.10 at 0.5 and 1.0mm from the target surface. At 1.5mm it can be seen with reference to Figure 2.8 that the plasma absorption becomes comparable to the noise level of the cw laser (~1%) thus no analysis was possible for this data.

It can be seen that the radiation temperature obtained in this way falls from a maximum of about 7ev at the end of the Q-spoiled laser pulse (the earliest instant at which the signals were sufficiently large to permit a calculation) to about 2.5ev after 100nsec at which time the rapid temperature decay ceases. A comparison between Figures 2.9 and 2.10 and rough calculations at 1.5mm indicates that the temperature is quite uniform throughout the flare. The existence of a large density gradient at the luminous boundry was indicated by a large difference in plasma absorption between 0.5 and 1.0mm immediately after the laser pulse. The ion density at 0.5mm decays from a maximum of about $1 \times 10^{19} \text{ cm}^{-3}$ at the end of the laser pulse to about $2 \times 10^{18} \text{ cm}^{-3}$ in 150nsec according to the analysis above as is shown in Figure 2.9. The density at 1.0mm remains near $2 \times 10^{18} \text{ cm}^{-3}$ for up to 200nsec after the end of the laser pulse, as is shown in Figure 2.10.

An attempt was made to relate the temperature decay to an adiabatic expansion of the laser-heated plasma. If one assumes that the plasma undergoes an adiabatic expansion, then,

$$TV^{\gamma-1} = T_0 V_0^{\gamma-1} \quad \dots 2.11$$

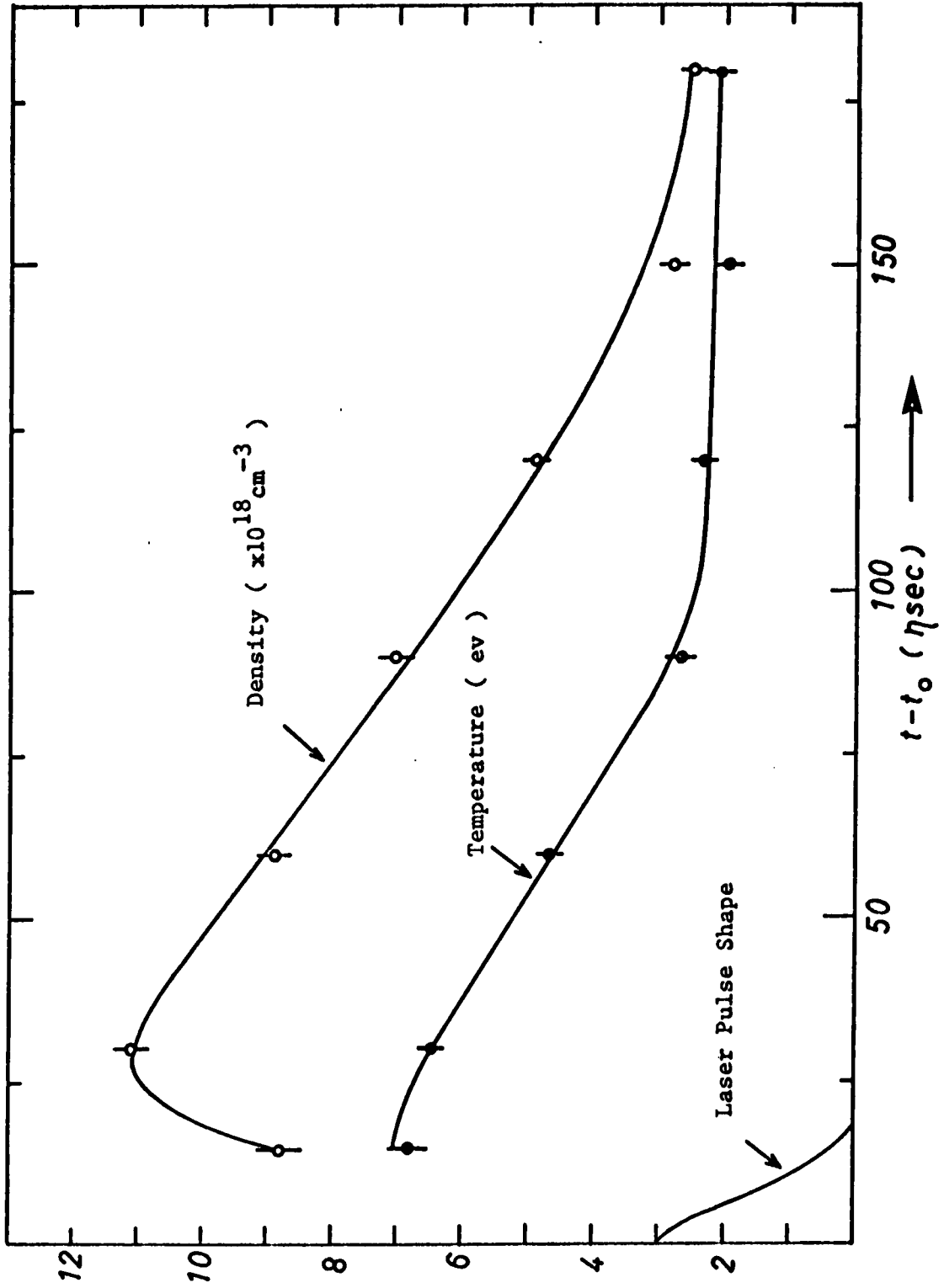


Fig. 2.9 Flare Temperature and Density 0.5mm from the Target Surface.

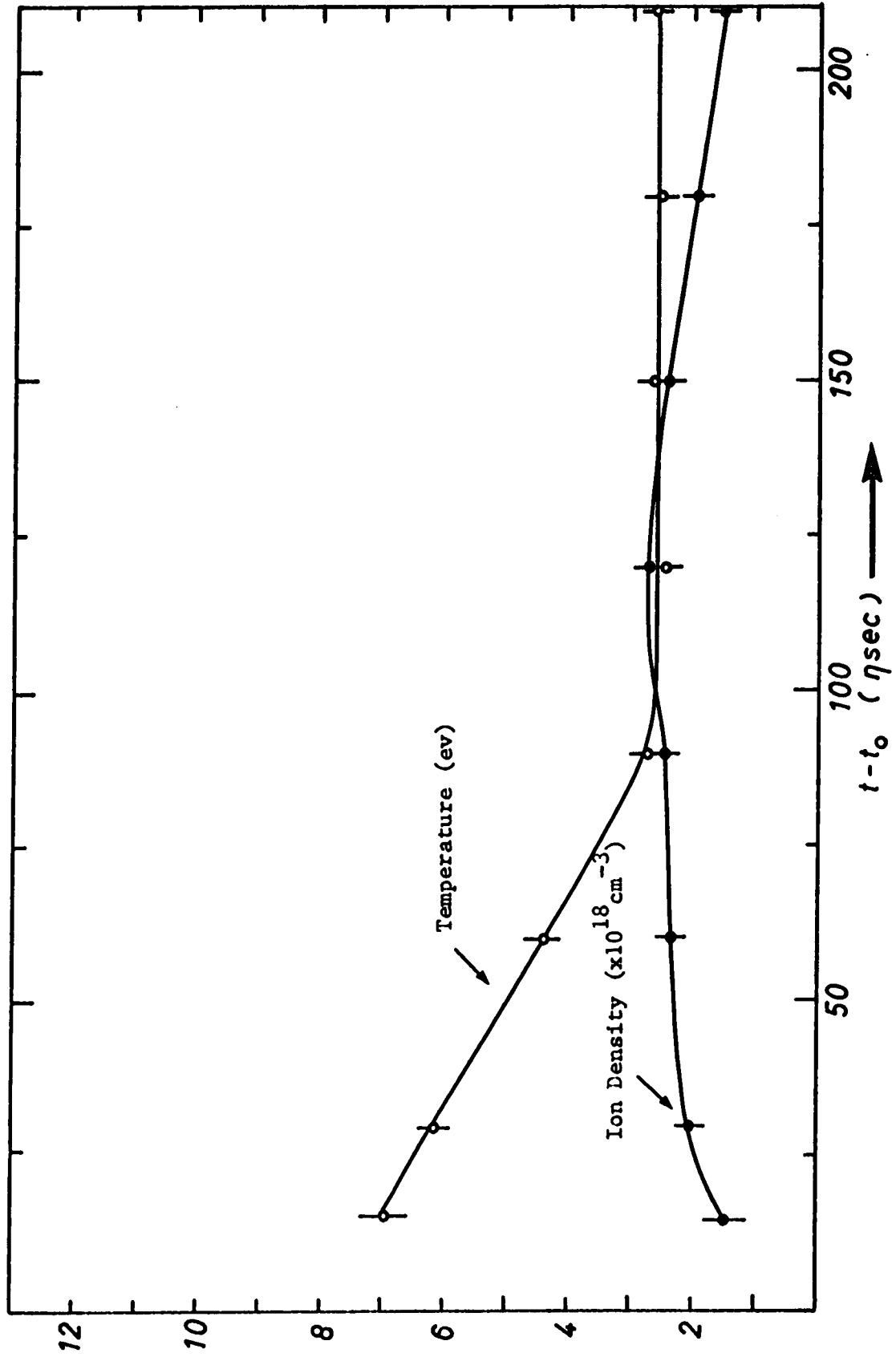


Fig. 2.10 Flare Temperature and Density 1.0mm from Target Surface.

where γ is the adiabatic constant of the plasma. For a completely ionized ideal plasma in free expansion, the adiabatic constant is $\gamma=5/3$. It is known that γ depends strongly on the electronic structure of the plasma ion species, being somewhat less than $5/3$ but still greater than unity for a plasma composed of a partially stripped ion species. The curves of Figure 2.11 depict the temperature decay of a spherical plasma of initial diameter 1.0mm, expanding at 3×10^6 cm/sec, with adiabatic constants of $\gamma=4/3$ and $\gamma=5/3$.

It can be seen that although fair agreement is obtained with $\gamma=4/3$, the temperature does decay somewhat more slowly than predicted by the adiabatic expansion. It may be of course, that the bulk of the plasma expands at a rate somewhat slower than that of the luminous front. (The experimentally observed density decay at 0.5mm is consistent with expansion at about 1×10^6 cm/sec.) The analysis above, however, ignores a possible source of additional energy to the rapidly cooling plasma, that is, ion-electron recombination. In fact, Dawson¹⁰ has speculated that the temperature decay should almost be arrested at some point with recombination just supplying the work done in the expansion. Thus it seems possible that the knee in the measured decay curves at $t-t_0 \approx 75 \text{ nsec}$ is attributable to ionic recombination.

These results can be compared to those of David and Weichel²² for a carbon blowoff plasma formed with a similar laser pulse. By measuring the plasma density interferometrically, and simultaneously measuring the absorption coefficient with an argon ion laser, they found that at incident energy densities of the order of 1000 joules/cm^2 the carbon plasma was in thermal equilibrium with a temperature of less than 10ev at the end of the laser pulse.

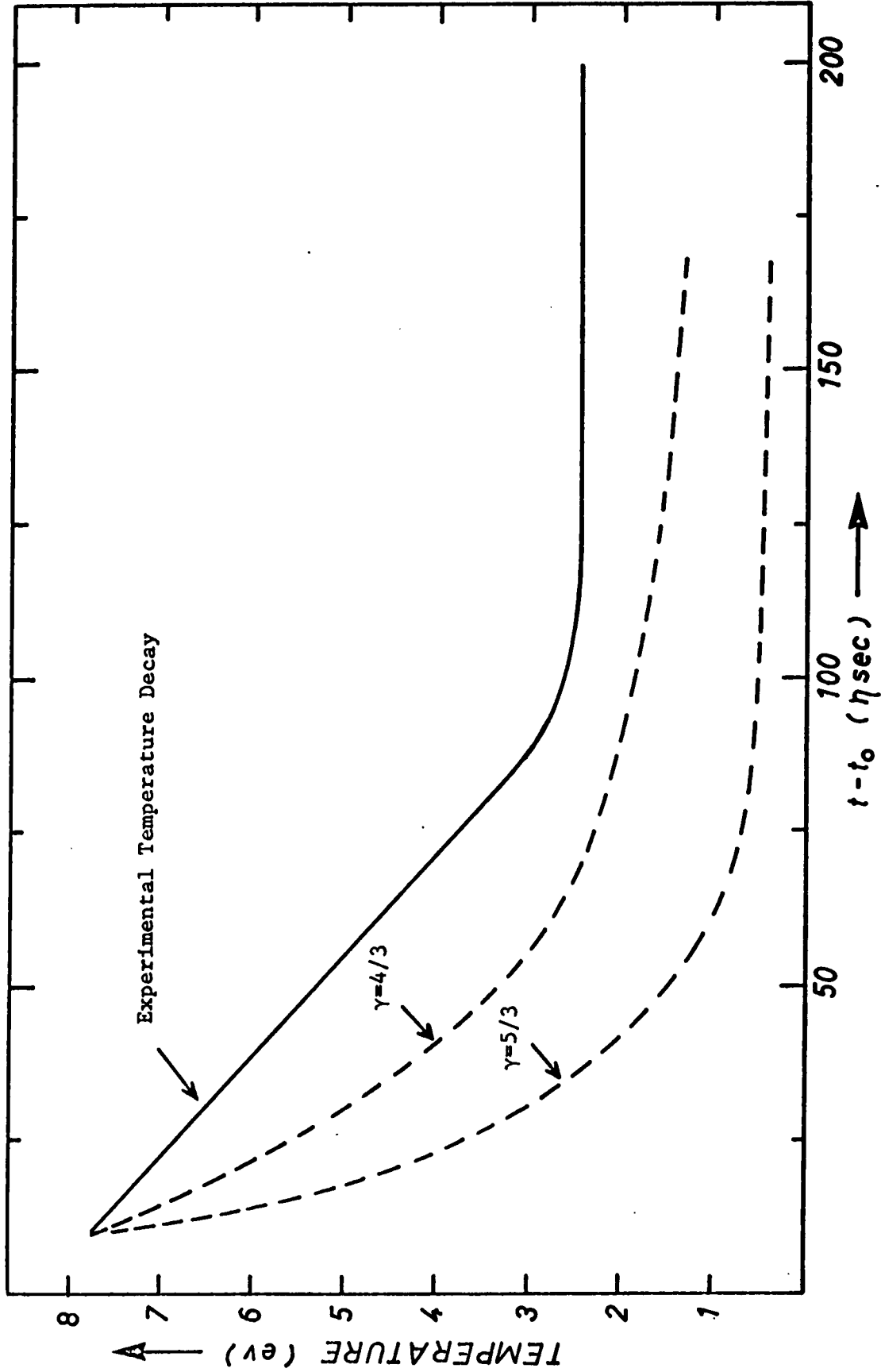


Fig. 2.11 Adiabatic Temperature Decay Profiles.

Although it is estimated that the experimental error in the application of this technique is only about 10% which results mainly from photomultiplier calibration and estimation of the linewidth of the detection system, it is necessary to discuss in more detail some of the limitations of the technique.

A lower limit on the spatial resolution in these measurements can be set as 0.75mm, the aperture of the spatial filter and the total extent of the cw laser at the plasma position. In fact, however, the resolution was slightly better than this. Measurements showed that approximately 80% of the power of the incident cw laser beam was contained in a diameter of 0.5mm at the target position. Calculations on the properties of the spatial filter show that this diameter also furnishes about the same fraction of the area-solid angle integral of the observed plasma cross-section.

Although the analysis assumes a plasma of uniform parameters (n_i, T_e), it can be shown that density gradients in the plane perpendicular to the cw laser beam will not affect the temperature calculation providing the temperature is uniform in this plane (see Appendix A). The curves of Figures 2.9 and 2.10 indicate that this is the case to a good approximation as might be expected due to the high thermal conductivity of a plasma at these temperatures.

The assumption of local thermodynamic equilibrium is basic to the interpretation of the temperature measurement. A common criteria for the applicability of L.T.E. is that the energy transport by collisional processes should be large compared to the transport by radiation and conduction, since the blowoff plasma is characterized by high densities (10^{19} cm^{-3}) and low temperatures (10ev) this condition should be well satisfied.

Spitzer¹ defines three collisional transfer times : the time

for an electron gas that does not initially have a Maxwellian distribution to acquire one, the time required for ions and neutrals to acquire a Maxwellian distribution, and the time required for ions and electrons with Maxwellian distributions at different temperatures to reach the same temperature. For a plasma of the nominal parameters $n_e = 10^{19} \text{ cm}^{-3}$, $\theta_e = 10 \text{ eV}$, these times have been estimated by David and Weichel²² as 10^{-13} , 5×10^{-11} , and 3×10^{-9} sec respectively. Thus it appears that the assumption of L.T.E. is justified and the temperature as measured in this way can be equated to the electron temperature of the plasma.

The charge multiplicity of the aluminum ions has been arbitrarily set at two in order to obtain an order of magnitude density estimate from the absorptivity of the plasma. In fact, the ratio of Al^{3+} to Al^{2+} can be computed from the Saha equation which neglecting the temperature dependence of the partition functions becomes,

$$\frac{n_{3+}}{n_{2+}} = \frac{38.1 \times 10^{20}}{n_e} \theta^{3/2} \exp \frac{-28.4}{\theta} , \quad \dots 2.12$$

where n_e is the electron density in cm^{-3} and θ is the electron temperature in eV. Thus, for an equilibrium plasma with an electron density of $n_e \approx 10^{19} \text{ cm}^{-3}$, the $\text{Al}^{3+} - \text{Al}^{2+}$ transition corresponds to an electron temperature of about 3 eV. Thus, the leveling off of the temperature decay at 2.5 eV as discussed above, and which has been attributed to plasma recombination is consistent with this transition.

2.5 Electrostatic Probe Measurements.

The plasma temperature near the target surface as measured by the preceding technique is an order of magnitude lower than what might be expected at the end of the Q-spoiled laser pulse, on the basis of energy delivered per plasma particle (see Section 2.2). This suggests that during the time interval of these measurements, most of the plasma energy is manifested as directed kinetic energy associated with the plasma expansion.

The emission of high energy ions from laser-solid interaction was established in the very early experiments on this phenomenon. Typically, these ions have been detected by scintillation counters or Faraday cup probes and their energies estimated on a time of flight basis. In this section, the design of two types of charge collection probes and their application to the study of the properties of the fast ionization front will be discussed. The first of these was a simple Faraday cup attached to the wall of the vacuum chamber. The second was a movable double electrostatic probe biased to collect saturation ion current.

1. The Faraday cup wall probe. Details of this device are shown in Figure 2.12. It was terminated in a standard BNC connector to which was attached a 500Ω load. The device was connected to a Tektronix 555 oscilloscope through five feet of RG58U cable. The capacitance of the probe plus connecting cable was measured to be $190\mu\text{F}$. Thus, the time response of the probe to current fluctuations was about 10nsec .

The current to the wall probe after the impact of the laser on the aluminum target is shown in Figure 2.13. The arrival of the plasma front at the vacuum chamber wall was signaled by a sharp negative current pulse, approximately 440nsec after the laser pulse, amounting to about 15 mamp

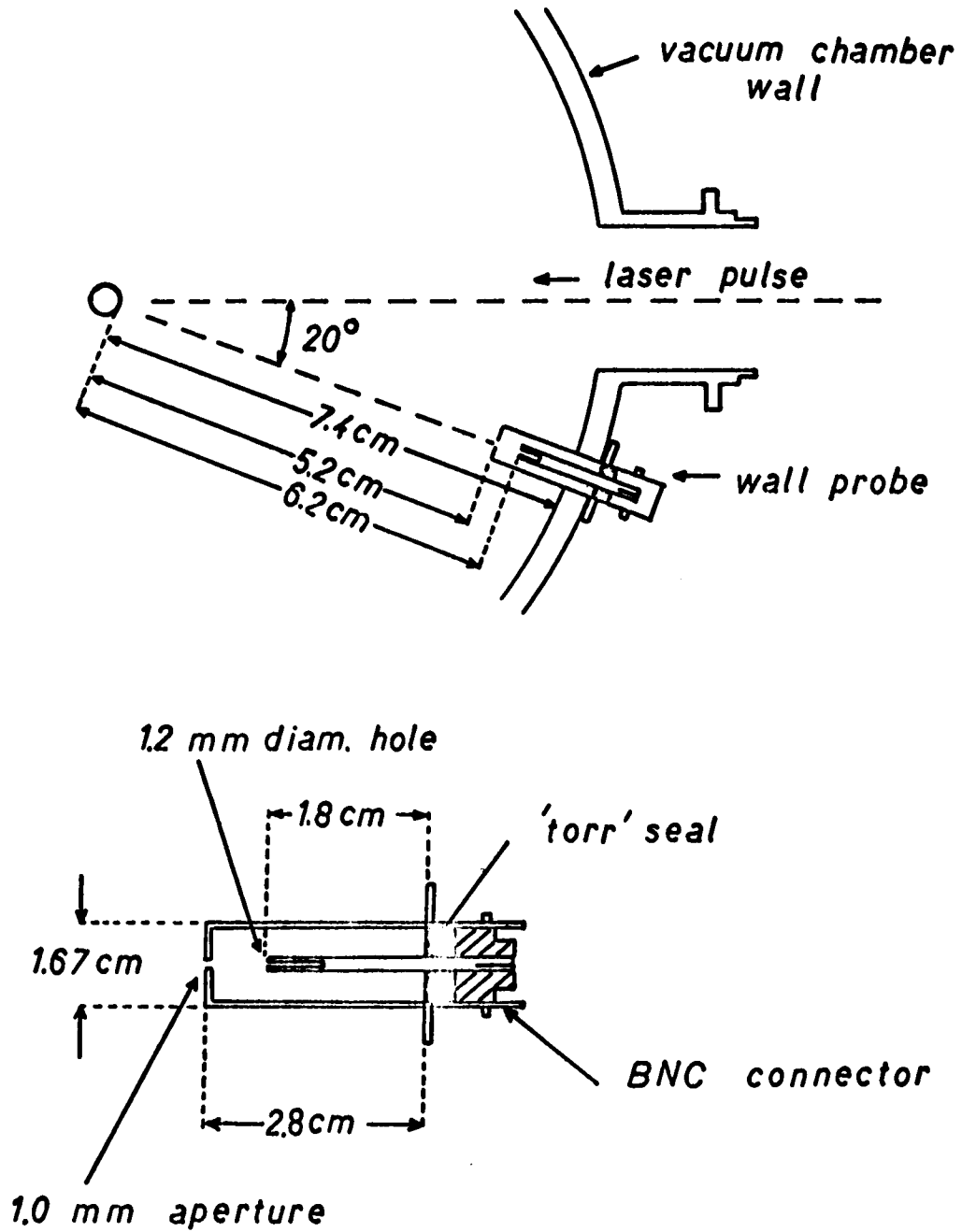


FIG. 2.12 WALL PROBE DETAILS

at its maximum. After about $1.5\mu\text{sec}$, the probe current became slightly positive for the remainder of the event. Qualitatively similar unbiased Faraday cup probe signals have been observed by Basov et al²⁰ and Opower and Press²⁹. The form of this signal has been attributed to a negative space charge at the plasma surface caused by the initially more rapidly moving plasma electrons.

The velocity of the plasma front can be calculated from the time required for it to reach the probe as approximately $1.4 \times 10^6 \text{ cm/sec}$, corresponding to aluminum ion energies of about 2800ev.

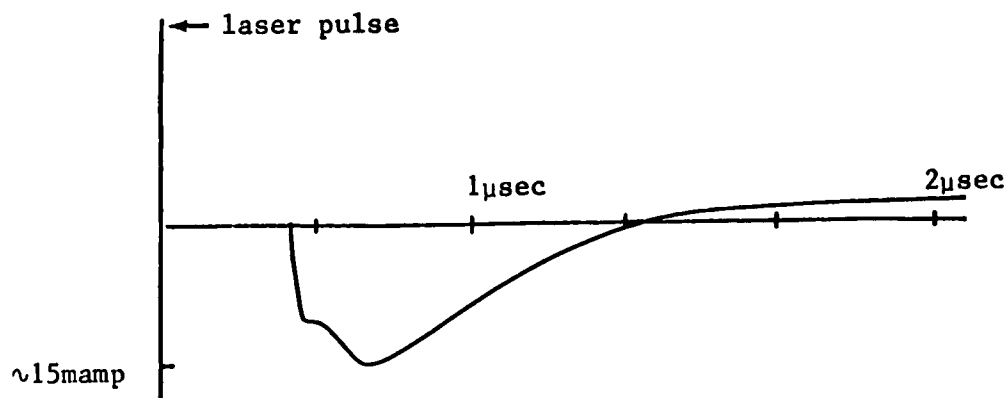


Fig. 2.13 Wall Probe Signal.

2. The double electrostatic probe. To investigate in more detail the structure of this fast ionization front, a movable double Langmuir probe was used. This probe consisted of two tungsten electrodes about 1mm apart, sealed into a 5mm diameter glass tube and inserted into the vacuum system through the probe port shown in Figure 1.6. A typical probe of this type and its biasing circuit is shown in Figure 2.14.

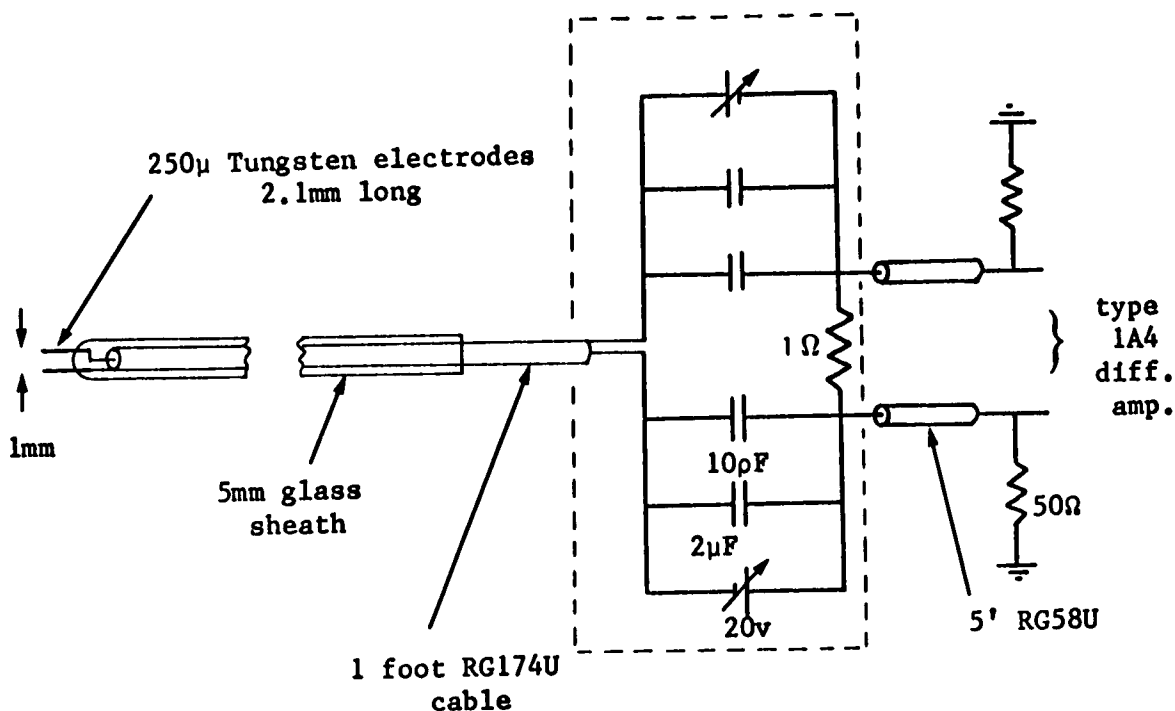


Fig. 2.14 Biased Double Electrostatic Probe.

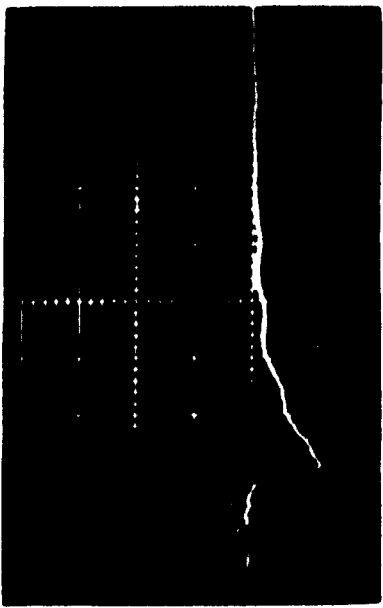
The probe circuit was estimated to have an inductance of about 10^{-8} henry. Assuming a plasma impedance of the order of 100Ω , the time response of the probe was thus limited to a few nanoseconds. The probe signals were displayed on a type 555 oscilloscope through a 1A4 vertical amplifier, allowing the output of the laser monitoring photodiode to be added onto the differential signal as a timing reference. Typical probe signals for a probe of the dimensions shown in Figure 2.14 are reproduced in Figure 2.15, for a 12v bias, at various distances from the target surface.

The normal collisionless theory of ion collecting probes in a quiescent plasma³⁶ predicts a saturation ion current of the form,

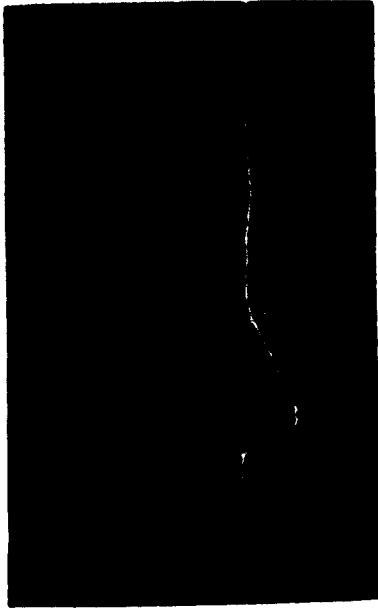
$$I_s \approx \frac{q_i n_i A_p}{2} \left[\frac{kT_e}{m_i} \right]^{1/2}, \quad \dots 2.13$$

with,

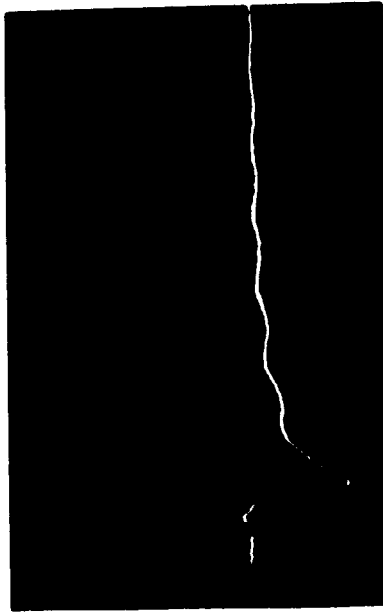
$$\frac{dI}{dV}_0 \approx \frac{e}{kT_e} \left(\frac{1}{2} I_s \right), \quad \dots 2.14$$



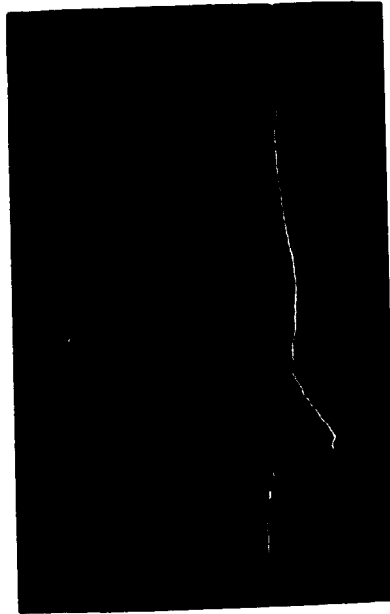
$R = 3.0 \text{ cm}$ 0.2 amp/div



$R = 4.0 \text{ cm}$ 0.1 amp/div



$R = 1.5 \text{ cm}$ 0.5 amp/div



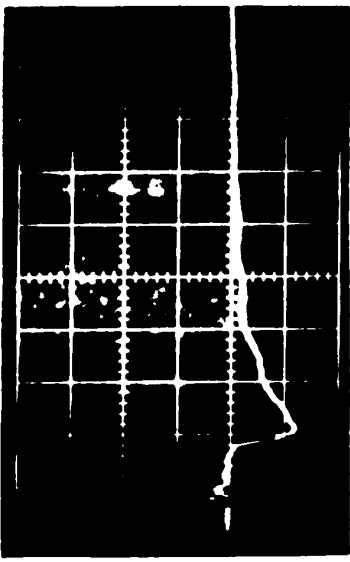
$R = 2.0 \text{ cm}$ 0.5 amp/div

200 nsec/div \rightarrow

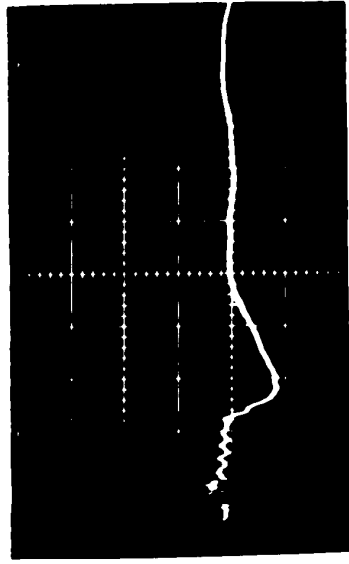
$\text{PROBE AREA: } 1.67 \times 10^{-2} \text{ cm}^2$

$\text{BIAS: } 12 \text{ v}$

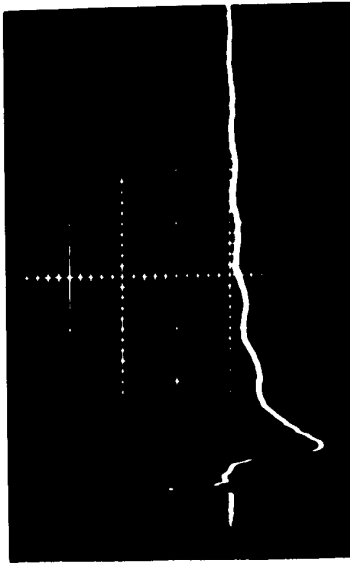
FIG. 2.15 ION CURRENT WAVEFORMS TO DOUBLE PROBE



$R = 3.0 \text{ cm}$ 0.2 amp/div



$R = 4.0 \text{ cm}$ 0.1 amp/div
 $\text{BIAS: } 12 \text{ V}$



$R = 1.5 \text{ cm}$ 1.5 amp/div



200 nsec/div \rightarrow

$R = 2.0 \text{ cm}$ 0.5 amp/div

$\text{PROBE AREA: } 1.67 \times 10^{-2} \text{ cm}^2$

FIG 2.15 ION CURRENT WAVEFORMS TO DOUBLE PROBE

where A_p is the probe area.

The situation in the present case is somewhat complicated by the high flow velocity of the plasma past the probe. In order to detect any effect of the plasma flow on these measurements, three probes of the dimensions shown in Table 2.2 were used.

Probe	Diameter	Length	Tip Area	Total Area
1	0.61mm	1.2mm	$0.30 \times 10^{-2} \text{ cm}^2$	$2.59 \times 10^{-2} \text{ cm}^2$
2	0.25mm	1.6mm	$0.03 \times 10^{-2} \text{ cm}^2$	$1.29 \times 10^{-2} \text{ cm}^2$
3	0.25mm	2.1mm	$0.03 \times 10^{-2} \text{ cm}^2$	$1.67 \times 10^{-2} \text{ cm}^2$

Table 2.2 Dimensions of the Double Probes.

One would expect the simple relations given above to apply providing the (probe tip area)x(the flow velocity) were much less than (the total probe area)x(the ion sound velocity). For ions at a temperature of a few ev flowing at 10^7 cm/sec, this is well satisfied for probes 2 and 3 but marginal for probe 1.

In fact, for all of these probes it was found that the current traces were of the same form and that the magnitude of the probe current was directly proportional to the total probe area. It was observed that the probe current saturated at a bias of a few volts and that the form of the signal was quite reproducible after the fresh probe had been exposed to several shots.

The magnitude of the ion current at 1.5cm from the target surface is shown in Figure 2.16 at the position behind the front corresponding to its maximum value, as a function of bias voltage. Assuming the alum-
edge
inum ions comprising the leading/of the flare to be triply ionized, it

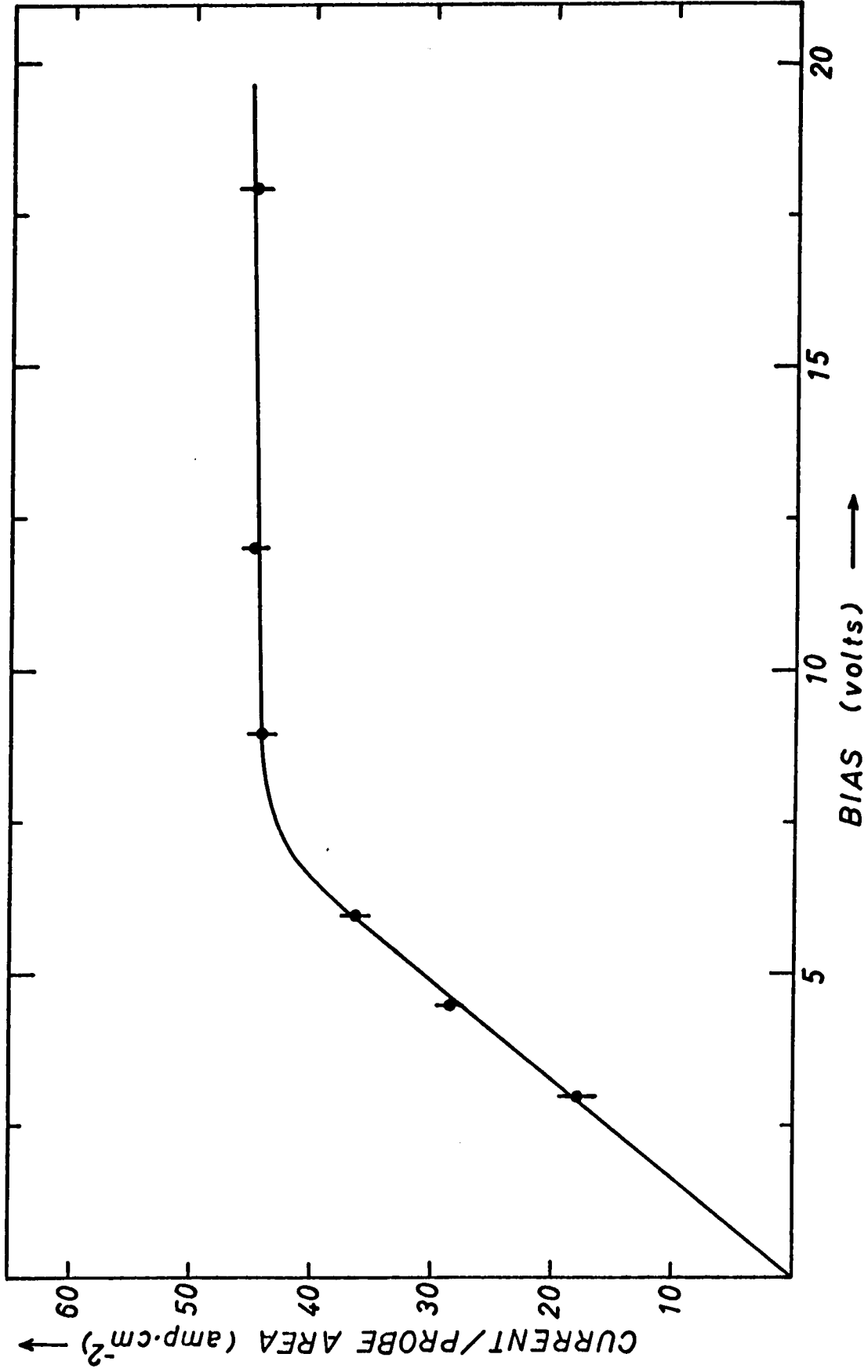


Fig. 2.16 Current-Voltage Characteristics of the Double Electrostatic Probes.

can be seen that, on the basis of the simple probe theory above, this curve corresponds to an ion density of about $5 \times 10^{14} \text{ cm}^{-3}$ and an electron temperature of about 3ev.

A crude estimate of the total number of energetic ions and electrons emitted during the blowoff process and the amount of energy they carry can be obtained by integrating the saturation ion current signals of Figure 2.15. If it is assumed that these particles are emitted isotropically over a solid angle of 2π steradians, we have,

$$\begin{aligned} N_T &= \int (z + 1) n_i v (2\pi R^2) dt \\ &= \int (z + 1) n_i \frac{R}{t} (2\pi R^2) dt \end{aligned} \quad \dots 2.15$$

where R is the distance from the target surface at which the measurement is made. These calculations indicate that there are about 3×10^{16} particles (assuming $z=3$) in the energy range of 500-3000ev. Thus on an order of magnitude basis these particles can account for the total Q-spoiled laser energy ($1.25 \times 10^{19} \text{ ev}$).

The position of the edge of the plasma front as a function of time is shown in Figure 2.17 as obtained from the movable probe data. It can be seen that the plasma front expands at a constant velocity of about $1.43 \times 10^7 \text{ cm/sec}$, in good agreement with that obtained from the Faraday cup wall probe.

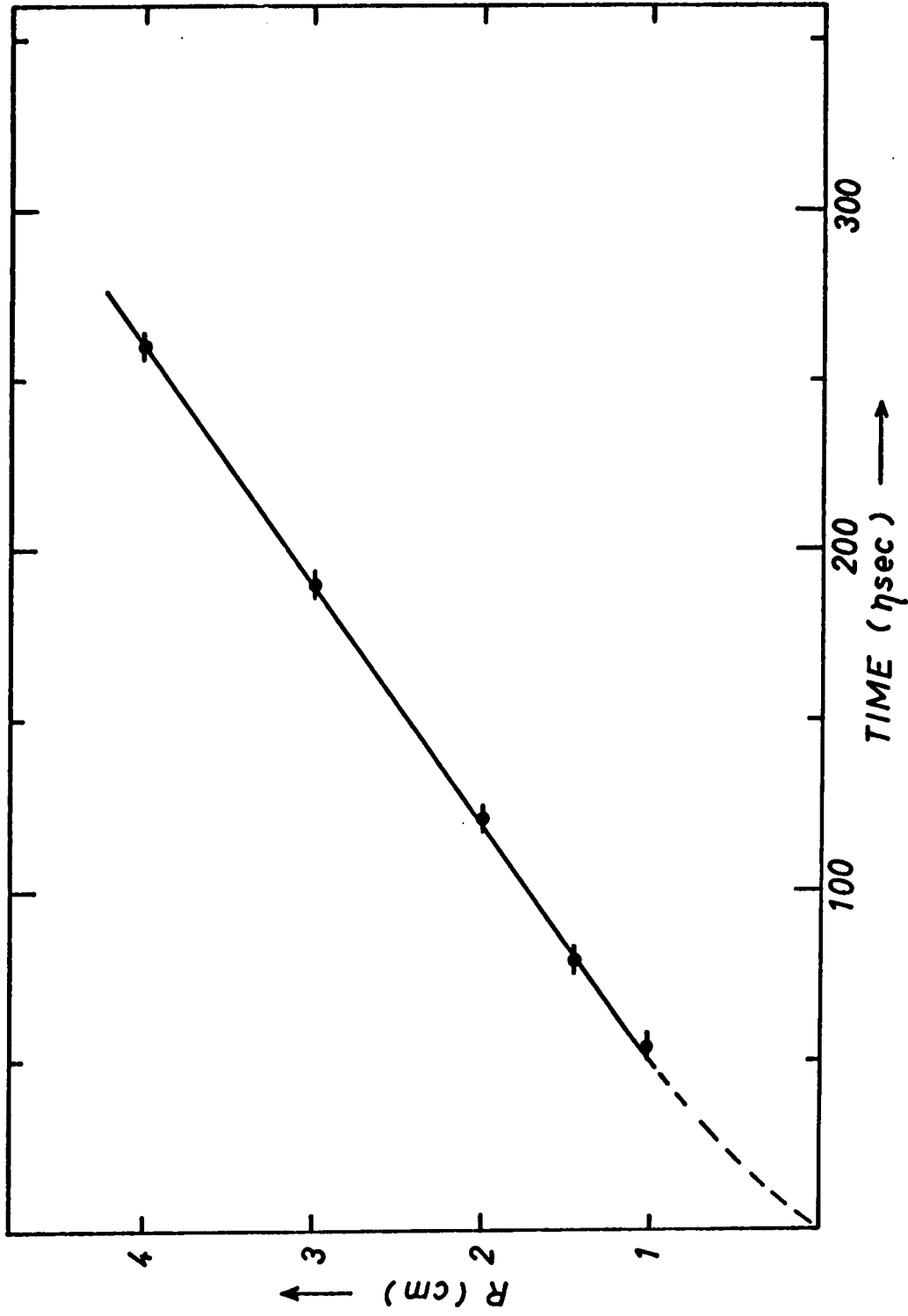


Fig. 2.17 Position of the Leading Edge of the Ionization Front vs. Time.

CHAPTER 3 A SIMPLE PLANAR MODEL OF THE HEATING AND HYDRODYNAMIC EXPANSION OF A LASER-BLOWOFF PLASMA

Dawson¹⁰ considered the heating of an initially ionized drop of solid matter by Q-spoiled laser radiation using a coupled set of hydrodynamic equations with plasma parameters averaged with respect to the gas mass. His results show that for the most readily obtainable laser pulse durations (~ 10 nsec), the maximum temperatures obtained in this case are limited by the hydrodynamic expansion (m_1) of the laser heated plasma, rather than the incident laser energy.

Dawson's theory has been used to relate the expansion velocity of a laser-blowoff plasma to the initial temperature in the flare²⁸. This approach, however, makes several assumptions which do not appear to be applicable to the laser-blowoff geometry. The most objectionable of these are: (a) spherical symmetry - In the laser-blowoff case the expansion in the initial stages at least, will be one dimensional because of the plasma-target interface; (b) constant plasma mass - In the blowoff case the plasma-target interface will serve as a particle source during the interaction process; (c) homogeneous spatial density - In blowoff plasmas large density gradients are expected to exist at the plasma-target interface.

In this chapter, the formulation and numerical solution of a single fluid, one dimensional model which to a large extent overcomes these objections will be presented and compared to the experimental observations of the aluminum blowoff plasma reported in Chapter 2.

3.1 The Model

The following model of the blowoff process was adopted. The incident laser light was assumed to be initially absorbed in a thin layer at the solid surface of the order of the skin depth at solid densities², approximately 10^{-4} cm. This layer was assumed to undergo a planar similarity expansion³ and to remain self-regulating throughout the process in the sense that sufficient mass was constantly added to keep the flare optically thick¹¹. The self-regulated flare was assumed to be in thermal equilibrium with uniform temperature throughout the expansion. The role of plasma re-radiation, reflection, and energy losses to the solid target was assumed to be negligible in the energy balance of the heating process. The energy required to vapourize the solid target material was also neglected.

The density profile of the sheet plasma was assumed to be of the form,

$$n_1(x) = n_0 \left[1 - \left(\frac{x}{R} \right)^\alpha \right] \quad \dots 3.1$$

Assuming that the density profile remains time invariant (similarity expansion), we have³,

$$dx/dt = \left(\frac{x}{R} \right) dR/dt . \quad \dots 3.2$$

The equation of motion of the plasma slab can be obtained by applying Newton's second law to a fluid element (see Fig. 3.1).

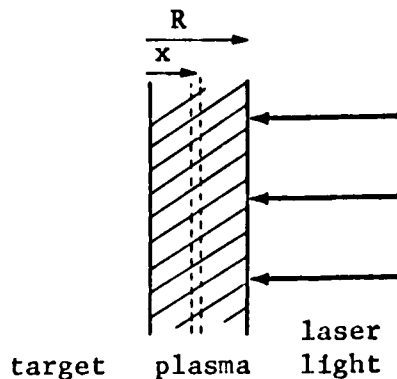


Fig. 3.1 One Dimensional Plasma Slab.

We have,

$$-\int_0^R \frac{\partial P}{\partial x} \frac{dx}{dt} dx = \frac{1}{2} \int_0^R n_i m_i \frac{d}{dt} \left(\frac{dx}{dt} \right)^2 dx, \quad \dots 3.3$$

where for a uniform temperature plasma with ions of charge multiplicity z ,

$$P = (z+1) n_i kT. \quad \dots 3.4$$

Equations 3.1 - 3.4 can be combined to give the equation of motion of the plasma slab⁷,

$$\frac{d^2 R}{dt^2} = \frac{3(\alpha+3)}{(\alpha+1)} \frac{(z+1) \theta}{m_i R}. \quad \dots 3.5$$

We also have the energy balance equation,

$$\frac{d}{dt} \int_0^R \frac{3}{2} (z+1) n_i kT dx = \int_0^R \frac{\partial P}{\partial x} \frac{dx}{dt} dx + W - \frac{d}{dt} [N_s \chi_z], \quad \dots 3.6$$

where W represents the incident laser flux, N_s , the total number of atoms vapourized, and χ_z , the energy required to ionize an atom to the z^{th} stage.

N_s is given by,

$$N_s = \int_0^R n_0 \left(1 - \left(\frac{x}{R} \right)^\alpha \right) dx = n_0 R \left[\frac{\alpha}{\alpha+1} \right]. \quad \dots 3.7$$

Equation 3.6 then reduces to,

$$\frac{3}{2} \frac{d}{dt} [N_s \theta] + N_s \frac{\theta}{R} \frac{dR}{dt} = \frac{W}{z+1} - \frac{\chi_z}{z+1} \frac{d}{dt} (N_s). \quad \dots 3.8$$

Using Dawson's¹⁰ formula for the inverse bremsstrahlung absorption coefficient, the requirement of self-regulation can be formulated as,

$$\int_0^R k_L(x) dx \approx 1, \quad \dots 3.9$$

where,

$$k_L(x) = 7.50 \times 10^{-38} \frac{z^3 n_i^2}{\theta^{3/2}} \quad \dots 3.10$$

this reduces in combination with 3.1 and 3.7 to,

$$7.50 \times 10^{-38} \frac{z^3}{\theta^{3/2}} \frac{N_s^2}{R} \frac{2(\alpha+1)}{2\alpha+1} = 1 \quad \dots 3.11$$

Equations 3.5, 3.8, and 3.11 form a coupled set of equations which may be solved for $N_s(t)$ (proportional to the depth of the target fissure), $\theta(t)$ (flare temperature), and $R(t)$ (flare thickness). A numerical solution is facilitated by placing these equations in the form:

$$\frac{dR}{dt} = v \quad \dots 3.12$$

$$\frac{dv}{dt} = \frac{k_2 \theta}{R} \quad \dots 3.13$$

$$\frac{d\theta}{dt} = \frac{k_1 W - 7/4 k_3^{1/2} R^{-1/2} \theta^{7/4} v - 1/2 \frac{\chi_z}{z+1} k_3^{1/2} R^{-1/2} \theta^{3/4} v}{21/8 k_3^{1/2} R^{1/2} \theta^{3/4} + 3/4 \frac{\chi_z}{z+1} k_3^{1/2} R^{1/2} \theta^{-1/4}} \quad \dots 3.14$$

$$N_s = K_3^{1/2} R^{1/2} \theta^{3/4} \quad \dots 3.15$$

where:

$$k_1 = \frac{1}{1.602 \times 10^{-12} (z+1)},$$

$$k_2 = \frac{3(\alpha+3)}{\alpha+1} \frac{(z+1)}{m_i} 1.602 \times 10^{-12},$$

$$k_3 = \frac{(2\alpha+1)}{2(\alpha+1) z^3} 7.5 \times 10^{-38},$$

with the following choice of units:

$$\begin{array}{ll} \theta & - \text{ ev} & m_i & - \text{ gm} \\ R & - \text{ cm} & \chi_z & - \text{ ev} \\ W & - \text{ erg/sec. cm}^2 & & \end{array}$$

The laser pulse was approximated by a modified Gaussian curve of the form,

$$W = A \exp\left(\frac{-1}{2} \left[\frac{t - 12 \times 10^{-9}}{6 \times 10^{-9}}\right]^2\right) \quad ; \quad t > 6 \times 10^{-9} \text{ sec}$$

$$W = A \left[\exp\left(-\frac{1}{2}\right)\right]^{\frac{t}{6 \times 10^{-9}}} \quad ; \quad t < 6 \times 10^{-9} \text{ sec} \quad \dots \quad 3.16$$

The constant A was chosen to correspond to a 130Mw laser pulse focused uniformly over a 300 μ diameter focal spot. The shape of this curve is shown in Figure 3.2.

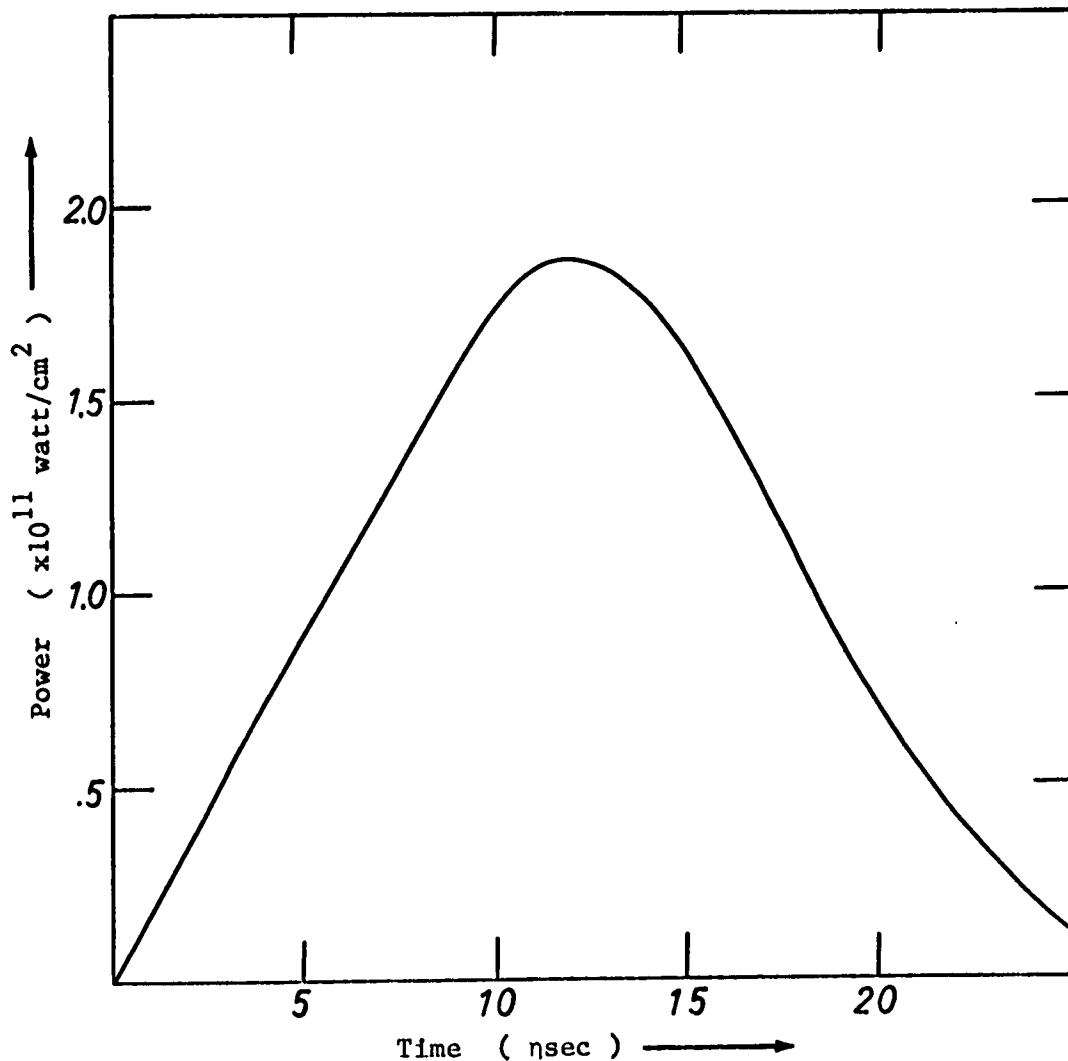


Fig. 3.2 Assumed Laser Pulse Shape.

Since the system of equations 3.12 - 3.15 describe only the properties of the self-regulated plasma flare, and not the actual laser-solid interaction mechanism, the numerical solution must be started by assuming that a plasma layer already exists at $t=0$. It might be expected that since these are basically conservation equations, the solution should not depend on the initial conditions so long as the initial plasma layer contains a small number of ions compared to the total number that will be vapourized by the laser pulse. This feature has been verified in the numerical solutions by assuming a wide range of initial conditions and observing that the solutions converge after a few thousandths of a nanosecond. A physically plausible set of initial conditions can be formulated as follows: For ruby laser light, $\nu_L = 4.35 \times 10^{14} \text{ sec}^{-1}$, the critical plasma density ($\nu_L = \nu_p$) is, $n_{ec} = 2.3 \times 10^{21} \text{ cm}^{-3}$ (density of solid Al = $2.4 \times 10^{22} \text{ cm}^{-3}$). At the critical density, the absorption depth is about 10^{-4} cm (see for example reference 2), therefore we can assume that the laser light initially interacts with a thin surface layer of the solid target (by multiphoton absorption), this layer is heated and expands until $n_e < n_{ec}$ at which time strong inverse bremsstrahlung absorption can occur within a layer of the order of 10^{-4} cm and a self-regulating regime can be established (O'power et al² estimate that this will occur in about 10^{-12} sec). Since the absorption coefficient in equation 3.10 is only applicable for θ greater than about one eV, it is plausible to assume initial conditions of the order: $\theta_0 = 1 \text{ eV}$; $R_0 = 10^{-4} \text{ cm}$; $V_0 = 0$.

3.2 The Numerical Solution

For the purposes of numerical solution, it was assumed that the level of ionization, z , was a constant and that the initial conditions were those outlined above. The actual computation was performed on an I.B.M. 360 computer, using S.S.P. subroutine DRKGS, a fourth order Runge-Kutta technique. Solutions were obtained for z in the range of three to seven, and density profile parameters, $\alpha = 1$ (linear density profile), $\alpha = 2$ (parabolic), and $\alpha = 10$ (approximately uniform density). Values of χ_z were chosen to correspond to the ionization energies of aluminum, that is, $\chi_3 = 53.2$, $\chi_4 = 173$, $\chi_5 = 327$, $\chi_6 = 517$, and $\chi_7 = 757\text{ev}$.

As might be inferred from the form of equations 3.12 - 3.15, the solutions were found to be relatively insensitive to the profile parameter α . Computed solutions up to $t = 17\text{nsec}$, for $z = 3$; $\alpha = 1, 2$ and 10 are shown in Figures 3.3 - 3.6 for R , V , θ , and depth of target fissure respectively. It can be seen that α affects only R and V and that even for these quantities, the dependence on α is not great. The specific energy curve of Figure 3.5 denotes the total laser energy delivered per plasma particle (ions and electrons), minus the ionization energy.

Somewhat more surprising, is the absence in the computed solutions for R , V , and θ of any strong dependence on z . Figures 3.7 - 3.9 depict these quantities with $\alpha = 10$; $z = 3$, and $z = 7$. The effect of ion charge multiplicity on the depth of the target fissure is shown in Figure 3.10, also with $\alpha = 10$ (this quantity was almost independent of α).

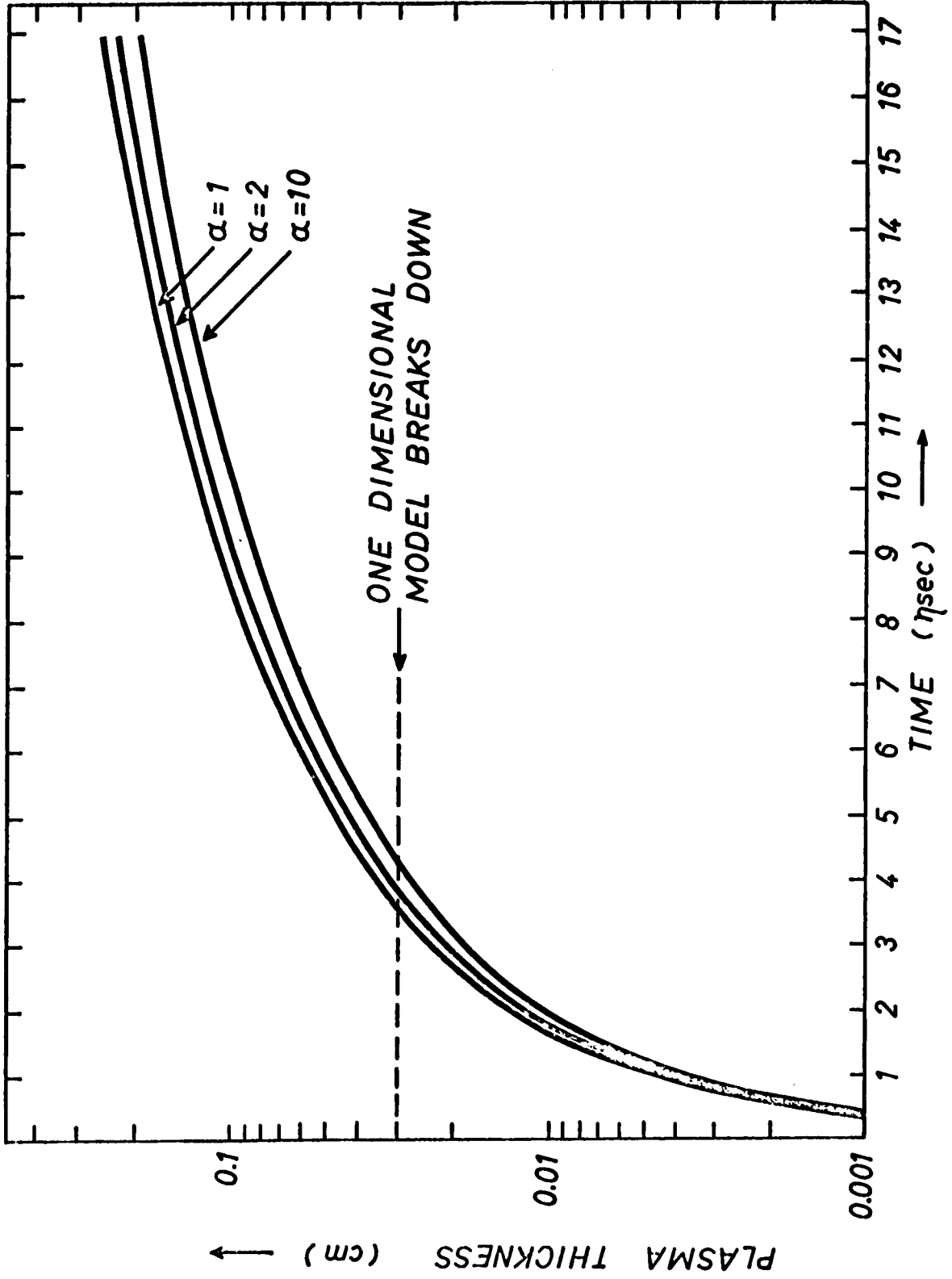


Fig. 3.3 Plasma Thickness as a Function of Time for $z = 3$; $\alpha = 1, 2, \text{ and } 10$.

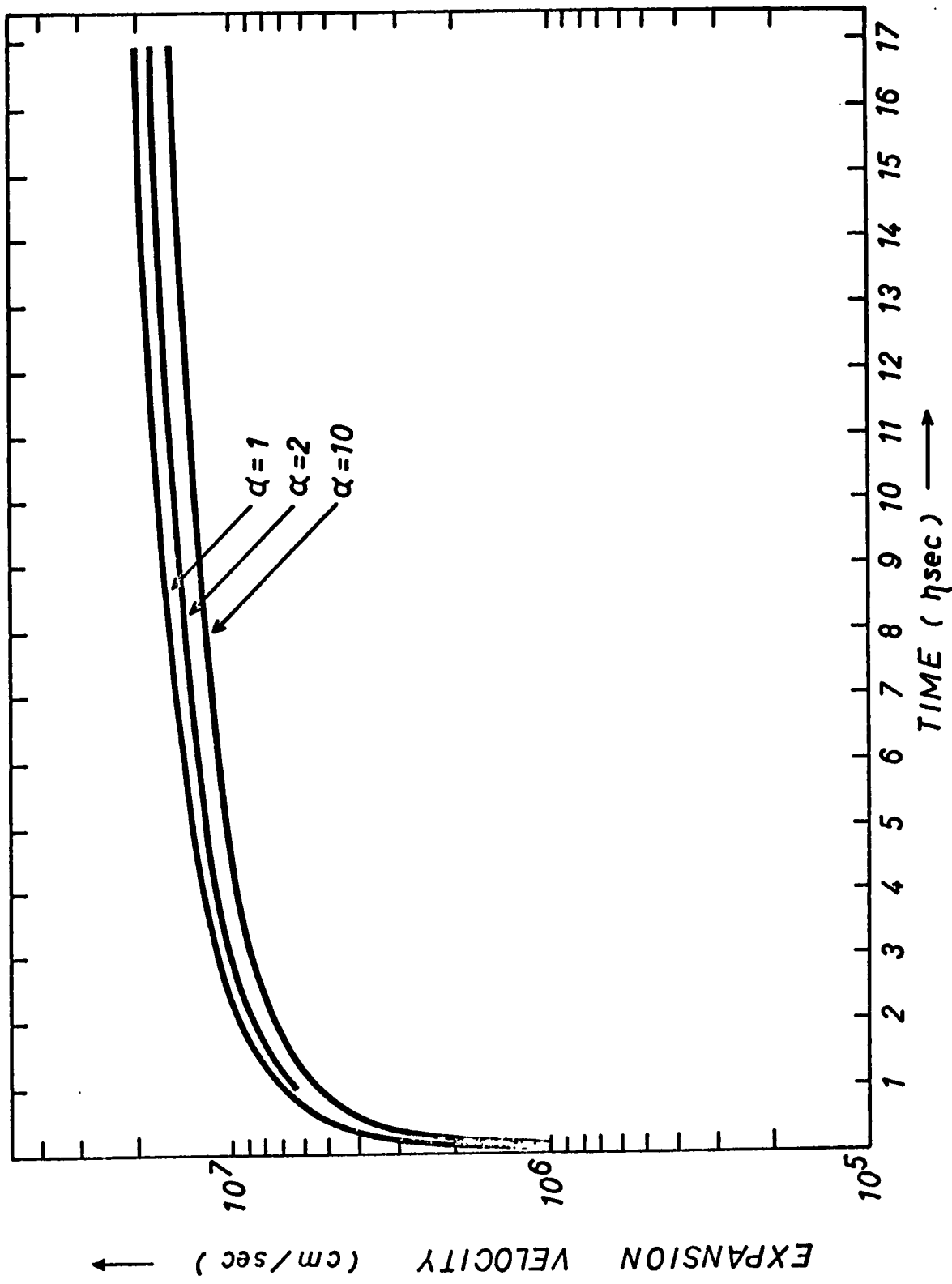


Fig. 3.4 Expansion Velocity of the Leading Edge of the Plasma for $z = 3$; $\alpha = 1, 2,$ and 10 .

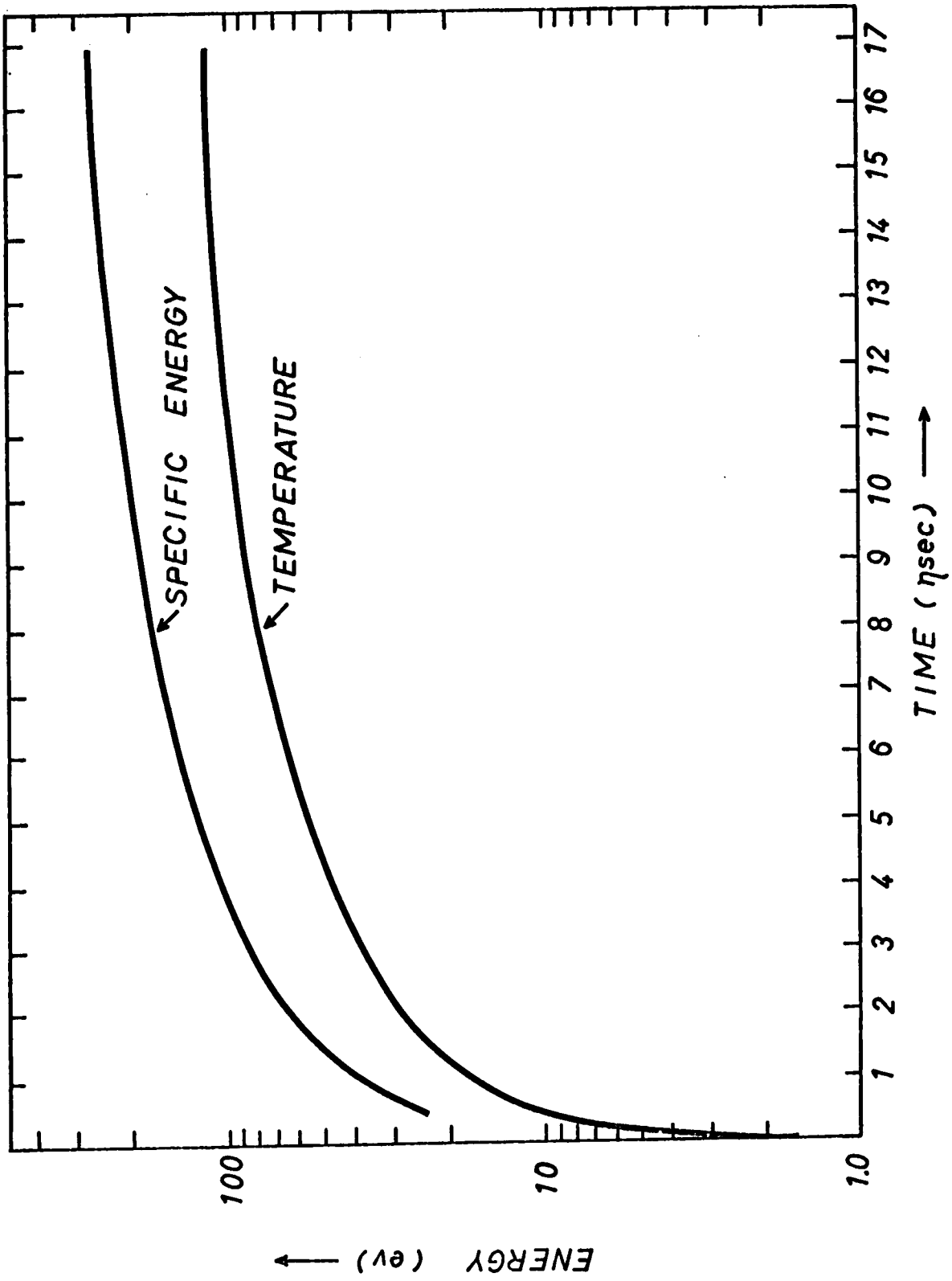


Fig. 3.5 Plasma Temperature and Specific Energy for $z = 3$; $\alpha = 1, 2,$ and 10 .

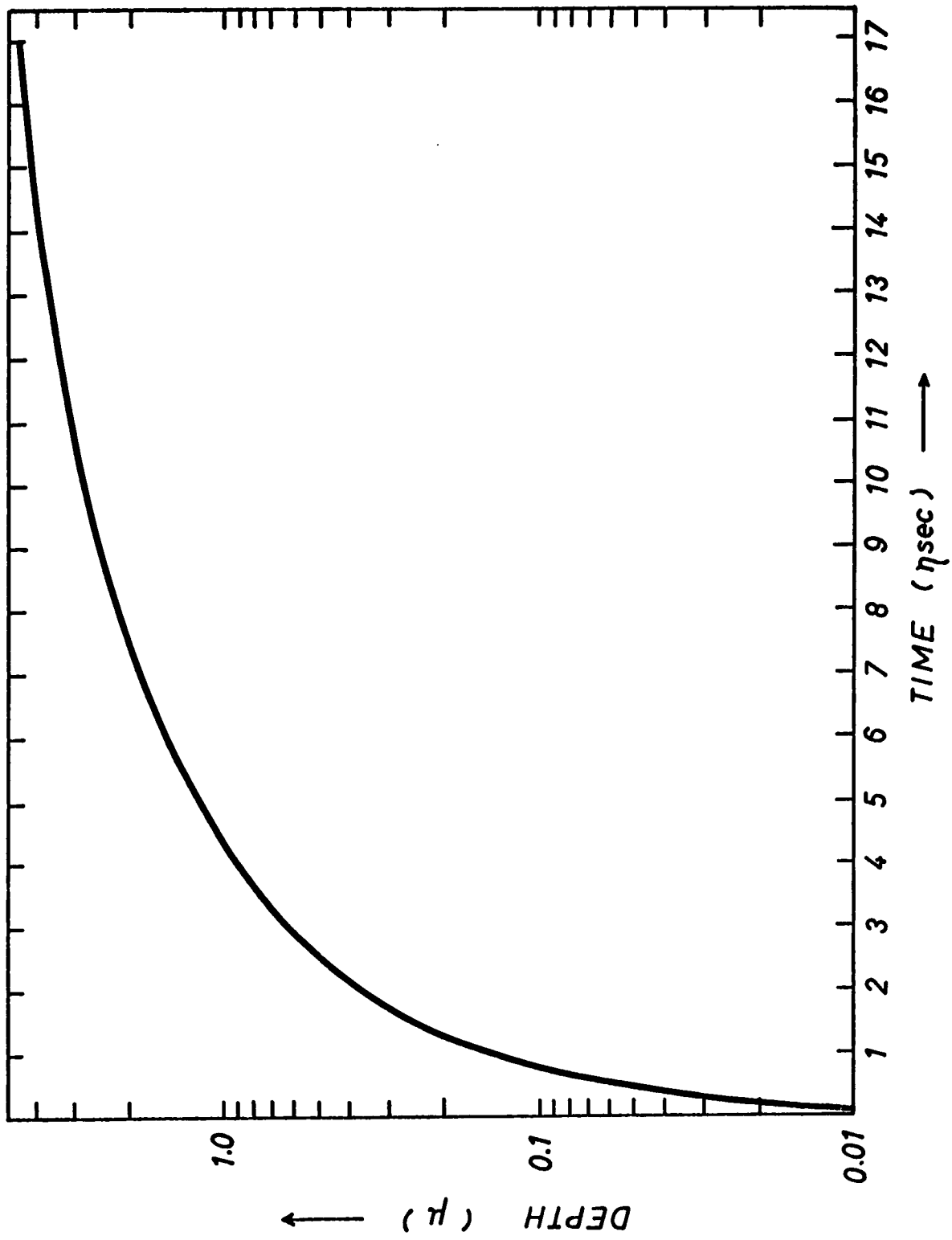


Fig. 3.6 Depth of Target Fissure for $z = 3$; $\alpha = 1, 2, \text{ and } 10$.

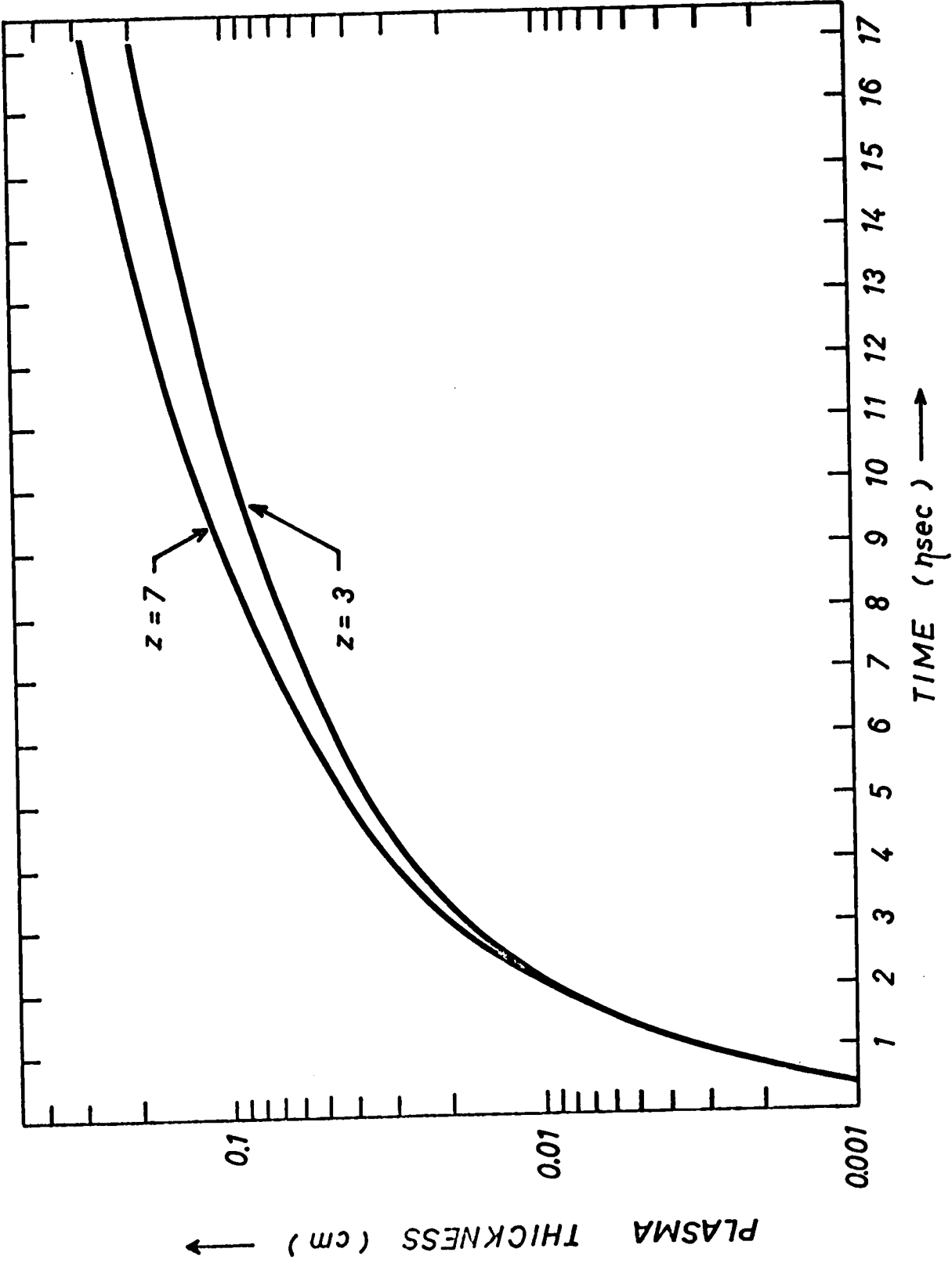


Fig. 3.7 Effect of Ion Charge Multiplicity on Plasma Thickness ($\alpha = 10$).

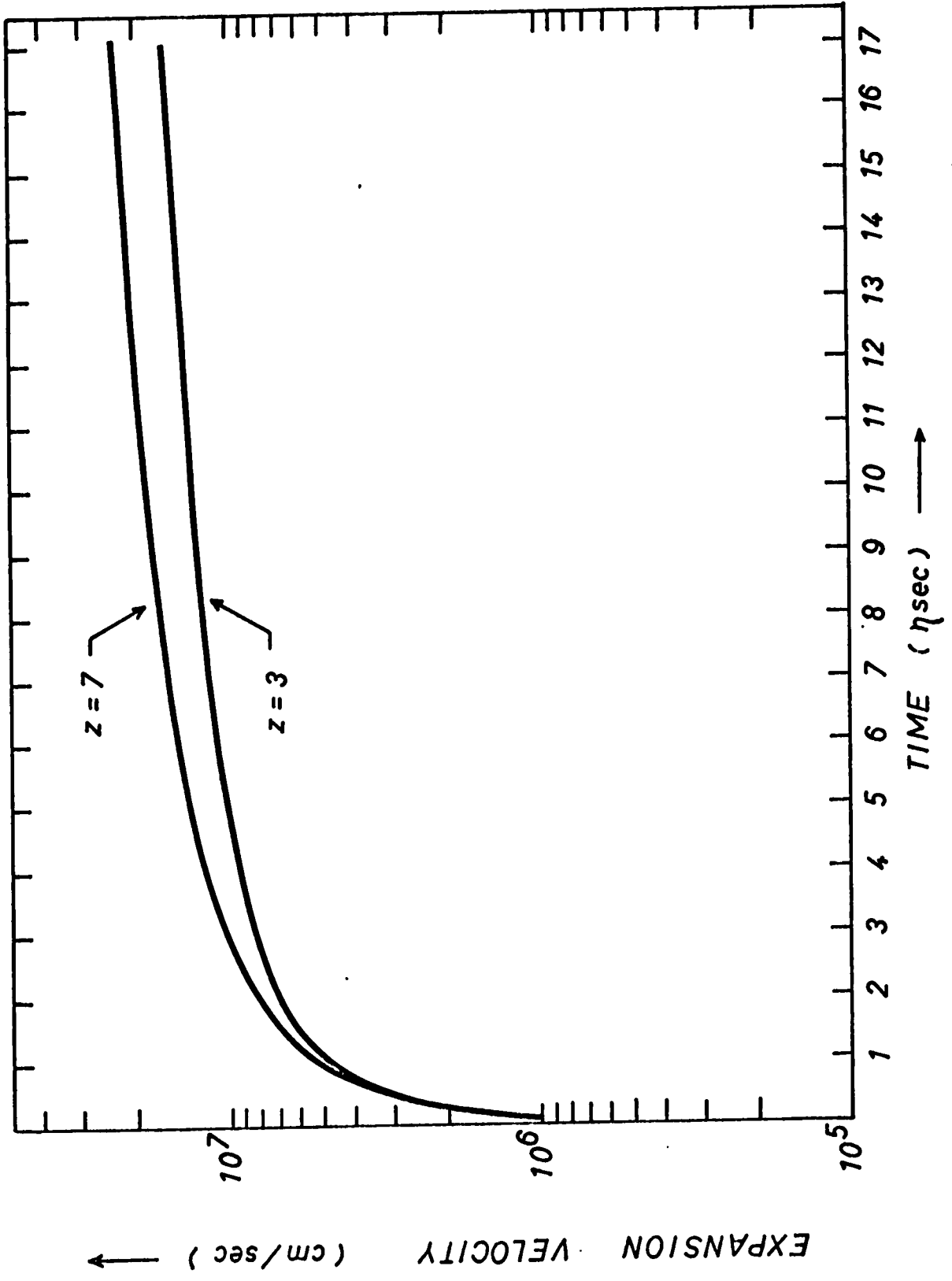


Fig. 3.8 Effect of Ion Charge Multiplicity on Expansion Velocity ($\alpha = 10$).

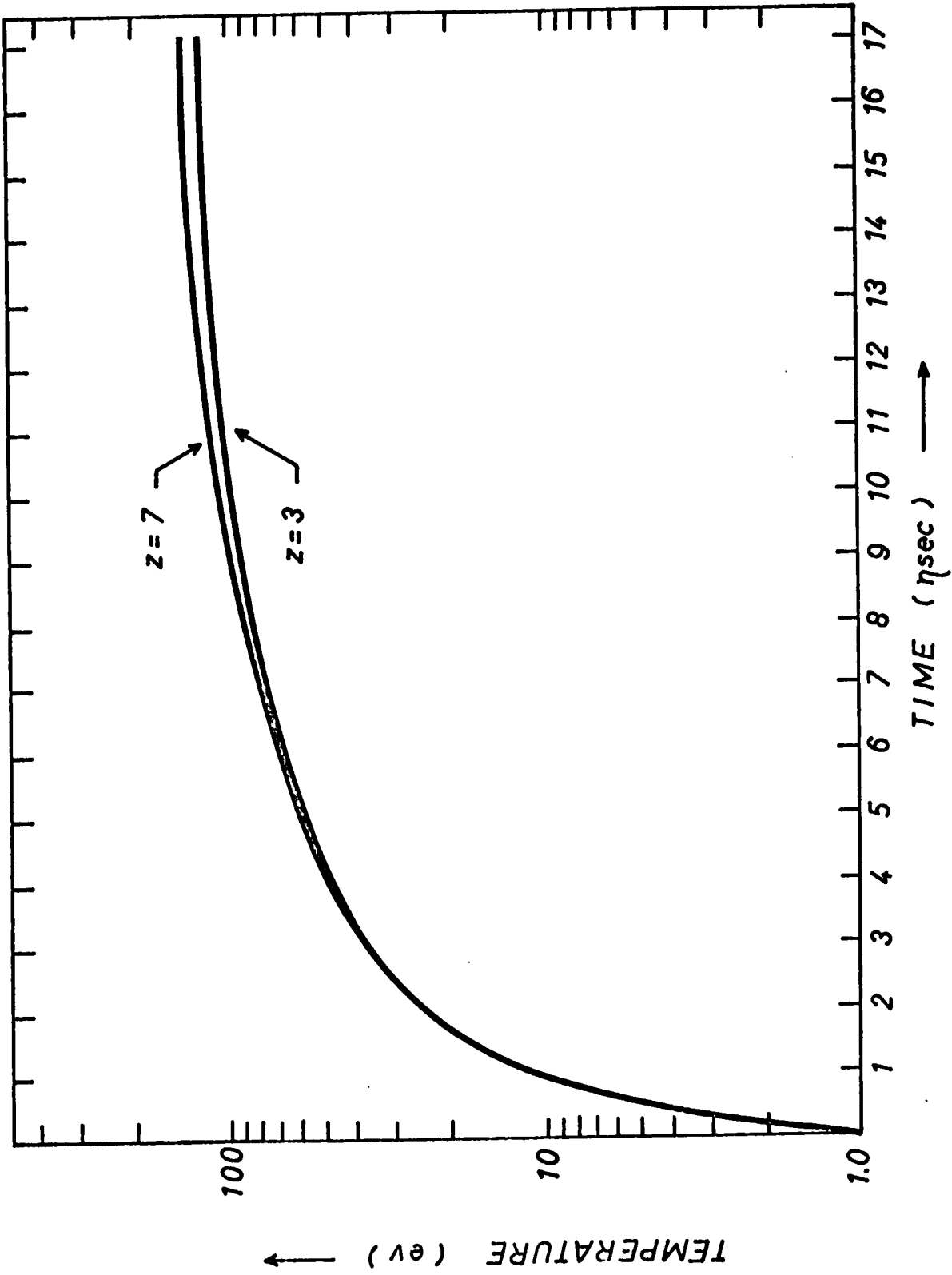


Fig. 3.9 Effect of Ion Charge Multiplicity on Plasma Temperature.

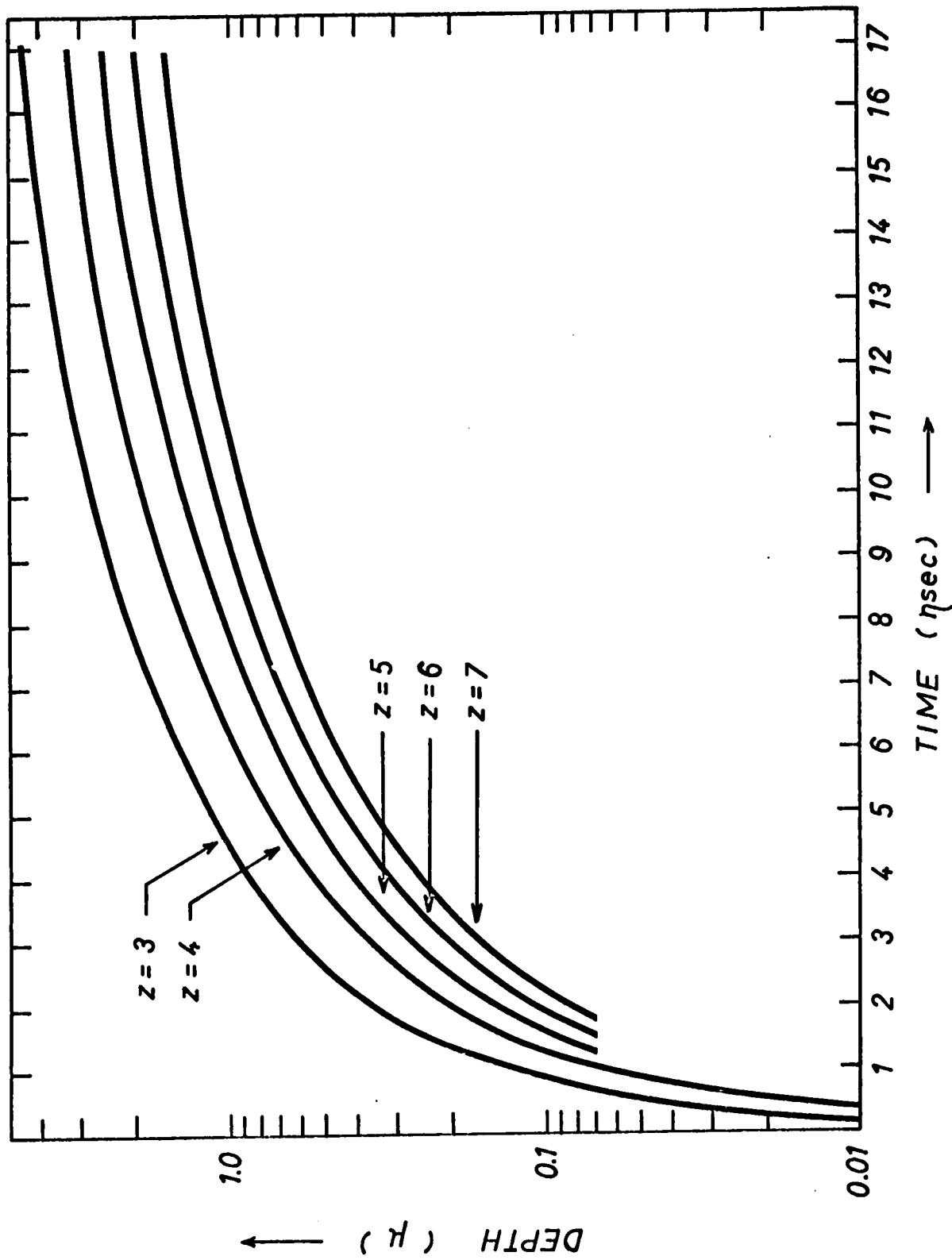


Fig. 3.10 Effect of Ion Charge Multiplicity on Depth of Target Fissure.

3.3 Discussion of Results and Comparison with Experiment

It can be seen by reference to Figures 3.3 and 3.7 that for the particular conditions of the measurements reported in Chapter 2 (focal spot diameter = 300μ), the one dimensional model breaks down about 4nsec into the laser pulse. One would expect a subsequent three dimensional plasma expansion with somewhat lower temperatures than predicted by the one dimensional theory and somewhat lower expansion velocities.

At the time when the expansion becomes three dimensional, the model predicts temperatures in the vicinity of 50ev and expansion velocities of about 1.1×10^7 cm/sec, relatively independently of α or z . It appears that the increase in the optical absorption coefficient with z (and hence reduction in the total number of ions plus electrons in the flare) is compensated for by the energy loss represented by the higher degree of ionization so that the only pronounced effect of increasing z is to decrease the depth of the target fissure (see Figure 3.10).

To a first approximation, a temperature of 50ev at an electron density of about 10^{21} cm^{-3} would be consistent on thermal equilibrium grounds with ionization levels of six or higher for aluminum.

Despite the expected breakdown of the model at a fairly early stage of the laser pulse, the predictions are in qualitative agreement with several of the experimental observations reported in Chapter 2. The observed expansion velocity of 1.4×10^7 cm/sec agrees quite well with the range of $1 - 2 \times 10^7$ cm/sec predicted by the theory. The measured temperature in the luminous flare of ~ 10 ev at the end of the laser pulse is , however, much lower than the ~ 50 ev predicted at the breakdown of the one dimensional model. This may be due in part to the subsequent three dimensional expan-

sion of the experimental plasma, and also the addition to the luminous flare of cold target material from shock heating and plasma erosion at the end of the laser pulse. The observations of O'power et al² indicate that although laser transmission was prevented by LiH foils thicker than 3μ , the plasma could penetrate foils as thick as 30μ during its lifetime. In the present case, the measured depth of the target fissure ($15 \pm 5\mu$) was very much greater than the $2 - 5\mu$ that might be expected on the basis of the one dimensional theory.

3.4 Discussion of the Model

The most serious simplifications in the foregoing analysis are: the assumption of temperature uniformity; the simplification of the energy balance to discount laser reflection, plasma re-radiation, and losses to the solid target; and the absence of a more sophisticated treatment of ionization processes. A brief discussion of these phenomena and their role in the blowoff process will be presented.

As discussed by Dawson¹⁰, the primary means for temperature equilization in such a plasma is electron heat conduction. The equation for thermal diffusion is,

$$C_v \frac{\partial T}{\partial t} = \eta \frac{\partial^2 T}{\partial r^2} , \quad \dots 3.17$$

where for a fully ionized plasma, the thermal conductivity,¹

$$\eta = \frac{5.85 \times 10^{12}}{z \ln \Lambda} T^{5/2} \frac{\text{ergs}}{\text{sec deg cm}} ,$$

and the specific heat,

$$C_v = 2(n_e + n_i) \times 10^{-16} \frac{\text{ergs}}{\text{cm}^3 \text{ deg}} .$$

Thus, the distance heat will diffuse in a time t is given by ($\ln \Lambda \approx 5$),

$$l = \left[\frac{n}{C_v} t \right]^{1/2} = \left[\frac{6 \times 10^{27}}{z(n_e + n_i)} T^{5/2} t \right]^{1/2} \quad (T \text{ in kev}) \dots 3.18$$

For $n_i + n_e = 10^{21} \text{ cm}^{-3}$, $T = 0.1 \text{ kev}$, $t = 10^{-9} \text{ sec}$,

$$l = 10^{-2} \text{ cm}.$$

Thus, up until several nanoseconds into the laser pulse, at least, electronic conduction should be sufficient to maintain a high degree of temperature uniformity. In a uniform density plasma, moreover, the nature of the inverse bremsstrahlung absorption coefficient is such as to regulate the temperature, that is, the absorption coefficient decreases with increasing temperature. Although a more detailed consideration of thermal gradients would be desirable, this could be done only with a much more elaborate numerical scheme. The model of Fader³⁷ for the laser heating of an isolated spherical plasma, for example, includes a vector heat flow and it is observed that the radial distribution of plasma temperature becomes uniform after a few nanoseconds of the solid particle irradiation.

The role of plasma re-radiation in laser-produced plasmas has also been discussed by Dawson¹⁰. He notes that the plasma will be transparent to most of its bremsstrahlung radiation and that the net energy loss per unit volume can be approximated by¹,

$$\epsilon = 4.86 \times 10^{-31} z n_e^2 T^{1/2} \text{ watt/cm}^3, \dots 3.19$$

where T is in kev.

For $n_e \approx 10^{21} \text{ cm}^{-3}$, $T \approx 0.1 \text{ keV}$, this is the order of $10^{10} \text{ watt/cm}^3$ and thus negligible compared to the laser flux ($10^{11} \text{ watt/cm}^2$).

The experimental work of Basov et al.³⁸ justifies the neglect of the reflected laser light in the energy balance of the blowoff process. The fraction of power reflected from an aluminum target was observed to be less than 10% at $10^{11} \text{ watt/cm}^2$.

The only significant energy loss to the solid target during the primary blowoff process will be the momentum given to the solid as a reaction to the plasma formation. As discussed by Caruso and Gratton¹³, the fraction of the laser energy dissipated in this shock wave will be of the order of $(\rho_2/\rho_0)^{1/2}$, where ρ_0 is the density of the undisturbed solid, and ρ_2 is the density of the plasma layer produced. This will be negligible for metallic targets at these power levels.

A complete treatment of plasma ionization processes would be a matter of some complexity for high z target elements such as aluminum. In addition to the numerical complication that such a treatment would entail, there is some question as to the applicability of the equilibrium theory, at least in the early stages of the process.

The effective time to raise the average degree of ionization by unity through electron impact is given approximately as³⁹,

$$\tau \approx \frac{1.4 \times 10^7 z^2}{n_e j} \left[\frac{E_H}{kT} \right]^{1/2} \frac{E_I}{E_H} \exp \left[\frac{E_I}{kT} \right] \text{ sec ,} \quad \dots 3.20$$

where E_I is the ionization potential, E_H , the ionization potential of hydrogen, and j is the number of equivalent electrons in the outer shell of the ion that are available for ionization. At an electron density of about 10^{21} cm^{-3} , and temperature of about 50 eV, this reduces to,

$$\tau \approx 5 \times 10^{-16} \frac{z^2}{j} E_I \exp \frac{E_I}{50} \text{ sec} , \quad . . . 3.21$$

where E_I is in ev. Thus, even for E_I in the range of 200ev, and z of the order of 5, the collisional ionization time would be very small (of the order of 10^{-10} sec).

Thus, one might expect the Saha equation to apply,

$$\frac{N_{z+1}}{N_z} \approx \frac{2 \times 10^{21}}{n_e} \theta^{3/2} \exp - \frac{E_I}{\theta} , \quad . . . 3.22$$

neglecting the differences in the partition functions of the relevant ions. Thus, for an electron density of $\sim 10^{21} \text{ cm}^{-3}$ and temperature of 50ev, one could expect aluminum ions of charge multiplicity six or greater. (The ground state ionization energy of Al^{6+} is about 250ev.)

Schwob et al³⁰, in vacuum ultraviolet spectroscopic work on the laser-blowoff aluminum plasma, have observed the simultaneous appearance of lines associated with $\text{Al}^{3+} - \text{Al}^{7+}$ near the time of maximum temperature. This is in apparent contradiction to the equilibrium statistics but may have been due to temperature gradients and the absence of spatial resolution in their experiment. For temperatures much less than 50ev, however, it can be seen from equation 3.21 that even on times scales of 20nsec or larger, non equilibrium ionization must be considered.

Several additional features should perhaps be emphasized in connection with the results of this highly simplified treatment of the blowoff process. It can be seen in reference to Figure 3.5 that approximately one-half of the available laser energy manifests itself as thermal energy. This result has previously been noted¹⁴ for the one dimensional expansion of a laser-heated, constant mass plasma slab. It is interesting to note that a three dimensional expansion reduces this fraction to one-quarter.

The results of a more sophisticated numerical treatment of a laser-

blowoff hydrogen plasma have recently appeared⁴⁰. These results for the constant power irradiation of a block of solid hydrogen are in qualitative agreement with those presented here. An important feature of these studies is the relatively shallow penetration of the laser into the solid target. This may have important consequences for the production of spherically symmetric plasmas by laser irradiation of isolated target specks. In particular, the very strong dependence of the depth on the ionic charge multiplicity is noteworthy. This implies that the laser irradiation of isolated high z target specks of dimensions greater than a few microns may be mainly a surface phenomenon.

CHAPTER 4 THE FORMATION AND EXPANSION OF BLOWOFF PLASMAS IN A LARGE
TRANSVERSE MAGNETIC FIELD

The interaction of laser-produced plasmas with magnetic fields has been of considerable interest in recent years. This has been directed at two possibilities. The first, is the creation of very high temperature plasmas with relatively long laser pulses ($>1\text{nsec}$) by inhibiting the expansion of the laser-produced plasma (normally the limiting factor for the plasma temperature) by means of the magnetic field. The second possibility is to use a relatively weak magnetic field to re-thermalize the laser produced plasma at some point in its expansion and create a hot, moderately dense plasma such as might be suitable for filling thermonuclear machines.

Creating a cavity of volume V in a magnetic field of strength B requires an amount of energy,

$$W = 3.98 \times 10^{-2} B^2 V \quad , \quad \dots 4.1$$

where B is in kgauss, V , in cm^3 , and W , in joules. Thus for a field of 10kgauss, a volume of 2.5cm^3 is required to absorb 1 joule of energy. To absorb 1 joule in the typical focal volume of a laser pulse (10^{-4}cm^3), a magnetic induction of several megagauss would be required.

Several theoretical studies on the dynamics of a high β , diamagnetic plasma blob expanding into a uniform magnetic field have been recently carried out^{15,16}. It is predicted that such an expanding plasma of infinite conductivity should repeatedly bounce off the compressed magnetic field at the point where $\beta \approx 1$. The effect of a finite resistivity is to superimpose on this motion a slow diffusion of the plasma across the field.

In the experiment described in this chapter, the interaction of laser-blowoff metal plasmas with transverse magnetic fields in the 100kgauss range was studied. These fields were generated by means of a line current through the target rod. Under these conditions, it was found that the classical diamagnetic behaviour discussed above^{15,16} was not observed and that the plasma crossed the field freely by means of an electrical polarization, at a constant velocity which was significantly lower than the zero field velocity. This velocity reduction has been attributed to an inhibiting effect of the magnetic field on the normal ambipolar energy transfer between electrons and ions in the free expansion of laser-blowoff plasmas.

4.1 The Experiment

For the purposes of this experiment a large current was passed through the target rod to generate a large transverse magnetic field during the blowoff plasma formation. This was obtained by discharging a $45\mu\text{F}$, 20kv capacitor bank several microseconds in advance of the laser pulse. A schematic diagram of the discharge path is shown in Figure 4.1.

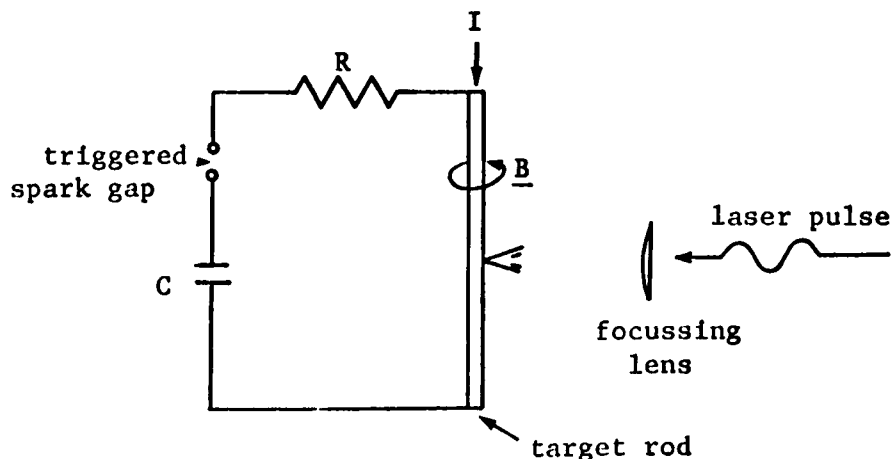


Fig. 4.1 The Discharge Circuit.

The capacitor bank was triggered by means of a co-axial spark gap and thyatron pulser. A 2 foot length of nichrome strip having a resistance of $.025\Omega$ was included in the capacitor bank leads to prevent the peak inverse current rating of the capacitors from being exceeded. The inductance of the discharge path was estimated from the period of the underdamped discharge to be 3.5×10^{-7} henry. The current waveform was monitored by means of a small coil placed near one of the capacitor bank leads, the output of which was integrated and displayed on a type 555 oscilloscope. The shape of the resulting waveform was found to be in good agreement with that expected for an underdamped RLC circuit with the parameters, $R = .025\Omega$, $L = 3.5 \times 10^{-7}$ henry, and $C = 45 \mu\text{F}$. The expected current for a circuit of these parameters was then used to calibrate the current monitor. The calculated current waveform is shown in Figure 4.2 for a charging voltage of 10kv. It can be seen that a charging voltage of 20kv could provide a current peak of about 200kamp with a half period of about $12.5\mu\text{sec}$.

The magnetic field generated by a line current I is given by,

$$B(r) = \frac{2.00 I \times 10^2}{r} \quad \text{gauss} , \quad \dots 4.2$$

where I is in kamp and r is in cm. Thus, at the surface of a 3.12mm radius rod, the magnetic field is given by,

$$B_o = 0.639 I \quad \text{kgauss}.$$

The laser pulse was synchronized by means of a Pockels cell to occur at one of the peaks in the current waveform, so that the magnetic field was held constant within a few percent over the maximum time interval of interest (less than $0.5\mu\text{sec}$). A block diagram of the electronics is shown in Figure 4.3.

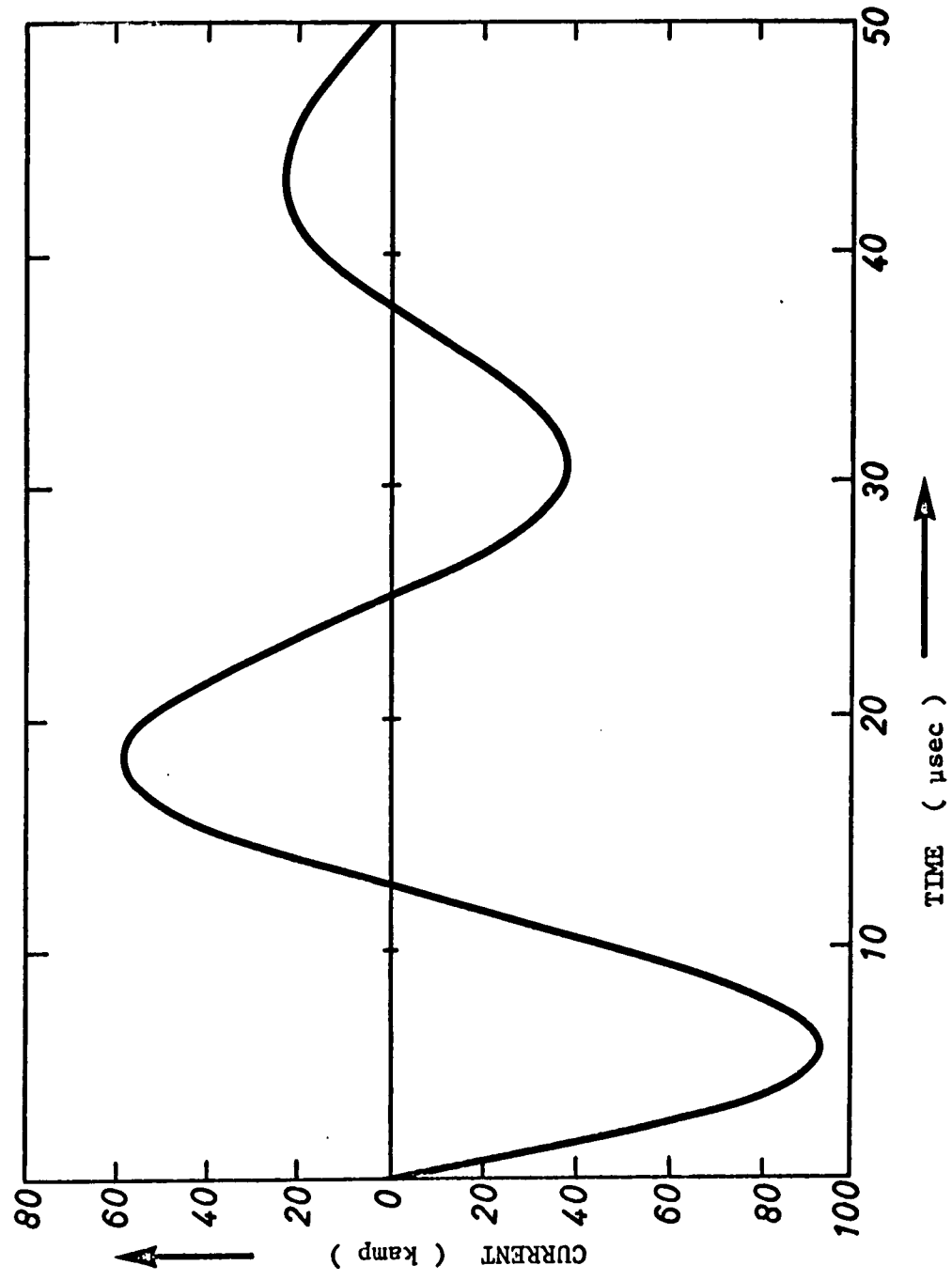


Fig. 4.2 Underdamped RLC Current Waveform for 10kv Charging Voltage.

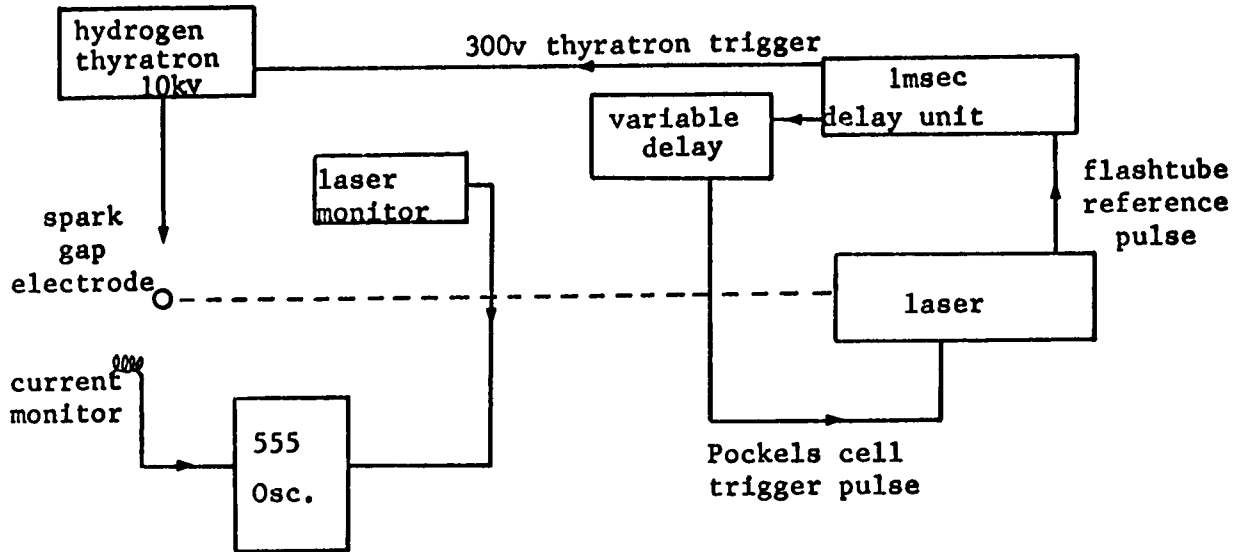


Fig. 4.3 Capacitor Bank Trigger Arrangement.

The properties of the plasma formed in this high gradient magnetic field were studied by means of high speed photography, charge collection probes, a movable diamagnetic probe, a movable transverse electric field probe, and the emission-absorption technique described in Chapter 2. The target chamber was evacuated to 10^{-5} torr before each shot and the target was rotated every five shots to expose a fresh surface.

4.2 High Speed Photography

The setup used to observe the luminous flare at the target surface in this case was identical to that described in Section 2.3 of Chapter 2. 50 nsec frames of the flare development in fields of $B_0 = 0 - 70$ kgauss (B_0

denotes the field strength at the target surface) are shown in Figure 4.4, with the camera aligned parallel (side view), and perpendicular (view from above) to the magnetic field. The first frame (0 - 50 η sec) was triggered a few nanoseconds before the arrival of the laser pulse at the target surface. These photographs were obtained with a camera f stop of 25.

It can be seen (Fig. 4.4a) that the luminous flare remains roughly spherically symmetric for at least 50 η sec after the start of the laser pulse but develops a "wedge" shape away from the target surface before the 225 η sec frame. The thickness of the plasma stream (or angle of the wedge) decreases with increasing magnetic field.

Due to the experimental geometry, the flare could be viewed from above (Fig. 4.4b) only after it had expanded past about 1mm from the target surface, thus, the first frame (0 - 50 η sec) was not available from this position. It can be seen, however, that there is some evidence of plasma "trapping" or spreading out along the field lines a few mm from the target surface, at B_0 greater than 40kgauss in the 225 η sec frame.

200 η sec streak photographs of the event in the plane parallel to \underline{B} are shown in Figure 4.5 for B_0 in the range of 0 - 110 kgauss. These were obtained with a camera f stop of 8.0. It can be seen that for B_0 in the range of 0 - 40 kgauss, the expansion does not proceed uniformly and that a secondary feature develops about 150 η sec after the start of the laser pulse. This feature has been confirmed to coincide with the development of the wedge shape discussed above in connection with the framing camera photographs. At fields above 70 kgauss, it can be seen that the flare increases in luminosity and exhibits a sharp boundary which expands uniformly over this time interval at a velocity of about 7×10^6 cm/sec.

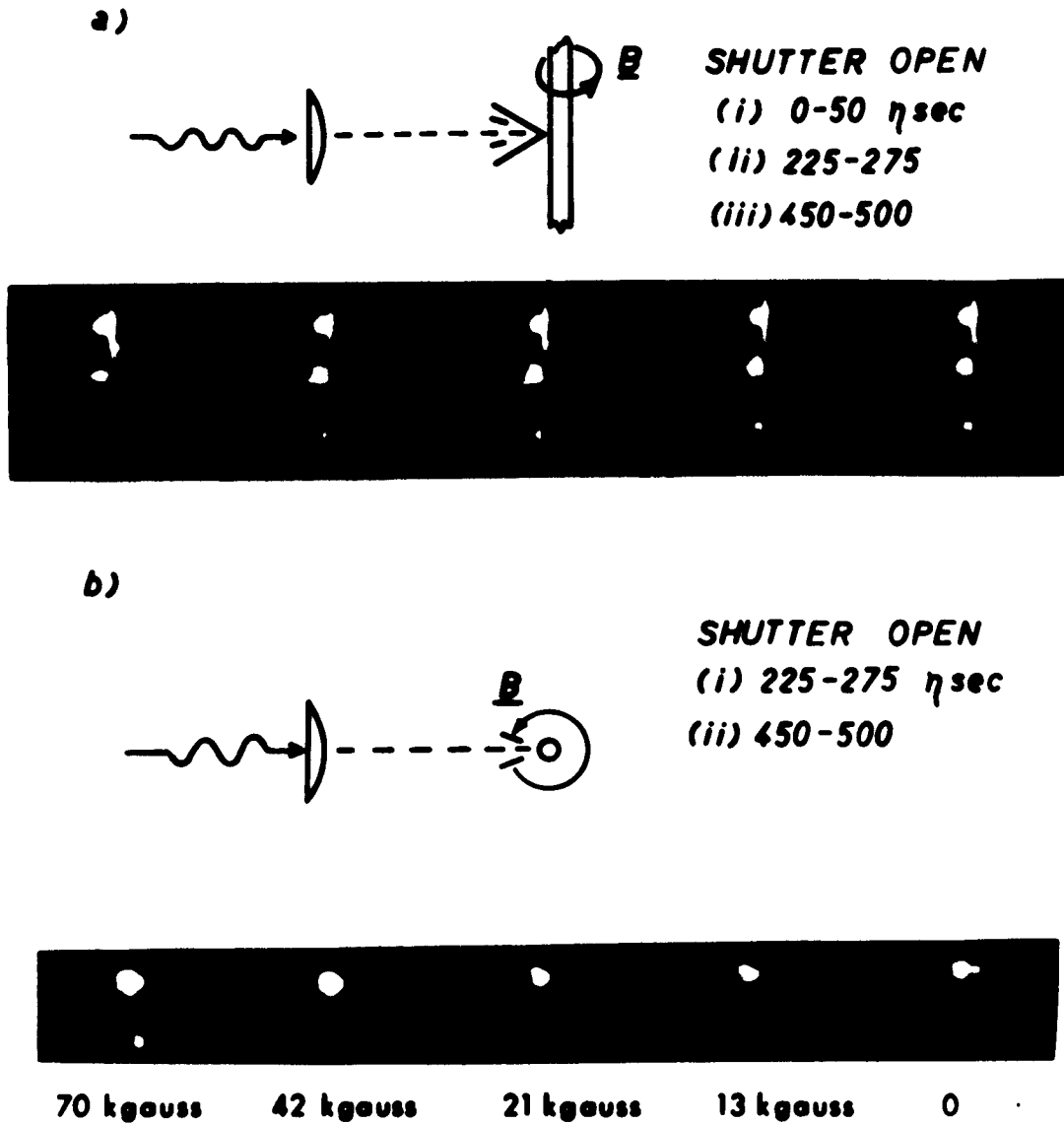


FIG. 4.4 50 NANOSECOND FRAMES OF FLARE DEVELOPMENT IN A MAGNETIC FIELD

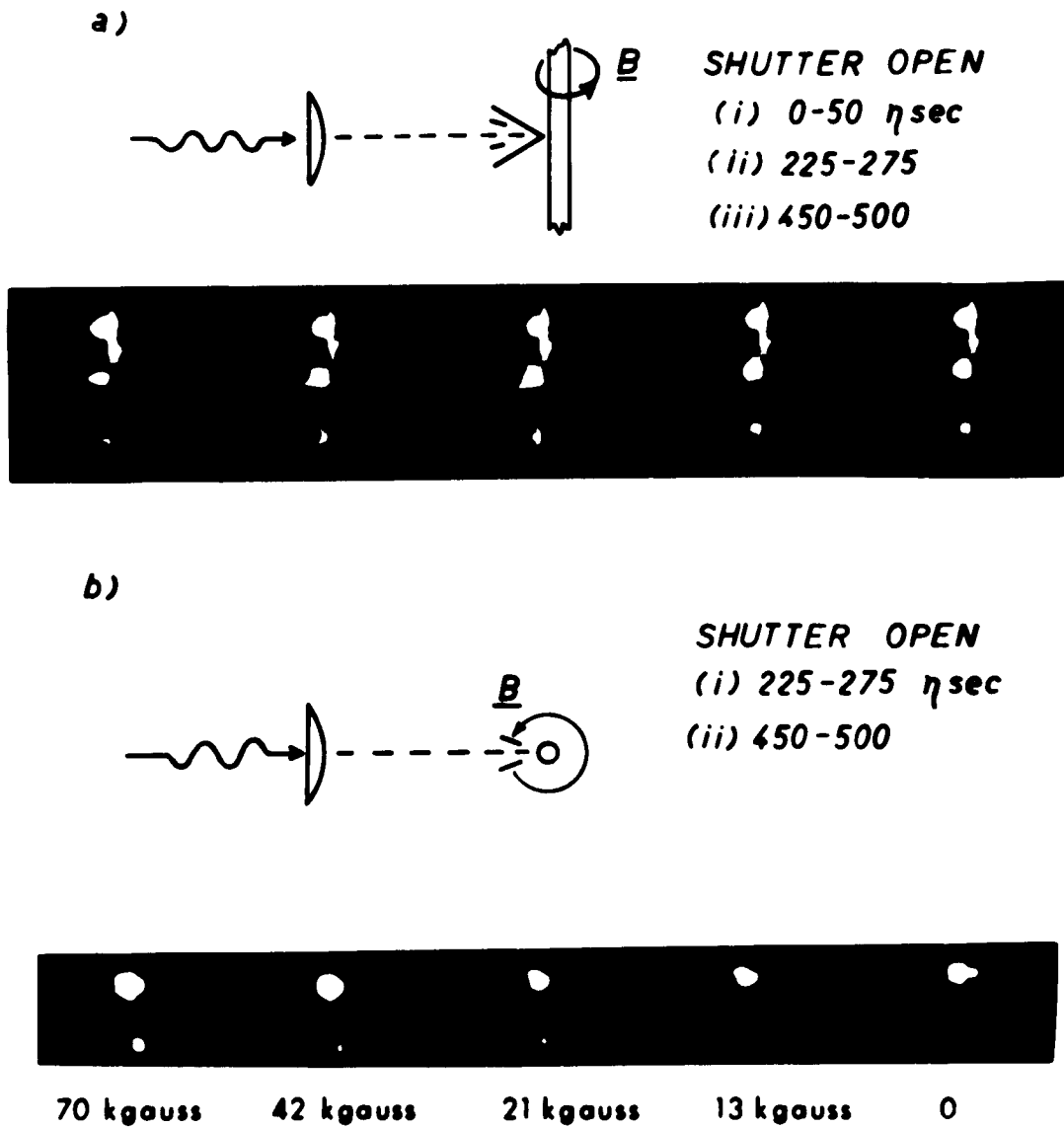


FIG. 4.4 50 NANOSECOND FRAMES OF FLARE DEVELOPMENT IN A MAGNETIC FIELD

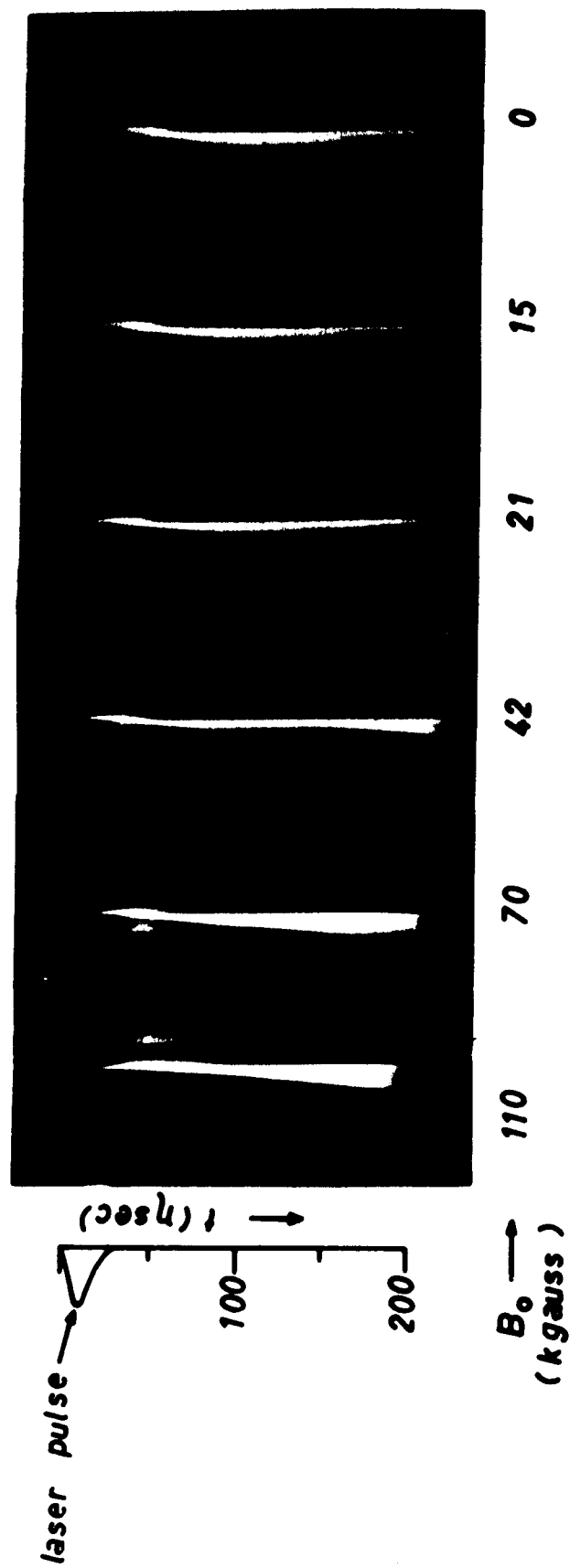


FIG. 4.5 200 NANOSECOND STREAK PHOTOGRAPHS OF FLARE DEVELOPMENT IN A MAGNETIC FIELD

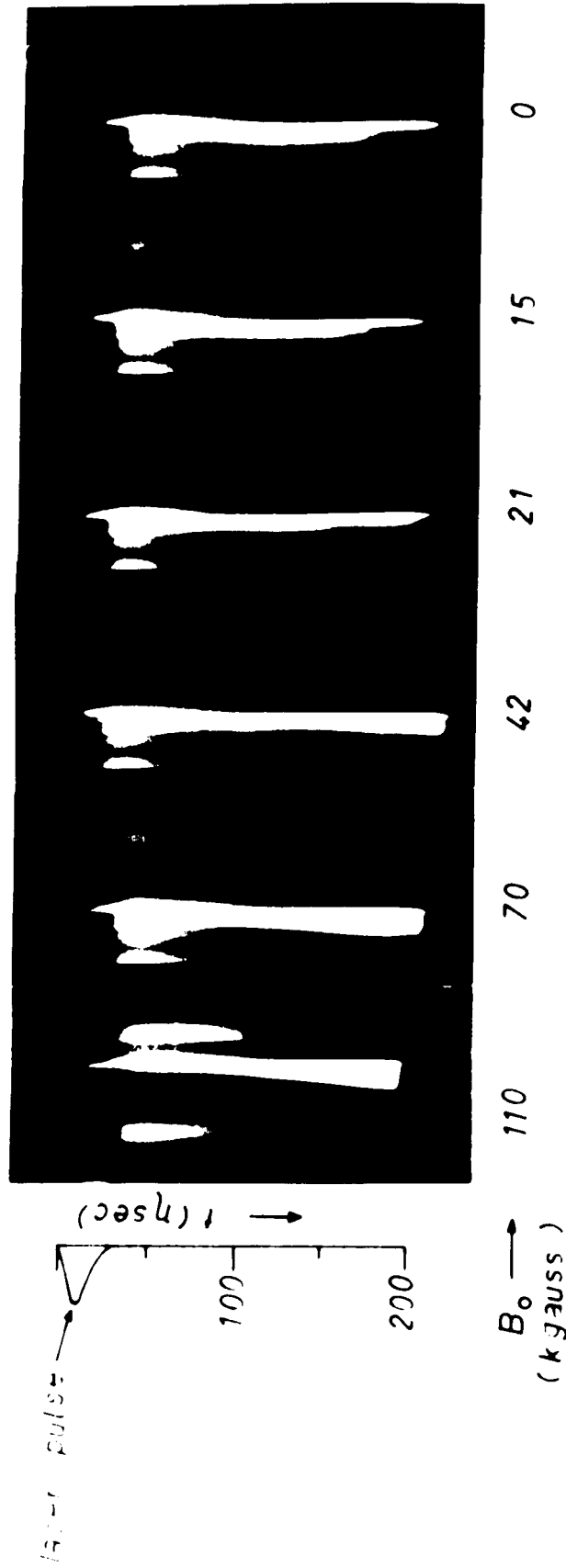
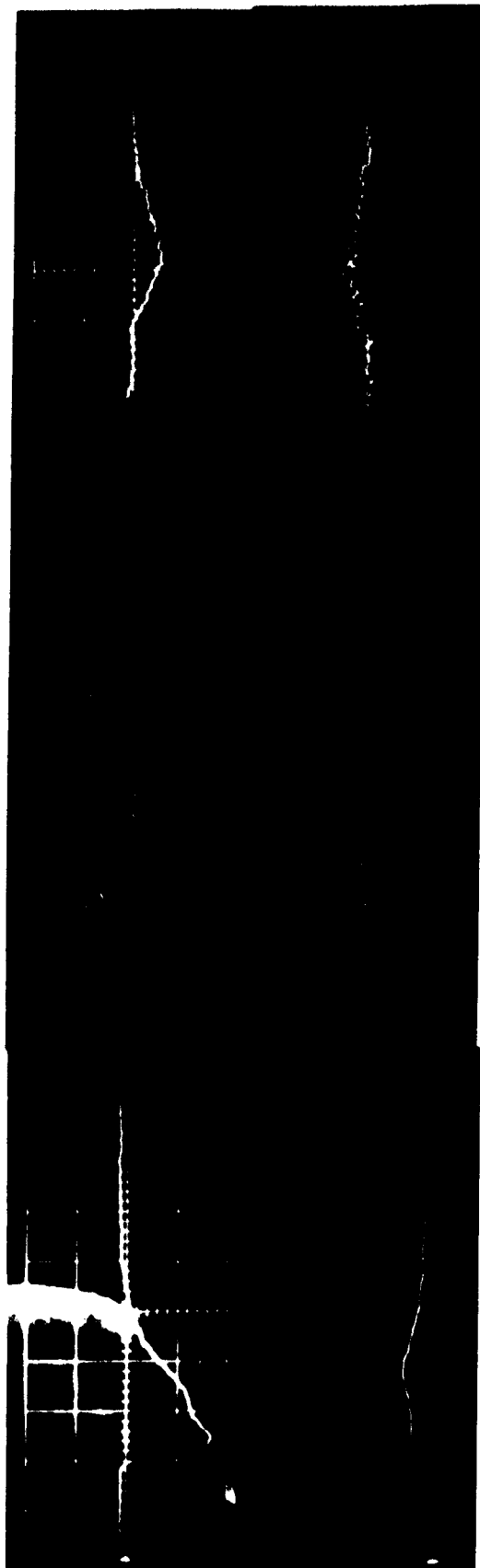


FIG. 4.5 200 NANOSECOND STREAK PHOTOGRAPHS OF FLARE DEVELOPMENT IN A MAGNETIC FIELD

4.3 Emission-Absorption Studies

Using the same experimental setup described in Section 2.4 of Chapter 2, the plasma emission and absorption at 6328 \AA was studied in the presence of the magnetic field. These measurements were performed with a target current of 110 kAmp, corresponding to $B_0 = 70$ kgauss. Emission and absorption profiles recorded at 0.5, 1.0, and 1.5mm from the target surface are shown in Figure 4.6.

The most interesting feature of these results is the development of a strong secondary maximum in the emission and absorption signals recorded at 1.0 and 1.5mm from the target surface in the magnetic field (compare to Figure 2.8). This secondary feature occurs about 150 nsec after the start of the laser pulse. The profiles at 1.0mm are analyzed in terms of ion density and radiation temperature in Figure 4.7. To obtain the density estimate, it was again assumed that the plasma thickness was constant at 1mm. This assumption is somewhat questionable in this case in view of the framing photographs of the flare development in a field of 70 kgauss, but in any event, the maximum at $\sim 150 \text{ nsec}$ in the density curve of Figure 4.7 represents an increase in the total amount of plasma in the midplane of the system over the zero field case, at this stage of the flare development. A comparison of Figures 2.10 and 4.7 indicates that the radiation temperature in the flare is not much effected by a magnetic field of this magnitude.



R = 0.5 mm

R = 1.0 mm

R = 1.5 mm

EMISSION - UPPER TRACE
 P.M. = 1400v
 50 ηsec/div
 0.1 v/div (neutral density = 0.5)

P.M. = 1600v
 50 ηsec/div
 .05 v/div

P.M. = 1600v
 50 ηsec/div
 .05 v/div

ABSORPTION-LOWER TRACE
 P.M. = 1000v
 .05v/div (dc level = .08v)

P.M. = 1000v
 .01 v/div (.08v)

P.M. = 1000v
 .005v/div (.08v)

FIG. 4.6 EMISSION - ABSORPTION PROFILES WITH $B_0 = 70$ KGAUSS



TOP TRACE

R = 1.0 mm

R = 1.5 mm

P.M. = 1400V
50 nsec/div
0.1 V/div (neutral density = 0.5)
P.M. = 1000V
0.5 V/div (dc level = .08V)

P.M. = 1400V
50 nsec/div
0.05 V/div
P.M. = 1000V
0.1 V/div (.08V)

P.M. = 1400V
50 nsec/div
0.5 V/div
P.M. = 1000V
0.05 V/div (.08V)

FIG. 40. NEUTRON CAPTURE RESONANCE ABSORPTION PROFILES WITH $B_0 = 70$ KGAUSS

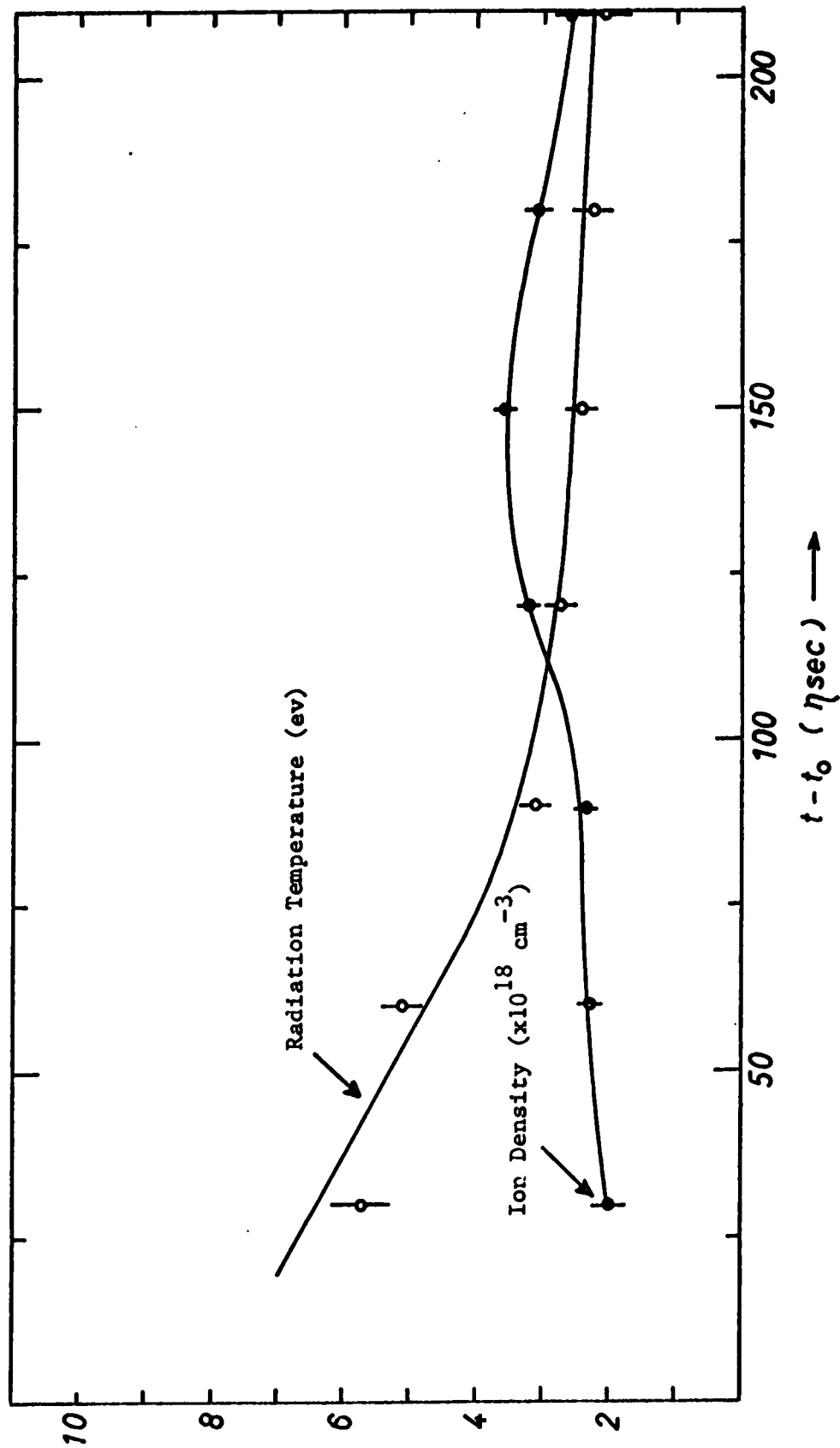


Fig. 4.7 Flare Temperature and Density 1.0mm from Target Surface with $B_0 = 70$ kgauss.

4.5 Probe Measurements

In the later stages of the plasma decay ($R > 1.5\text{cm}$), the plasma was studied with movable diamagnetic, charge collection, and electric field probes. These were inserted into the vacuum system through the probe port shown in Figure 1.6 and the probe axis was at an angle of 20° to the incident laser pulse as shown in Figure 4.8.

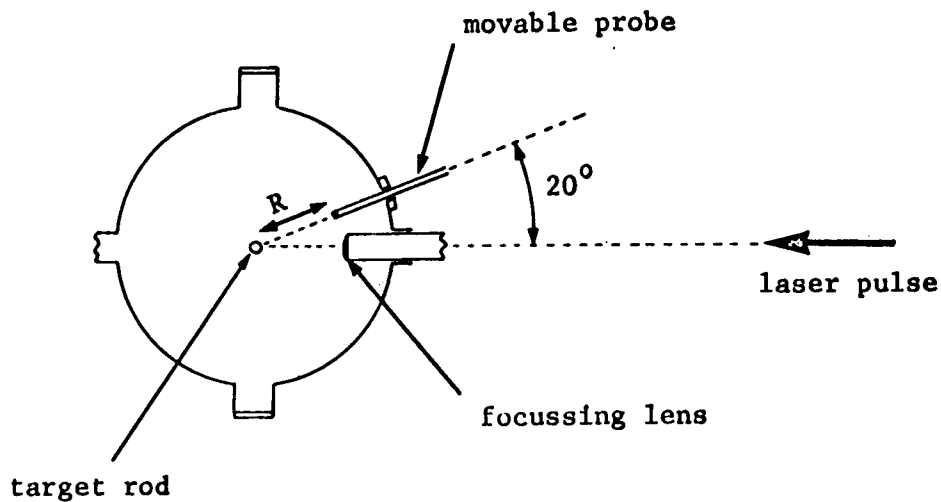
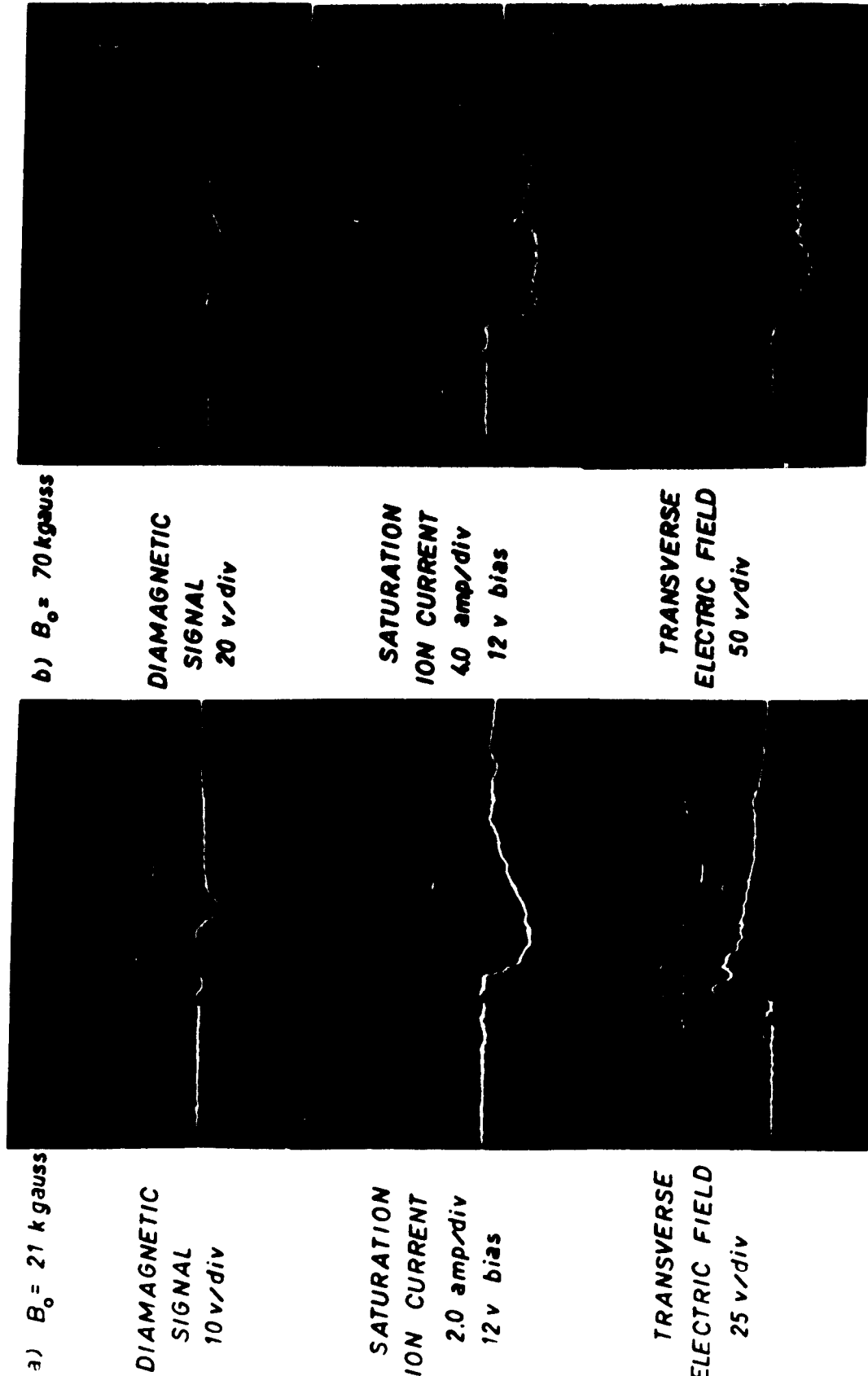


Fig. 4.8 Probe Insertion Geometry.

The probe signals were displayed on one beam of a Textronix, type 555 oscilloscope together with the output of the laser monitoring photodiode through a type 1A4 plug in. The output of the target current monitor was displayed on the second beam with a brightened portion corresponding to the laser discharge.

The diamagnetic probe consisted of 10 turns wound in a coil of 1.5mm length and 0.5mm radius, with a measured inductance of 1μhenry and resistance of 10Ω . The coil was enclosed in a 5mm diameter glass sheath and

Representative movable probe signals are reproduced in Figure 4.10 at $R = 1.5\text{cm}$ (probes 1.5cm from target surface), for $B_0 = 70$ kgauss and $B_0 = 21$ kgauss. It can be seen that all three signals define a sharp plasma boundary propagating across the field at a high velocity. This velocity was observed to be independent of R even though B falls off as $1/R$. The velocity of the ionization front as a function of B_0 , for an aluminum target, is shown in Figure 4.11.



a) $B_0 = 21 \text{ kgauss}$

DIAMAGNETIC
SIGNAL
10 v/div

SATURATION
ION CURRENT
2.0 amp/div
12 v bias

TRANSVERSE
ELECTRIC FIELD
25 v/div

b) $B_0 = 70 \text{ kgauss}$

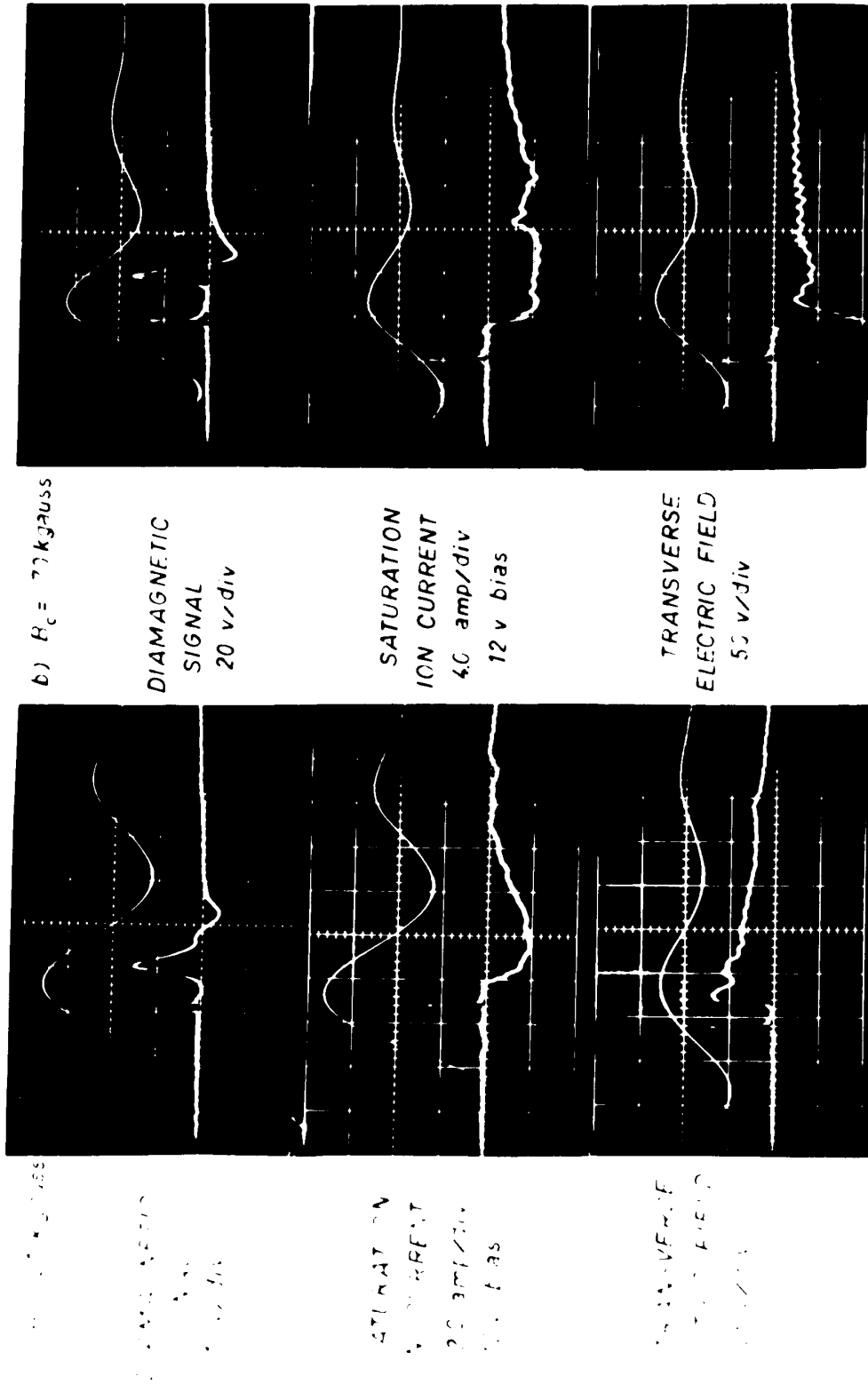
DIAMAGNETIC
SIGNAL
20 v/div

SATURATION
ION CURRENT
4.0 amp/div
12 v bias

TRANSVERSE
ELECTRIC FIELD
50 v/div

200 $\eta\text{sec/div}$ \rightarrow

FIG. 4.10 MOVABLE PROBE SIGNALS AT $R = 1.5 \text{ CM}$



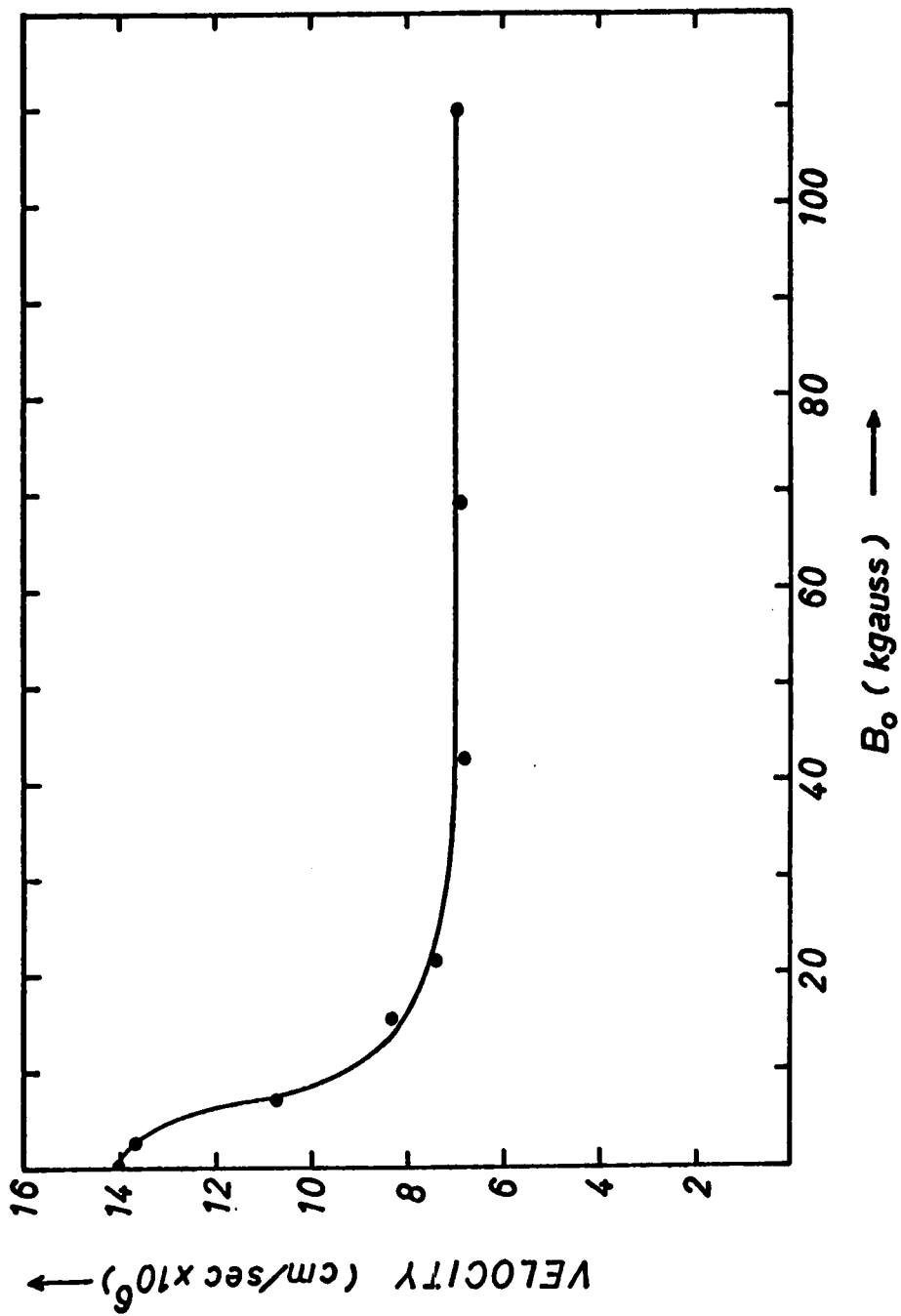


Fig. 4.11 Expansion Velocity of the Sharp Ionization Front of an Aluminum Plasma in a Magnetic Field.

The observed degree of diamagnetism and the magnitude of the transverse electric field at the plasma front are consistent with the hypothesis that the plasma crosses the magnetic field by means of an electrical polarization and $\underline{E} \times \underline{B}$ drift. A discussion of this mechanism and its relation to the experimental results follows.

4.5 A Discussion of the Cross-Field Plasma Flow

The injection of a plasma stream into a transverse magnetic field is a matter of considerable experimental and theoretical interest. This centres for the most part on the possibility of cross-field injection of plasmas from guns or other devices into various confinement geometries. There are essentially two mechanisms by which such flow may occur:

- (i) Diamagnetic Flow. In this case the plasma is considered to remain completely diamagnetic as it enters the field and has sufficient momentum to "push" the field lines aside.

It follows that a necessary requirement for this mechanism to function is that⁴¹,

$$\frac{1}{2} n_i m_i v_d^2 > \frac{B^2}{2 \mu_0}, \quad \dots 4.3$$

where v_d is the plasma drift velocity perpendicular to the magnetic field, B .

- (ii) Electrical Polarization and $\underline{E} \times \underline{B}$ Drift. In this case the plasma does not completely exclude the induction but is dense enough to electrically polarize and cross the field by means of an $\underline{E} \times \underline{B}$ drift.

The maximum polarization field obtainable in a given plasma is limited by its density. That is, the maximum particle displacement is of the order of the electron or ion Larmor radius. A displacement of all ions relative to the electrons by an amount b (the ion gyroradius) produces an electric field,

$$E_p = \frac{z b n_e e}{\epsilon_0} , \quad \dots 4.4$$

where n_e is the plasma density and z , the ion charge multiplicity. Then from the requirement that $\underline{E}_p + \underline{v}_d \times \underline{B} = 0$, it follows that the limiting flux density that the plasma can cross in this manner is given by,

$$B_{mi} = \left[\frac{m_i n_e}{\epsilon_0} \right]^{1/2} . \quad \dots 4.5$$

The electrons because of their faster response may, in some circumstances, be responsible for the initial polarization as a plasma stream first enters the field. From the same argument, the limiting flux density in this case ($b =$ electron gyroradius) is given by,

$$B_{me} = \left[\frac{m_e n_e}{\epsilon_0} \right]^{1/2} . \quad \dots 4.6$$

It can be seen that the limits imposed by equations 4.5 and 4.6 are not very serious in most practical cases. That is, for aluminum, we have $B_{mi} = 2.3 (n_e)^{1/2}$ gauss, and $B_{me} = 3 \times 10^{-3} (n_e)^{1/2}$ gauss, where n_e is in cm^{-3} .

Because of the velocity distribution in the stream, a polarized plasma will also exhibit some diamagnetism. That is, ions moving faster or slower than v_d are deflected in the $-E_p$ or $+E_p$ directions respectively. In the moving frame these execute circular orbits and possess diamagnetic moments. By integrating over all particles, it can be shown that⁴²,

$$\Delta B = \frac{\mu_0 n_e k}{B} (T_i + T_e) , \quad \dots 4.7$$

where the T's are perpendicular temperatures in the moving frame.

The measured magnitude of the transverse electric field at the plasma front, 1.5cm from the aluminum target is shown in Figure 4.12, as a function of B_0 . It can be seen that E/B well matches the observed expansion velocity (dotted curve in Fig. 4.14). Thus an electrical polarization of the plasma accounts for its rapid motion across the magnetic field.

As might be expected on the basis of the above result, a graphical integration of the diamagnetic signal indicated that the plasma was well permeated by the applied field at this distance from the target surface. The measured values of $\Delta B/B$ (B being the local strength of the field at $R = 1.5\text{cm}$) are shown in Figure 4.13 as a function of B . It can be seen that $\Delta B/B$ lies in the range of 0.5 - 0.05, for B in the range of 0.5 - 20 kgauss (B_0 in the range of 2.8 - 110 kgauss). For the lower values of B (less than $\sim 1000\text{gauss}$), assuming temperatures of the order of 10eV and a density of the order of 10^{15} cm^{-3} , ΔB compares reasonably well with the predictions of equation 4.7. At higher values of B , however, the measured ΔB is significantly higher than expected. Moreover, the measured $\Delta B/B$ is approximately proportional to $B^{-2/3}$ instead of B^{-2} which would be expected on the basis of equation 4.7. This seems to indicate some strong interaction of the plasma stream with the applied field. A possible source of this interaction will be discussed in Section 4.6.

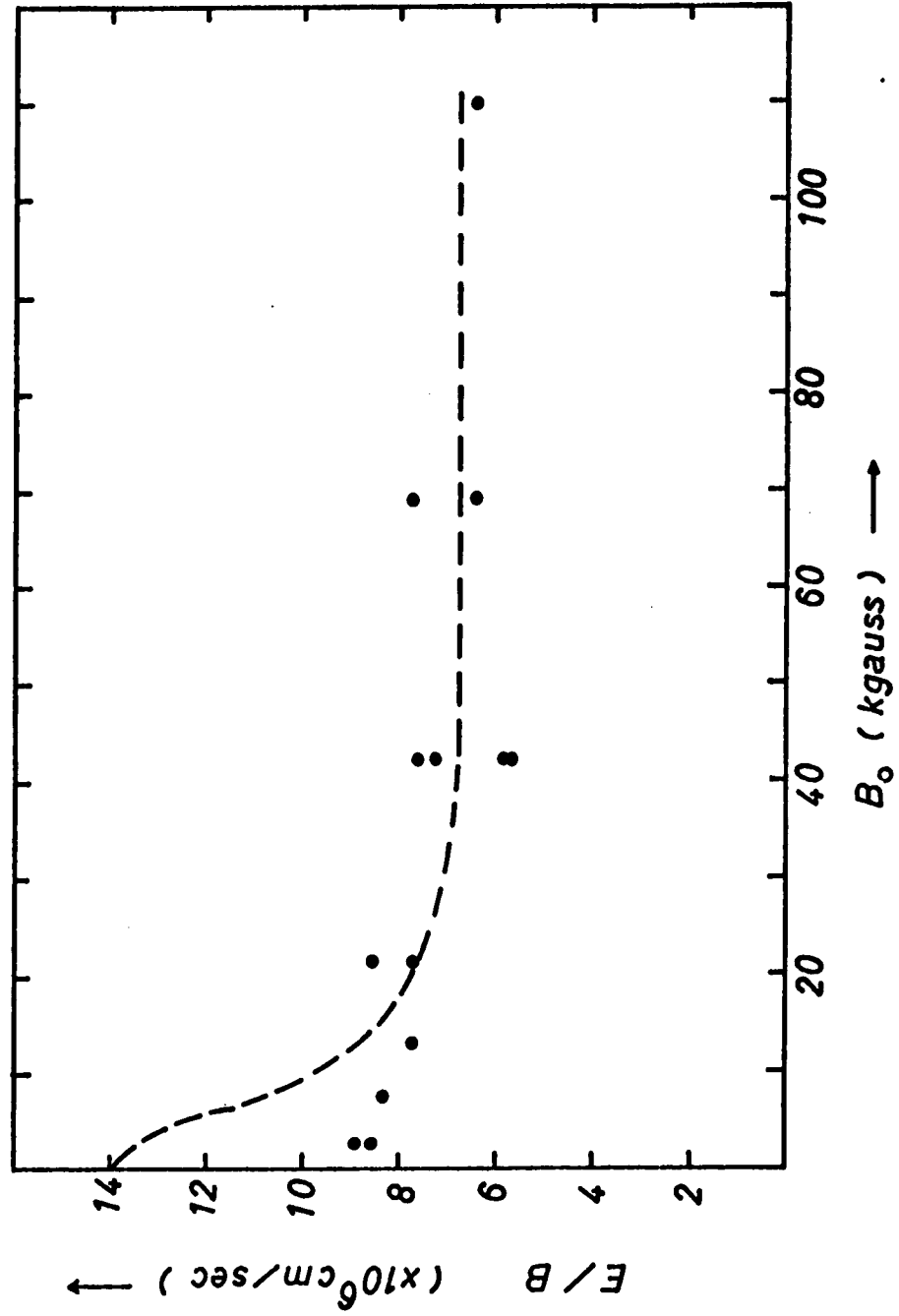


Fig. 4.12 Magnitude of Transverse Electric Field at the Ionization Front.

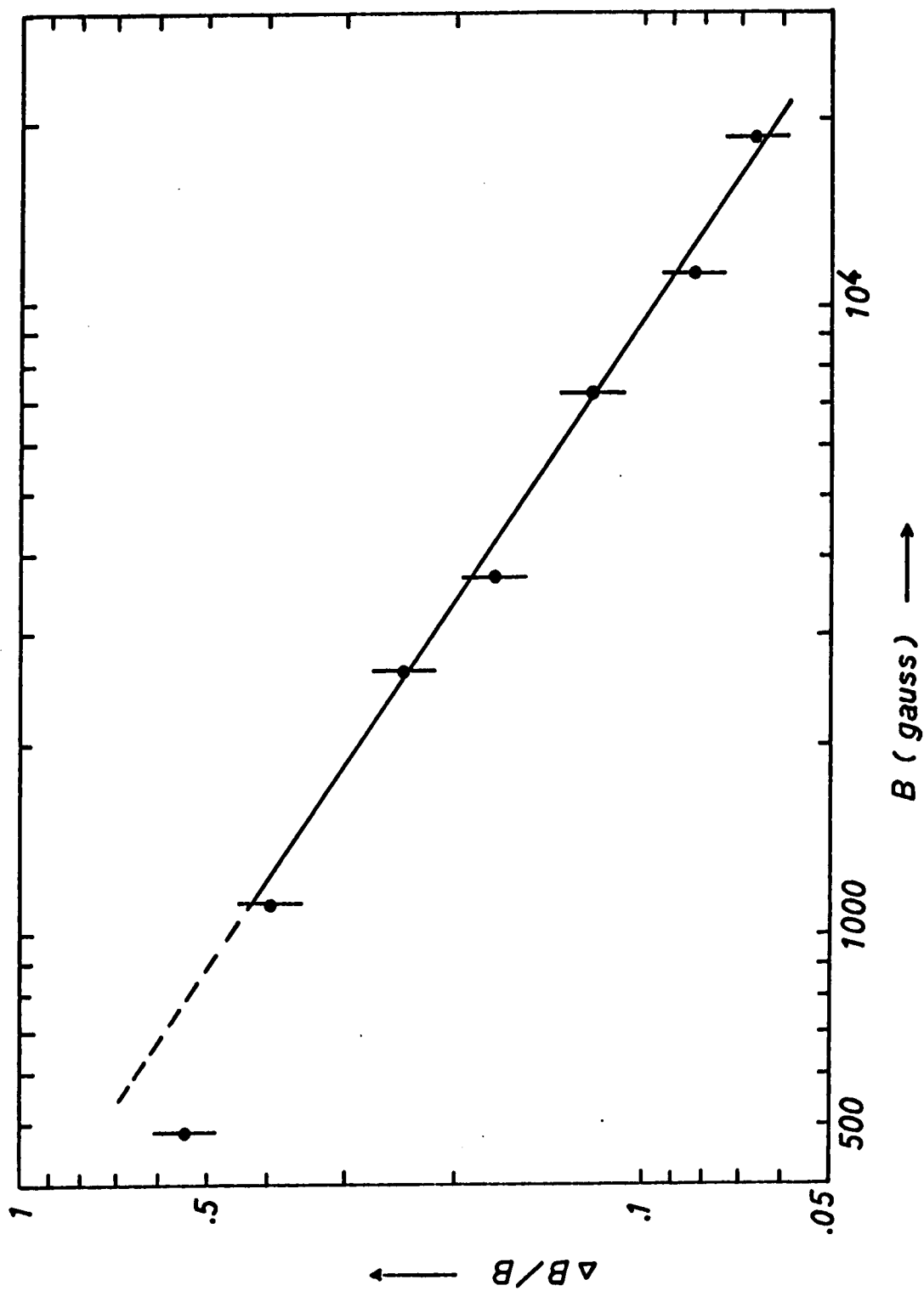


Fig. 4.13 Maximum Plasma Diamagnetism 1.5cm from the Surface of an Aluminum Target.

The increasing plasma confinement to the midplane of the system, mentioned above in connection with the framing camera photographs of the luminous flare, is confirmed in the magnitude of the saturation ion current to the double electrostatic probe. The magnitude of the probe current at $R = 1.5\text{cm}$, at the time corresponding to the peak diamagnetic signal (this was also the maximum ion current - see Fig. 4.10) is shown in Figure 4.14 for $B_0 = 0, 21, \text{ and } 70 \text{ kgauss}$. It can be seen that at biases of greater than 12v , the probe current increases by about a factor of four in a field, $B_0 = 70 \text{ kgauss}$ (the local field at $R = 1.5\text{cm}$ being 11.3 kgauss).

Although the application of the simple probe theory in fields of this magnitude is somewhat questionable, if the formulae of Section 2.6 are applied assuming the aluminum ions to be triply ionized, these currents would correspond to ion densities of about 5×10^{14} , 8×10^{14} , and $1.7 \times 10^{15} \text{ cm}^{-3}$, at $B_0 = 0, 21, \text{ and } 70 \text{ kgauss}$ respectively. In view of the fact that at $B_0 = 70 \text{ kgauss}$ ($B_{1.5} = 11.8 \text{ kgauss}$), the Larmor radius of a 5ev aluminum ion becomes comparable to the probe radius (the order of 10^{-2}cm), the ion saturation current in this case must be considered as yielding a lower limit on the ion density.

It is interesting to note that an inverse proportionality of stream thickness to B has been noted in the polarized injection experiments of Baker and Hammel⁴³. They explain the observation that $hB \approx \text{const.}$ ($h = \text{stream thickness}$) by means of a model that assumes each fluid element of the plasma enters the field and intermixes with a fixed value of the fringing field (independently of the applied field) and then moves across the remaining field while remaining pressureless and flux conserving.

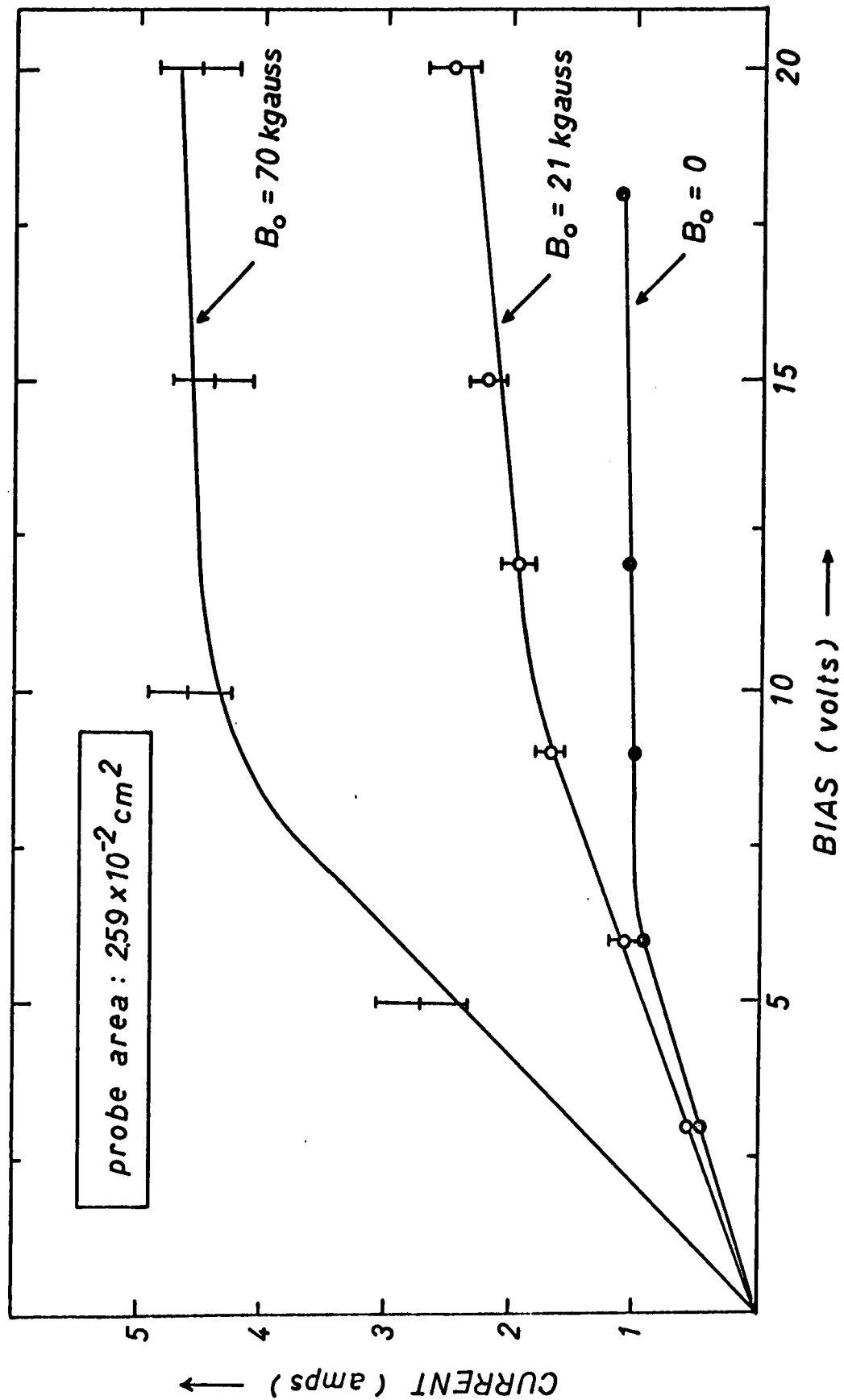


Fig. 4.14 Maximum Ion Current to the Double Probe, 1.5cm from the Target Surface.

4.7 The Source of the Plasma Velocity Reduction

The model developed in Chapter 3 of this thesis for the free expansion of a blowoff plasma describes the event through a single fluid equation of motion. Implicit in this model is an energy transfer from the plasma electrons to the ions (that is, it is assumed that both species expand at the same rate). It is thought that in fact this energy transfer is accomplished through a collective electrostatic interaction^{29,44}. The nature of this interaction can be understood by considering the expansion of a semi-infinite plane plasma slab which is initially at rest, in thermal equilibrium, and possesses complete charge neutrality. At the initial instant, during a time of the order $\tau \approx D/(m_e/2kT)^{1/2}$, the electrons will separate from the ions, a distance D , the Debye length, as shown in Figure 4.15.

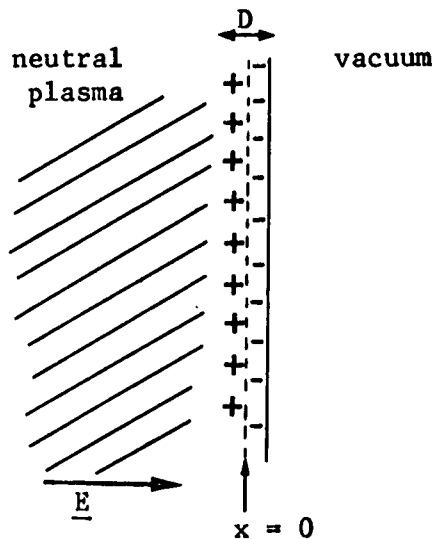


Fig. 4.15 Charge Separation in a Free Plasma Expansion.

At the plasma boundary there will be formed a double charge layer of thickness D . An electric field will result in the bulk of the plasma which will retard the escape of electrons and provide for a neutral expansion of the plasma through a process which may be described as an ambipolar acceleration of ions by electrons. This collective energy transfer is similar to the acceleration of a heavy piston (ions) by a light gas (electrons). It is clear that asymptotically a complete energy transfer to the ions will occur and the average ion energy will approach the value,

$$\bar{E}_i \text{ asymp.} \approx (z+1) kT_0 \quad \dots 4.8$$

Opower and Press²⁹ have developed a simple model of the collective energy transfer in the expansion of a spherically symmetric plasma, using a spherical condenser analogy (see Appendix B). They conclude that in a spherical plasma of initial radius, 0.1mm, the ions will gain 90% of their asymptotic energy after an expansion to 1.0mm.

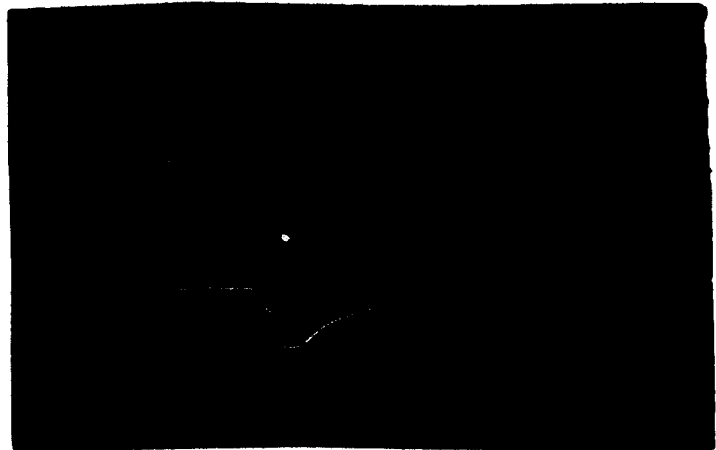
It must be emphasized that the process discussed above is a collective one and that in very dense plasmas such as the initial stage of the laser-blowoff expansion, electron-ion collisions may provide a further mechanism for an energy transfer between the ions and electrons which may very much complicate the situation.

In the presence of a sufficiently strong magnetic field, it is clear that the collective energy transfer will be inhibited due to the difference in electron and ion Larmor radius. Under these conditions, one would expect the electric field in the plasma bulk to be reversed and the electron-ion energy transfer limited to collisional processes. Although the theory of ambipolar diffusion of a fully ionized plasma across a magnetic field is not sufficiently developed to make quantitative predictions, one would expect

a magnetic field to inhibit the collective energy transfer at the point where the electron Larmor radius becomes smaller than its mean free path and smaller than the scale length of the plasma. Since in a blowoff plasma expansion of the nature encountered in this experiment, the density is a rapidly decreasing function of the plasma thickness, one would not expect a complete energy transfer through collisional effects and hence the asymptotic velocity of the plasma front should decrease in a magnetic field.

Evidence for the reversal of the space-charge forces in the presence of the magnetic field is furnished by the wall probe response in a field of $B_0 = 70$ kgauss. The current signals with $B_0 = 0$, and $B_0 = 70$ kgauss are shown in Figure 4.16. It can be seen that whereas the plasma front in the free expansion has a negative polarity, in the presence of the field the current is initially positive and greater by a factor of four over the zero field case. This indicates a net positive charge in the leading edge of the plasma under these conditions.

0.5 $\mu\text{sec}/\text{div}$
0.5 v/div



a) $B_0 = 0$

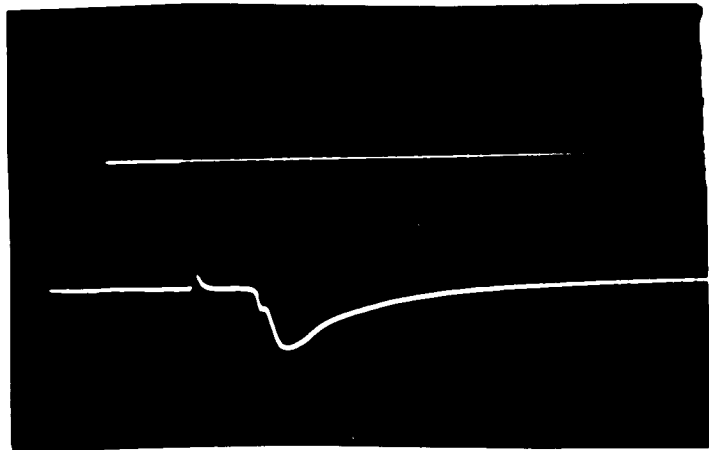
0.5 $\mu\text{sec}/\text{div}$
2.0 v/div



b) $B_0 = 70 \text{ kgauss}$

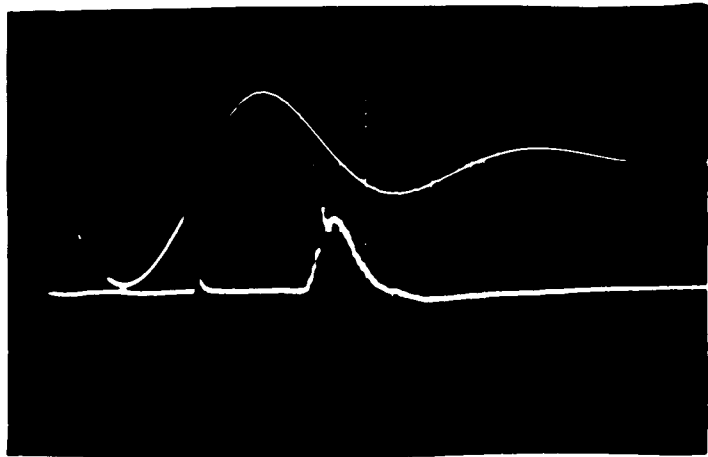
FIG. 4.16 RESPONSE OF FARADAY CUP
WALL PROBE

0.5 $\mu\text{sec}/\text{div}$
0.5 v/div



a) $B_0 = 0$

0.5 $\mu\text{sec}/\text{div}$
2.0 v/div



b) $B_0 = 70 \text{ kgauss}$

FIG. 4.16 RESPONSE OF FARADAY CUP
WALL PROBE

The velocity reduction shown in Figure 4.11 indicates that a field of $B_0 > 20$ kgauss is sufficient to prevent any collective electron-ion energy exchange. The observation that fields of larger magnitude than this lead to no further reduction in the velocity of the plasma front lends particular credence to the argument above. It is interesting to note that the velocity reduction for the aluminum blowoff plasma is very nearly one-half of the free expansion velocity. Neglecting collisional effects, this would be consistent with a charge multiplicity of the aluminum ions of three. That is, the ions gain energy by a factor of four or $z+1$ through the collective interaction.

In order to detect any possible z dependence of the velocity reduction, the expansion in the magnetic field of plasmas formed from magnesium and copper was also examined. The ionization energies of the first few levels of these metals are shown in Table 4.1.

	1	2	3	4	5	6
Al	5.98	18.8	28.4	120	154	190 (ev)
Cu	7.72	20.3	36.8	59	82	110 (ev)
Mg	7.64	15.0	80.1	109	141	186 (ev)

Table 4.1 Ionization Energies of Al, Cu, and Mg.

The velocity of the ionization front for these target metals is shown in Figure 4.17. In comparison with Figure 4.11, it can be seen that the velocity reduction for copper (~ 2.3) was greater than that observed for aluminum (~ 2.0). Although considerable scatter was observed in the data for magnesium at low B_0 , the velocity reduction in this case appeared to be somewhat less (~ 1.9) than that observed for aluminum.

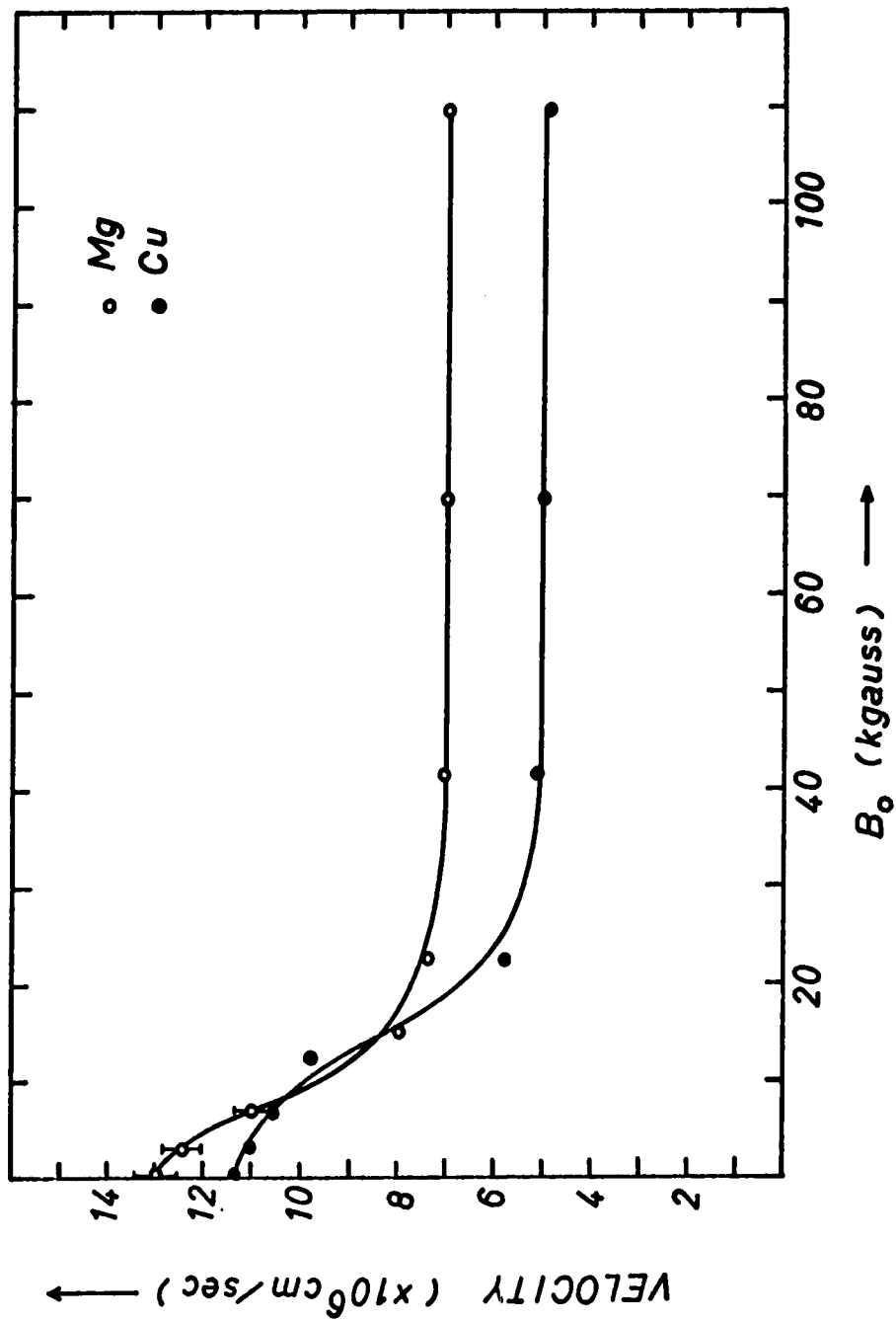


Fig. 4.17 Velocity of Ionization Front of Plasmas Formed from Mg and Cu in a Magnetic Field.

With the breakdown of the collective energy transfer mechanism, one might expect a considerable enhancement of the electron temperature behind the plasma wavefront. In order to look for such an effect, an attempt was made to relate the electrical conductivity of the plasma to the width of the unintegrated diamagnetic signal. Such a calculation in terms of the magnetic Reynold's number has been made by Schwirze and Tuckfield²⁵.

The distance over which B diffuses into a plasma is given approximately by equating the magnetic Reynold's number to unity, that is, $R_m = \mu_0 \sigma V d = 1$. This can be seen as follows, for $R_m \gg 1$, magnetic transport dominates diffusion and the field is "frozen" into the plasma, and for $R_m \ll 1$, magnetic diffusion dominates and this case is characterized by a penetration of magnetic field into the plasma bulk. Thus in a diamagnetic or partially diamagnetic plasma moving in a magnetic field, the point at which R_m equals unity is a crude measure of the distance over which the plasma can modify the external field⁴⁵.

The width d of the unintegrated diamagnetic signal was obtained by plotting the positions of its leading and trailing edges as a function of time as is shown in Figure 4.18, at $B_0 = 70$ kgauss. It was observed that d was relatively independent of distance from the target surface for $R > 1$ cm, but depended strongly on B_0 . The plasma conductivity was estimated from the relation,

$$\sigma_{\text{eff}} = \frac{1}{\mu_0 V d} = \frac{7.96 \times 10^7}{V d} \quad (\text{ohm} \cdot \text{cm})^{-1}, \quad \dots 4.9$$

where V is the velocity of the plasma front in cm/sec, and d is the width of the front in cm. The conductivities calculated in this manner at $R = 1.5$ cm are shown in Figure 4.19.

Using Spitzer's¹ formula for the conductivity of a plasma transverse to a strong magnetic field (Larmor radius less than electron m. f. p.),

$$\sigma_{\text{coll}} \approx \frac{T^{3/2}}{1.29 \times 10^4 z \ln \Lambda} \quad (\text{ohm} \cdot \text{cm})^{-1}, \quad \dots 4.10$$

so that assuming $\ln \Lambda \approx 10$, $z = 3$, we have,

$$\sigma_{\text{coll}} \approx 2.5 \theta^{3/2} \quad (\text{ohm} \cdot \text{cm})^{-1},$$

where θ is in ev. Thus the values of conductivity shown in **Figure 4.19** would correspond to temperatures in the range of 1 - 4ev on the basis of collisional dissipation.

Schwirze and Tuckfield²⁵ have observed conductivities of a similar magnitude in the wavefront of a spherically symmetric laser-produced plasma expanding in a magnetic mirror field, using the same type of calculation. They have attributed the rather low values of conductivity to turbulence introduced by a high electron drift velocity through the two stream instability.

In the present case, it is doubtful whether the electron streaming velocity is large enough to excite the two stream instability (see Appendix C), in any event, turbulent dissipation should introduce a strong density dependence in the plasma conductivity (see Appendix C). This was not observed, that is, the plasma conductivity as calculated in this manner was found to be relatively independent of distance from the target surface even though the density falls off as $1/R^2$.

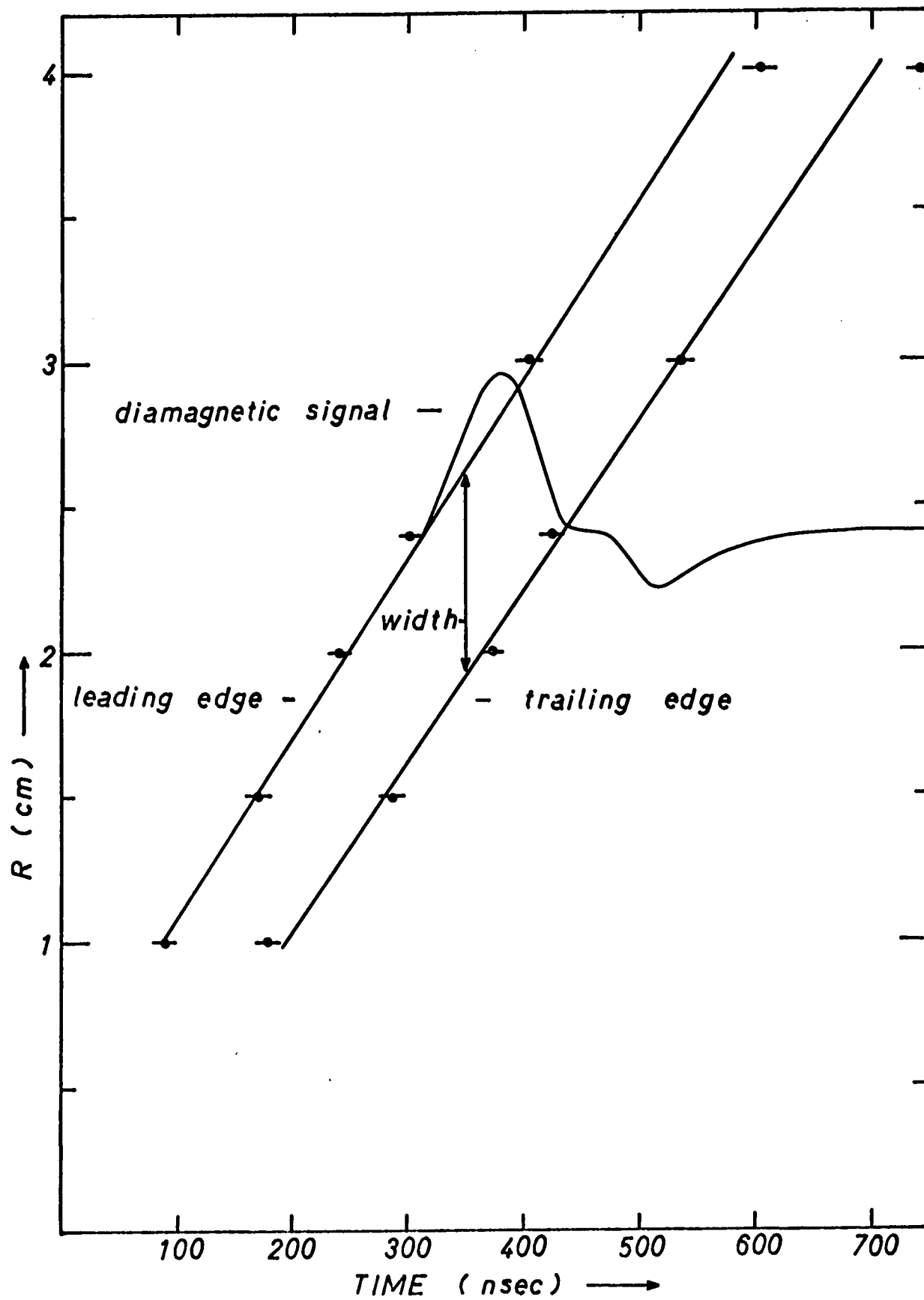


Fig. 4.18 Width of Diamagnetic Signal at $B_0 = 70$ kgauss.

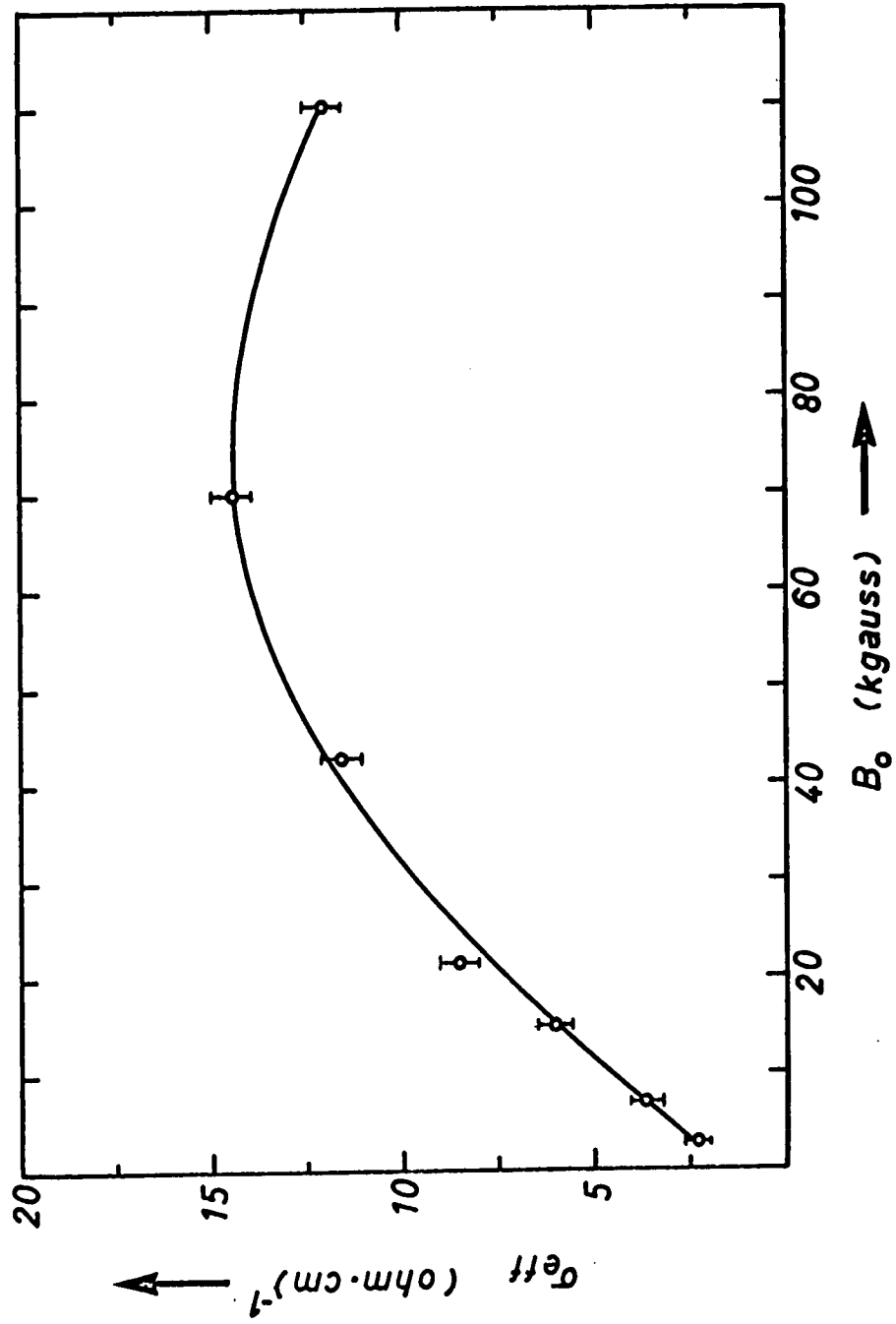


Fig. 4.19 Conductivity in Ionization Front, 1.5cm from the Target Surface.

4.8 Possible Causes of the Onset of Polarization.

As discussed in Section 4.3, one might expect a diamagnetic cross-field plasma flow under the condition,

$$\frac{1}{2} n_1 k m_1 v^2 > \frac{B^2}{2 \mu_0} \quad , \quad \dots 4.11$$

which is certainly fulfilled in the early stages of the expansion of the blowoff plasma of this experiment. It must be noted, however, that this relation does not ensure diamagnetic flow if the initial stream-field interface is not stable enough to prevent the development of a polarization electric field. It will be shown that the geometry of the present experiment introduces a mechanism for this development in the early stages of the blowoff process.

This mechanism stems from the toroidal nature of the magnetic field and it is expected that the resulting particle drifts are exactly analogous to those which are known to prevent stable plasma confinement in a simple torus⁴⁶.

The drift velocity of the guiding centre of a single particle in a magnetic field is⁴⁷,

$$\underline{v}_g = \frac{m v_\perp^2}{4q} \frac{\underline{B} \times \nabla B^2}{B^4} + \frac{m v_\parallel^2}{q} \frac{\underline{B} \times (\underline{B} \cdot \nabla) \underline{B}}{B^4} + \underline{v}_\parallel \quad , \quad \dots 4.10$$

where v_\parallel is the component of the particle velocity along \underline{B} , and v_\perp is the perpendicular component. In an inhomogeneous magnetic field, it follows that two charge dependent particle drifts in the direction perpendicular to \underline{B} and ∇B result. The first results from a gradient in the induction and the second, from a curvature of the field lines. With reference to

Figure 4.20, it can be seen that in the geometry of the present experiment these drifts will contribute to the required polarization field.

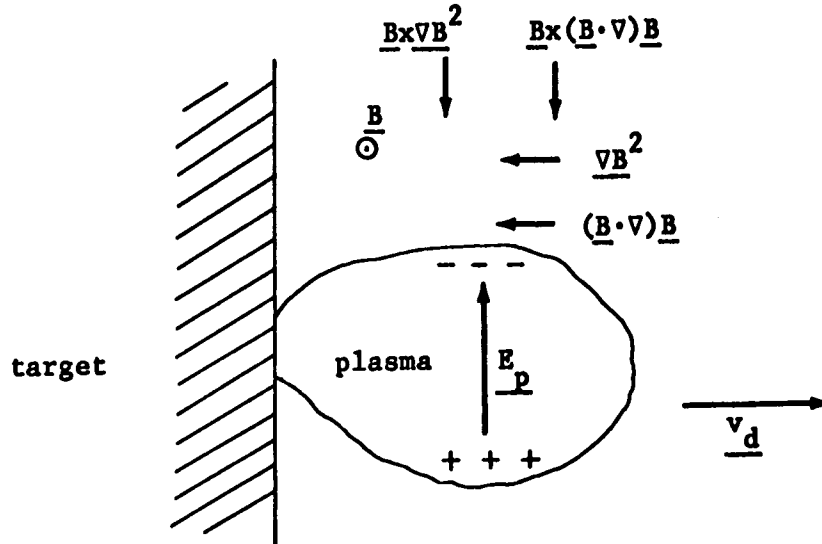


Fig. 4.20 Nature of the Particle Drifts Introduced by Magnetic Field Gradient and Curvature.

CHAPTER 5 CONCLUSIONS AND SUGGESTIONS FOR FUTURE RESEARCH

The properties of a laser-blowoff aluminum plasma resulting from the interaction of a moderately powerful ruby laser pulse with a massive target have been examined. It has been shown that the luminous flare at the target surface formed by this interaction rapidly degenerates into a dense, recombination dominated plasma ($n_e < 10^{19} \text{ cm}^{-3}$, $T_e < 10 \text{ eV}$) with most of the incident laser energy manifested as ordered energy of expansion soon after the end of the heating phase.

The rapid expansion and energetic ion emission from the laser-solid interaction has been explained in terms of a simple hydrodynamic model. The large ion energies have been shown to be partially attributable to a collective electrostatic energy transfer between the ions and electrons as the plasma cloud expands.

The simple magnetic field geometry used in this experiment has been shown to be ineffective in preventing the rapid expansion of the blowoff plasma because of an electrical polarization and $\underline{E} \times \underline{B}$ drift. At the same time, it appears that the normal electrostatic energy transfer may be prevented by a relatively small transverse magnetic field. The heating of the plasma behind the ionization front observed in this experiment has been attributed to this latter effect. The electrical polarization observed under the conditions of this experiment underlines the necessity of a high degree of spherical symmetry for the successful magnetic confinement of laser-produced plasmas.

The considerations discussed in Chapter 3 indicate that Q-spoiled laser irradiation of solid matter with dimensions greater than $\sim 5\mu$ is essentially a surface phenomenon, thus attempts to produce spherically symmetric

plasmas by irradiating single particles of larger dimensions are not likely to succeed.

Much additional work remains to be done on the nature of the laser-solid interaction. Apart from the properties of the plasma produced, the actual mechanism whereby intense light is absorbed in dense plasmas is of fundamental interest. Many authors^{10,3,37} have assumed the inverse bremsstrahlung absorption coefficient to be a function only of the plasma temperature and density, independent of the radiation flux. Recently⁴⁸, it has been noted that a non-Maxwellian velocity distribution induced by the intense radiation field may have a significant effect on the absorption coefficient. Dawson et al⁴⁹ have also pointed out that density gradients may allow a coupling of laser energy into an overdense plasma through the generation of longitudinal plasma oscillations.

The effect of Compton photon-electron interactions and their role in the absorption process has yet to be investigated experimentally. It has been pointed out^{50,51,52} that this process may be quite effective in absorbing laser energy in the intermediate range of densities $10^{16} < n_e < 10^{19} \text{ cm}^{-3}$.

It seems likely that much could be gained in the area of laser absorption in dense plasmas by examining the laser energy absorbed by thin metal foils in the 1 - 5 μ range. Measuring the time of onset of transparency for such foils might also furnish additional information on the dynamics of the blowoff process, for example, the validity of the various theories relating depth of target fissure to time could be examined.

From the discussion in Chapter 4, it is apparent that the magnetic field geometry used in this experiment may be responsible for the rapid polarization and non-diamagnetic behaviour of the blowoff plasma that has

been observed in this experiment. It would be desirable to generate a field with zero gradient and curvature at the target surface. This could be easily done by using as a current element a flat metal strip. Under these conditions, it is possible that the diamagnetic expansion discussed in the three dimensional case by Bhadra¹⁵ and Poukey¹⁶ could be observed.

BIBLIOGRAPHY

1. L. Spitzer, "Physics of Fully Ionized Gases" (Interscience Publishers Inc., New York, 1962), 2nd. ed.
2. H. Opower et al, Z. Naturforschg. 22A, 1392 (1967).
3. A. F. Haught and D. H. Polk, Phys. Fluids 9, 2047 (1966).
4. U. Ascoli-Bartoli, C. DeMichelis, and E. Mazzucato, in "Plasma Physics and Controlled Nuclear Fusion Research" (International Atomic Energy Agency, Vienna, 1966), Vol. 2, p. 941.
5. C. David, P. V. Avizonis, H. Weichel, C. Bruce, and K. D. Pyatt, J. Quant. Elect. QE-2 , 499 (1966).
6. P. Langer et al, J. Quant. Elect. QE-2 , 493 (1966).
7. M. J. Bernstein and G. G. Comisar, J. Appl. Phys. 41 , 729 (1970).
8. F. Floux et al, Phys. Rev. 1A, 821 (1970).
9. N. G. Basov and O. N. Krokhin, in "Proceedings of the Conference on Quantum Electronics", Paris (1963).
10. J. M. Dawson, Phys. Fluids 7, 981 (1964).
11. O. N. Krokhin, Sov. Phys. - Tech. Phys. 9, 1024 (1965).
12. A. Caruso, B. Bertolli, and P. Giupponi, Il Nouvo Cimento 45, 176 (1966).
13. A. Caruso and R. Gratton, Plasma Physics 10, 867 (1968).
14. P. I. Shkuropat and G. A. Schneerson, Sov. Phys. - Tech. Phys. 12 (1967).

15. D. K. Bhadra, *Phys. Fluids* 11, 234 (1968).
16. J. W. Poukey, *Phys. Fluids* 12, 1452 (1969).
17. J. F. Ready, *Phys. Rev.* 137A, 620 (1965).
18. W. I. Linlor, *Appl. Phys. Lett.* 3, 210 (1963).
19. N. R. Isenor, *Appl. Phys. Lett.* 4, 152 (1964).
20. N. G. Basov et al, *Sov. Phys. - JETP.* 24, 659 (1967).
21. R. V. Ambartsuyan et al, *Sov. Phys. - JETP.* 21, 1061 (1965).
22. C. David and H. Weichel, *J. Appl. Phys.* 40, 3674 (1969).
23. E. W. Sucof et al, *Phys. Fluids* 10, 2035 (1967).
24. R. G. Tuckfield and F. Schwirze, *Plasma Physics* 11, 11 (1969).
25. F. Schwirze and R. G. Tuckfield, *Phys. Rev. Lett.* 22, 1284 (1969).
26. U. Ascoli-Bartoli et al, 3rd. Conf. on Plasma Phys. and Nuclear Fusion, Novosibirsk (1968).
27. A. F. Haught, D. H. Polk, and W. J. Fader, 3rd. Conf. on Plasma Phys. and Nuclear Fusion, Novosibirsk (1968).
28. H. Opower and E. Burlefinger, *Phys. Lett.* 16, 37 (1965).
29. H. Opower and W. Press, *Z. Naturforschg.* 21A, 344 (1966).
30. J. L. Schwob, C. Breton, W. Seka, and C. Minier, *Plasma Physics* 12, 217 (1970).
31. P. Dhez and P. Jaegle, *J. Appl. Phys.* 40, 2545 (1969).

32. W. Seka, C. Breton, J. L. Schwob, and C. Minier, *Plasma Physics* 12, 73 (1970).
33. G. Lampis and S. C. Brown, *Phys. Fluids* 11, 1137 (1968).
34. G. L. Rogoff, *Appl. Optics* 8, 723 (1969).
35. B. E. Patton and N. R. Isenor, *Can. J. Phys.* 44, 1237 (1968).
36. D. Bohm, in "The Characteristics of Electrical Discharges in Magnetic Fields" (A. Guthrie and R. K. Wakerling, eds., McGraw-Hill, New York, 1949).
37. S. Fader, *Phys. Fluids* 11, 2200 (1968).
38. N. G. Basov et al, *Sov. Phys. - Tech. Phys.* 13, 1581 (1969).
39. H. R. Griem, "Plasma Spectroscopy" (McGraw-Hill, New York, 1964) p. 292.
40. P. Mulser and S. Witkowski, *Phys. Lett.* 28A, 151 (1968).
41. J. L. Tuck, *Phys. Rev. Lett.* 3, 313 (1959).
42. G. O. Barney, *Phys. Fluids* 12, 2429 (1969).
43. D. A. Baker and J. E. Hamnel, *Phys. Fluids* 8, 713 (1965).
44. A. A. Plyutto, *Sov. Phys. - JETP.* 12, 1106 (1961).
45. R. J. Rosa, "Magnetohydrodynamic Energy Conversion" (McGraw-Hill, New York, 1968).
46. D. J. Rose and M. Clark, "Plasmas and Controlled Fusion" (The M. I. T. Press, Cambridge Mass., 1961).

47. W. P. Allis, Handbuch der Physik, 21, 383 (Springer, Berlin, 1957).
48. T. P. Hughes and M. B. Nicholson-Florence, J. Phys. A (Proc. Phys. Soc.) 1, 588 (1968).
49. J. Dawson, P. Kaw, and B. Green, Phys. Fluids 12, 875 (1969).
50. J. Peyraud, J. Phys. (France) 29, 55 (1968).
51. J. Peyraud, J. Phys. (France) 29, 88 (1968).
52. J. Peyraud, J. Phys. (France) 29, 306 (1968).
53. O. Buneman, Phys. Rev. Lett. 1, 8 (1958).
54. R. Z. Sagdeev and A. A. Galeev, "Non-Linear Plasma Theory" (W. A. Benjamin Inc., 1969).

Review Papers

- (i) R. G. Meyerand Jr., "Laser Plasma Production - A New Area of Plasma-Dynamics Research", AIAAA. Jour. 5, 1730 (1967).
- (ii) C. DeMichelis, "Laser Interaction with Solids: A Bibliographical Review", Westinghouse Research Report 69-1C1-IBEAM-R1 (1969).

APPENDIX A. EFFECT OF DENSITY GRADIENT ON TEMPERATURE DETERMINATION

It can be shown that, to a first order, the density distribution in the plasma test cross-section is not important for the temperature measurement providing the temperature is uniform. This can be seen as follows: If we consider a circular plasma cross-section, uniformly irradiated by an external laser beam, the calculated temperature is determined by the quantity, $\frac{I E}{\xi}$, where E is the emission (per unit area) from the test cross-section, I, the incident laser power, and ξ , the absorbed laser power. If we divide the test cross-section into N subsections (labeled j), of equal area, and with uniform density in each subsection (but possibly different densities in different subsections), then if,

$$T_j = \frac{I_j E_j}{\xi_j} , \quad \dots \text{ A.1}$$

we have,

$$E = \frac{1}{N} \sum E_j , \quad \dots \text{ A.2}$$

$$\xi = \sum \xi_j , \quad \dots \text{ A.3}$$

and $I = \sum I_j = N I_j . \quad \dots \text{ A.4}$

So that,

$$T = \frac{I E}{\xi} = \frac{N I_j \frac{1}{N} \sum E_j}{\sum \xi_j} = T_j \quad \dots \text{ A.5}$$

Thus, the calculated temperature, which is a function of T, will be characteristic of the temperature in any of the equal temperature but different density subsections.

APPENDIX B. THE MODEL OF OPOWER AND PRESS

Considering a spherically symmetric plasma cloud initially in thermal equilibrium with $T_e = T_i$, Opower and Press²⁹ consider the expansion in the following terms:

Electrons which on account of their small mass have a high velocity leave the spherical plasma surface, resulting in a positively charged plasma bulk. The plasma senses a voltage, V , to the further removed electron sheath such that the escape of further electrons is prevented.

In equilibrium, according to Boltzman statistics,

$$N = N_0 \exp - \frac{e V}{kT_e} \quad \dots B.1$$

electrons leave the plasma. Taking a spherical condensor as a model,

$$V = \frac{N_0 \exp - \frac{e V}{kT_e}}{4\pi \epsilon r} \quad \dots B.2$$

Thus, a radial outward force acts on the ions which is equal to the rate of change of their kinetic energy, that is,

$$N_i m_i \dot{r}_i = - e N_0 \exp - \frac{e V}{kT_e} \frac{dV}{dr} \quad \dots B.3$$

Through integration, it follows that as $r \rightarrow \infty$,

$$N_i E_{i\infty} = N_0 kT_e \left[1 - \exp - \frac{e V_0}{kT_e} \right] + N_i kT_i \quad \dots B.4$$

where $N_0 = zN_i$, thus,

$$E_{i\infty} = zkT_e \left[1 - \exp - \frac{e V_0}{kT_e} \right] + kT_i \quad \dots B.5$$

For any practical case involving laser-produced plasmas ($r_0 < 0.1\text{mm}$, $kT_e = 10\text{ev}$, $N_0 = 10^{16}$), it follows from equation B.2 that,

$$\exp - \frac{e V_0}{kT_e} \ll 1 , \quad \dots \text{ B.6}$$

and,

$$E_{i\infty} = zkT_e + kT_i . \quad \dots \text{ B.7}$$

APPENDIX C. TURBULENT DISSIPATION

In general, the conductivity of a plasma will be determined by the effective collision or relaxation time of the plasma electrons. That is,

$$\sigma_{esu} = \frac{\omega_{pe}^2}{4\pi} \tau_{eff} \quad \dots C.1$$

In non-turbulent situations, τ_{eff} will be just the electron collision time.

In the presence of turbulence, however, τ_{eff} will be governed by wave-particle interactions rather than collisions. Plasma turbulence may be classified as weak or strong, according to whether the plasma microfields are attributable to a two stream instability or an ion acoustic instability. The threshold for these instabilities is related to the electron streaming velocity, v_s .

For strong turbulence, the requirement is, $v_s > \left[\frac{\theta_e}{m_e} \right]^{1/2}$, and the effective relaxation time is⁵³,

$$\tau_1 \approx \left[\frac{m_i}{m_e} \right]^{1/3} \frac{2\pi}{\omega_{pe}} \quad \dots C.2$$

For weak turbulence, the requirement is, $\left[\frac{\theta_e}{m_i} \right]^{1/2} < v_s < \left[\frac{\theta_e}{m_e} \right]^{1/2}$, and the effective relaxation time is⁵⁴,

$$\tau_2 \approx \frac{T_i}{T_e} \frac{\bar{v}_e}{v_s} \frac{1}{\omega_{pe}} \quad \dots C.3$$

It can be seen that both of these mechanisms introduce a ω_{pe} dependence in σ_{eff} .

In the case of the plasma front formed from an aluminum target, as dis-

cussed in Section 4.6, it is doubtful whether the transverse electron streaming velocity 1.5 cm from the target surface is high enough to excite either of these instabilities. The streaming velocity can be estimated from the plasma temperature and density as obtained from the the double probe data, and the perturbation in the magnetic field as measured by the diamagnetic probe. That is,

$$\frac{e}{c} n_e v_s \approx \frac{1}{4\pi} \frac{d(\Delta B)}{dr} \approx \frac{1}{4\pi} \frac{\Delta B}{h} , \quad \dots \text{C.4}$$

where n_e is the electron density, and h is the width of the unintegrated diamagnetic signal.

The streaming velocities estimated in this manner at $B_0 = 2.8, 21.5,$ and 70 kgauss are shown in Table C.1. It can be seen that these values are well below the threshold for the two stream instability and near the threshold for the ion acoustic instability.

B_0 (kgauss)	θ (ev)	n_e (cm^{-3})	ΔB (gauss)	h (cm)	v_s (cm/sec)	$\left[\frac{\theta}{m_e}\right]^{1/2}$ (cm/sec)	$\left[\frac{\theta}{m_e}\right]^{1/2}$ (cm/sec)
2.8	3	1.5×10^{15}	265	2.6	3×10^5	7×10^7	3×10^5
21.5	4	2.5×10^{15}	650	1.2	6×10^5	8×10^7	3.5×10^5
70	5	5×10^{15}	960	0.8	1×10^6	9×10^7	4×10^5

Table C.1 Estimate of Electron Streaming Velocity, v_s , in Plasma Wavefront, 1.5cm from Surface of an Aluminum Target.